Macroporous Semiconductors Tantalum Oxide, (Oxy)nitride and Nitride for Photocatalytic Hydrogen Evolution

Min Ying Tsang

Master by Research

2010

Content **Page**

List of Figures

Page

List of Tables

Acknowledgements

First of all, I would like to express my gratitude to my supervisor Dr. Richard E. Douthwaite for his great help and advice throughout the whole year of my masters' studies with chemistry, problem solving and experimental work. I gained a lot of knowledge under his patient guidance.

I would also like to thank my mentor Cindy Chou not only for her enthusiastic guidance on my project, but also her kind help with my life in York outside my studies.

Moreover, I would like to express my gratefulness to my research group mate Adam Morgan for his support with both laboratory work and machine operation. Also thanks to Rob Thatcher, and laboratory technicians Iman and Nasser for help with laboratory issues.

Furthermore, I would like to thank Ian Wright from the nanocentre for his kind help with operating the SEM and TEM instruments. Nicole Hondow and Michael Ward for SEM and TEM training from Leeds Electron Microscopy and Spectroscopy (LEMAS) centre, University of Leeds. Also the PhD students Navpreet and Steve from Prof. Duncan Bruce's research group for operation guidance and offering support with BET surface area measurements and also Dr. Adrian Whitwood for his x-ray powder training. I would also like to thank Steve and Mike from the department stores for kind help with chemical supplies.

I also thank my friends and my flatmates from Hong Kong and UK for their mental support and encouragement during the whole year. They make me feel that I am not alone when studying here and also enlighten me on some daily life matters.

Lastly, I would like to send my great thanks to Dr. Tony Wild for the Wild fund which has been a huge support for my studies in York. Most importantly, I would like to send my great gratitude to my parents not only for their financial support, but also their care and spiritual support on everything for my whole life, to motivate and enlighten me when I am depressed and also to share my happiness.

Abstract

Due to the serious climatic consequences of CO_2 pollution and increasing global energy demand, a clean and sustainable energy source is required. Perhaps the ideal clean fuel is hydrogen, which would be sustainable if it could be sourced efficiently from water. Photocatalysis using metal-semiconductor composites is potentially a feasible way to make use of solar energy to drive the water splitting reaction to product hydrogen and oxygen. A significant number of studies have been reported in recent decades on the development of new photocatalytic materials, ion doping, co-catalyst addition and modification of the morphology to enhance the light harvesting, and increase the number of active sites in order to improve the photocatalytic activity.

In this project, three-dimensional ordered macroporous (3DOM) Ta_2O_5, TaON and Ta_3N_5 have been prepared and loaded with Pt co-catalyst (0.5 wt% and 3 wt %). Subsequently the photocatalytic activities with respect to hydrogen production using methanol as a sacrificial reagent were measured and compared with bulk analogues. A colloidal crystal templating method using polystyrene (PS) monodispersed spheres with diameter 500±20 nm was used for the synthesis of the macroporous materials. Characterizing data of the macroporous materials was obtained by powder X-ray diffraction (PXRD), scanning electron microscopy (SEM), transmission electron microscopy (TEM), BET surface area measurement and UV-Vis reflectance and absorbance spectroscopy. Pore sizes of macroporous Ta_2O_5, TaON and Ta_3N_5 are 370±10, 380±10 and 400±10 nm, respectively. The wall thicknesses are 70±5, 60±5 and 60±10 nm, respectively. Spectroscopy showed that the macroporous Ta_2O_5, TaON and Ta_3N_5 structures are photonic and stop bands are observed at 721, 683 and 748 nm, respectively. Surface areas were measured to be 11.53, 12.12, 22.98 m^2g^{-1} for macroporous Ta_2O_5, TaON and Ta_3N_5 respectively whereas bulk materials were between 1.35, 3.22 and 7.91 m^2g^{-1}, respectively. The microstructure of the macroporous materials was determined by PXRD and electron microscopy which showed increasing crystallite fragmentation as the level of nitridation increases. Calculated crystallite size as determined by PXRD are 60, 36, 35 nm for bulk Ta_2O_5, TaON and Ta_3N_5 and 40, 33, 18 nm for macroporous Ta_2O_5, TaON and Ta_3N_5, respectively. Electron microscopy of 0.5 wt% Pt loaded Ta_2O_5 showed evidence for deposition of Pt on the surface of the bulk Ta_2O_5 and on the inner walls of the macroporous Ta_2O_5, respectively, but some aggregation occurred. Comparing the photocatalytic activities for hydrogen production showed that Pt addition enhances the activities

for both bulk materials and macroporous Ta_2O_5, however, less activity was observed for macroporous TaON and Ta_3N_5. Normalizing for the increase in surface area of macroporous materials Ta_2O_5 and Ta_3N_5 show ca 50% less activity whereas TaON shows a 40% increase in activity. It should be noted errors have not been estimated and the surface chemistry of the materials is at present unknown. However, the activities strongly indicate that photocatalysis is occurring throughout the porous material.

In addition, because of difficulties comparing photocatalytic reactions in the literature a series of calibration experiments was performed using P25 and methanol. Activity as a function of photocatalyst mass and concentration were performed. The results indicate that the concentration of P25 does not have significant effect for the photocatalytic activities and the optimum amount of photocatalyst in our reaction system is ca 80 mg (in the system of 100 ml H_2O + 10 ml MeOH solution).

Introduction
Chapter 1

1.1 Catalysis and the Energy Problem

Catalysis is a vital industrial process because it can provide new efficient routes to chemical products by reducing the reaction time and energy consumed, whilst increasing the yield and ease of purification. Catalysis can be broadly divided into two subgroups, homogeneous and heterogeneous, which are differentiated by the phase distribution of catalyst, reagents and products. Homogeneous catalysis is characterized by having everything in the same phase, for example, the well known Wilkinson's catalyst, $[RhCl(PPh_3)_3]$, for hydrogenation. In comparison, for heterogeneous catalysis the catalyst and reactants are in different phases usually with the catalyst in the solid phase, where an example is the alkylation of benzene using zeolites.

Photocatalysis is a chemical reaction mediated by a catalytic material via photoabsorption. Similarly, it can be divided into homogeneous and heterogeneous subgroups. In homogeneous photocatalytic reactions, the excitation of an electron to a high energy state of a molecule in solution occurs, followed by a chemical reaction via the reduced or oxidized orbital.[1] In heterogeneous photocatalysis, the photocatalyst is normally a solid state material where excitation can be restricted to a single ion, which is similar to the molecular case, or across a band gap generating electron and hole pairs that can perform redox reactions.[2-3] The focus of this thesis is heterogeneous photocatalysis mediated by electron excitation across a semiconductor benadgap.

In recent years, an average global temperature increase and global environmental pollution due to CO_2 emissions have been identified. Additionally, global energy demand is increasing rapidly (Fig. 1.1) because of increasing population and increasing development of countries such as China and India. Therefore, the search for clean and sustainable energy resources is becoming increasingly important.

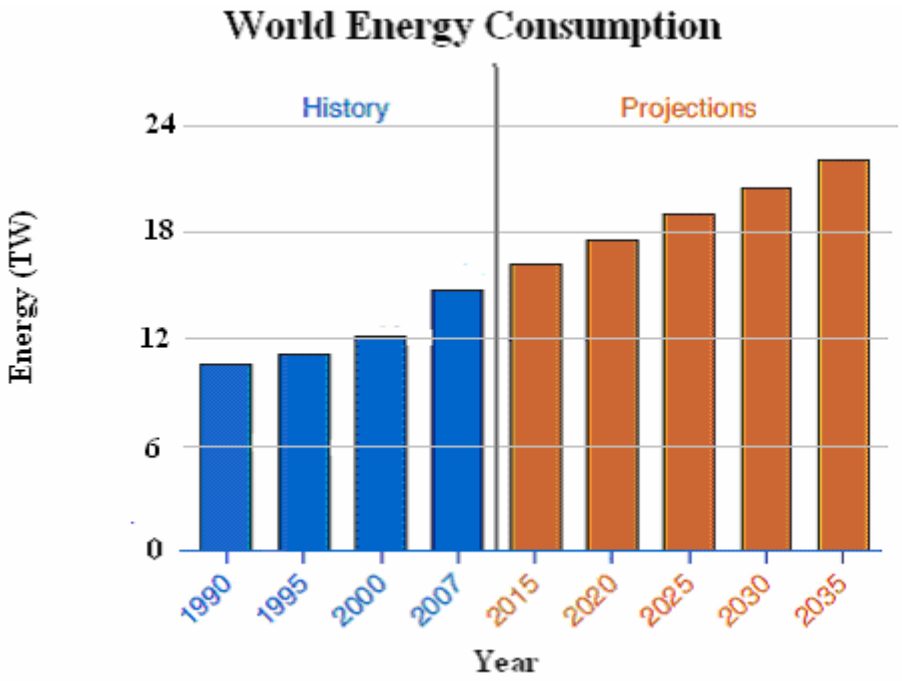

Fig. 1.1 World energy demand from International Energy Outlook 2010 [4]

Current global energy consumption is estimated at 15 TW and increasing rapidly. The greatest potential source of energy by far is from the sun, with about 86000 TW incident at the surface of the Earth per year. Solar energy is therefore clearly sufficient to meet global needs; however irradiation is diffuse and diurnal. Technologies used to achieve solar energy conversion include solar furnaces, photovoltaics and dye-sensitized solar cells, which generate electricity via heating water, excitation across p-n junctions and photoelectrochemically, respectively. However, in each case, storage (e.g. via batteries) is expensive, inefficient and power output is low. An alternative, which can potentially provide energy on demand, is solar fuel production using photocatalysis.[5-9]

1.2 Semiconductors for photocatalytic solar fuel production

Semiconductor photocatalysis has received great interest for both environmental cleanup studies to remove polluting organic contaminants from air and water, and relevant to this thesis, hydrogen production from water photolysis.[10-11] The principle of semiconductors is shown in Fig. 1.2.

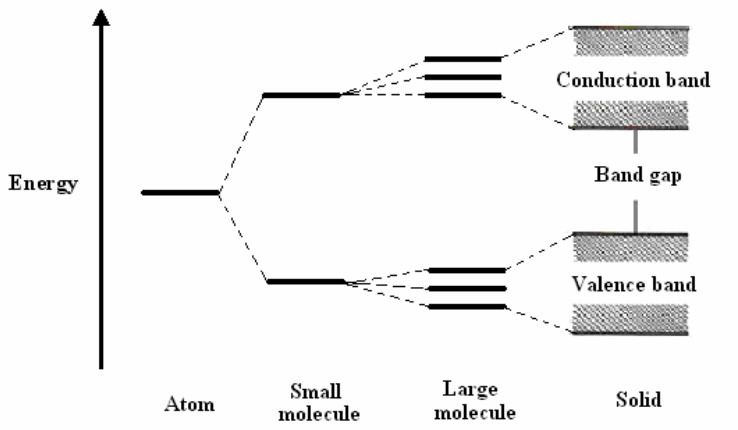

Fig. 1.2 Band structure of a solid state semiconductor

For extended solids, the molecular orbitals within the antibonding/bonding manifolds become sufficiently close to be defined as a band. The conduction band contains antibonding character and the valence band contains bonding character. The band gap is the energy difference between the filled valence band and empty conduction band.

The concept for semiconductor photocatalysis is that when a photon of sufficient energy is absorbed, an electron is excited from the valence band to the conduction band and generates an electron-hole pair. The electron and hole subsequently separate and migrate to the surface where redox chemistry occurs. Fig. 1.3 shows the principle of hydrogen and oxygen generation.

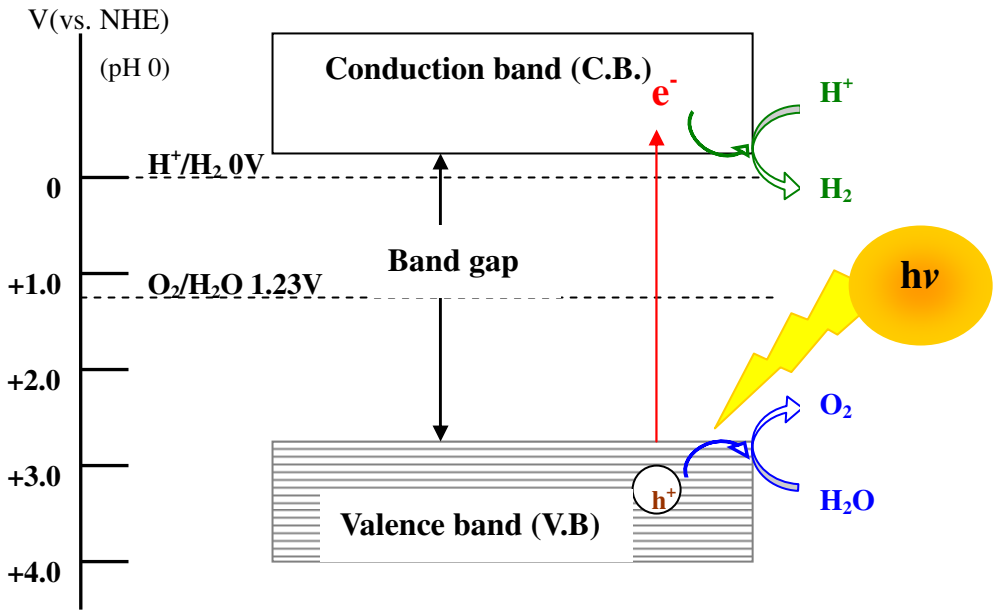

Fig. 1.3 Principle of semiconductor photocatalytic water splitting

Hydrogen is an ideal source that could produce clean energy because its combustion product is water; however, the vast majority of current hydrogen production is from the steam reforming of hydrocarbons, [12-14] generating CO_2 as a by-product. The ideal source of hydrogen is water because it is abundant, available globally and is truly renewable as the combustion product of hydrogen burning is water. Splitting water to hydrogen and oxygen requires energy because it is an endoenergetic reaction. Therefore, the solar energy is stored in the chemical bonds and, in contrast to photoelectricity, the energy can be stored efficiently and used on demand for high power applications, where chemical fuels (i.e. hydrocarbons) are currently in use.

Considering Fig. 1.3, the reduction potential of H^+ to H_2 and the oxidation potential of H_2O to O_2 must be located between the valence band (V.B.) and conduction band (C.B.) of the semiconductor photocatalyst and the minimum band gap must be 1.23 eV. In reality the minimum gap should be at least 1.4 eV due to activation energies associated with overpotentials. Once a photon has been absorbed, an electron is excited and the generated electron (e^-) and hole (h^+) can cause water reduction and oxidation respectively after migrating to the surface. H_2 and O_2 are then produced at the surface of the photocatalyst.[15] All these processes have an associated over potential/activation energy.

1.3 Solar fuel devices

A very similar concept for hydrogen production is to use photovoltaics either in a photoelectrochemical cell or from direct light absorption without external circuitry.[8] The photovoltaic device is used to produce electricity by absorbing and converting the photon energy as shown in Fig. 1.4.

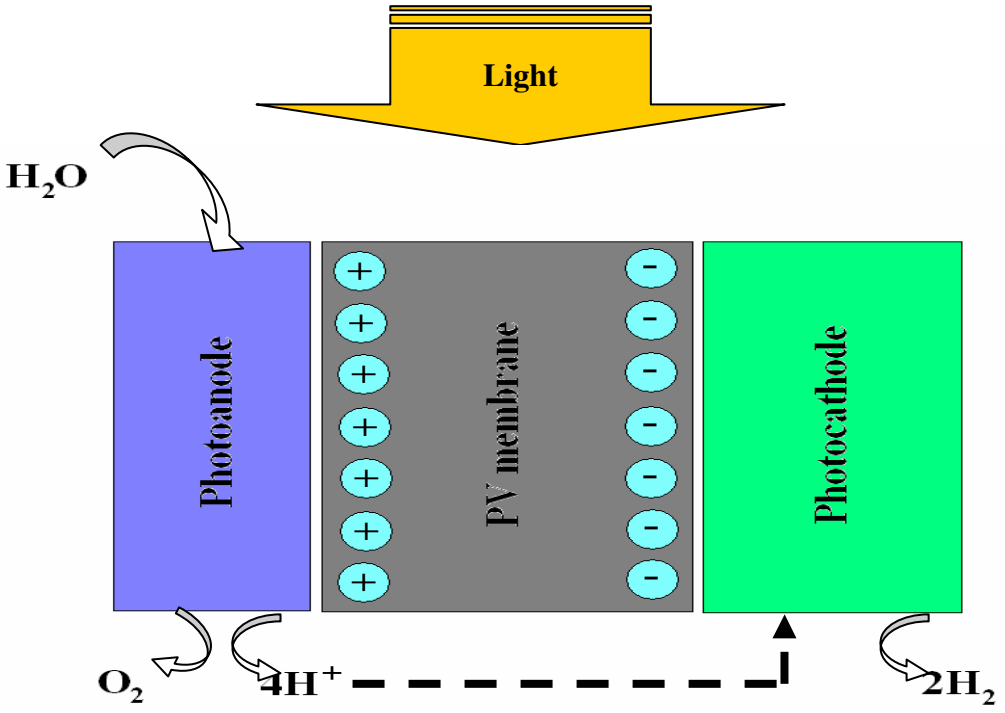

Fig. 1.4 Schematic illustration of photovoltaic device

The PV membrane is constructed from semiconductor materials, and on absorption of photons, electrons from the valence band will be promoted into the conduction band and electrons and holes will migrate to the anode and cathode respectively. Water can then be oxidized and generate O_2 and H^+ at the anode, following by transferring H^+ to the cathode in order to generate H_2.

Photoelectrochemical cells involve the external electrical connection of usually a photoanode and cathode with an intervening electrolyte.[9, 16] The direct light absorption device is without the formal external connection and uses a proton conducting membrane to complete the circuit and overall water splitting reaction.[8] Comparing the two concepts of photovoltaics, the direct light absorption device has higher development potential because of the relatively lower cost and simpler construction.

However, the efficiency of hydrogen production from water splitting materials is still low. Therefore, the field of semiconductor photocatalysts for water splitting to produce H_2 and O_2 requires further development.

1.4 Efficiency considerations

The low water splitting efficiency may be due to the demanding combination of physical and chemical property requirements such as chemical stability, visible light harvesting efficiency, corrosion resistance and long-lived e^-/h^+ generation.

Photocorrosion resistance is important for the photocatalyst to avoid photodegradation during reaction. If, the photocatalyst decomposes under light irradiation, such as CdS and ZnO shown in eqn (1) [17] and (2), then the photocatalyst is corroded.

$$CdS + 2O_2 \rightarrow Cd^{2+} + SO_4^{2-} \quad (1)$$

$$ZnO + H_2O \rightarrow Zn(OH)_2 + O_2 \quad (2)$$

The photocatalyst should also have high thermal chemical stability to prevent any reaction with the reaction media such as water, acid/base buffer and organic solvent (i.e. methanol) if present. High crystallinity of the photocatalyst is preferred because defects reduce the electron-hole diffusion length and promote electron-hole recombination. It is crucial that the excited electron and hole should have sufficiently long lifetime for migration, so that they can be separated and diffuse to the surface of the photocatalyst. Furthermore, the surface structure should selectively catalyze the desired reduction and oxidation reactions. Clearly these are a demanding set of criteria.

1.5 Materials for photocatalysis and related processes

Fujishima and Honda first discovered that the semiconductor TiO_2 could be used for the photoelectrochemical water splitting reaction.[18] They showed that the presence of TiO_2 as the anode and platinum as the cathode can separate water into dihydrogen and dioxygen under illumination with UV light (Fig. 1.5). Based on this, further investigation on the photocatalytic activity of TiO_2 and many other kinds of metal oxides has occurred in device and powder form without the use of an external electrical circuit.

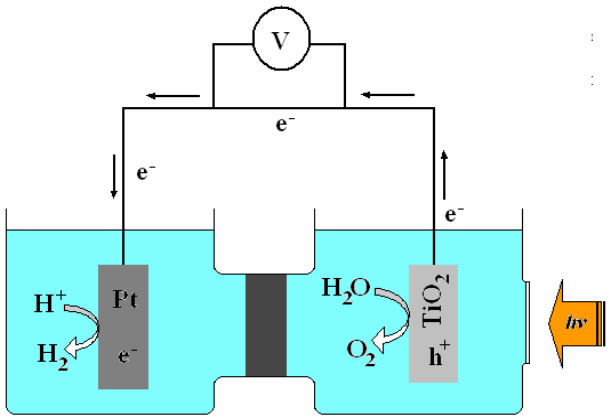

Fig. 1.5. Electrochemical cell with TiO_2 as the anode and platinum as the cathode

Since the activities of pure oxide materials are low due to the effect of a large band gap and efficient electron/hole recombination, ion doping and co-catalyst loading (i.e. Pt, NiO) are applied to enhance the photocatalytic activity, by changing the band positions to reducing the band gap and acting as a sink for photogenerated electrons to enhance electron/hole separation, respectively. Fig. 1.6 illustrates the ion doping and co-catalyst loading strategies for photocatalytic activity enhancement.

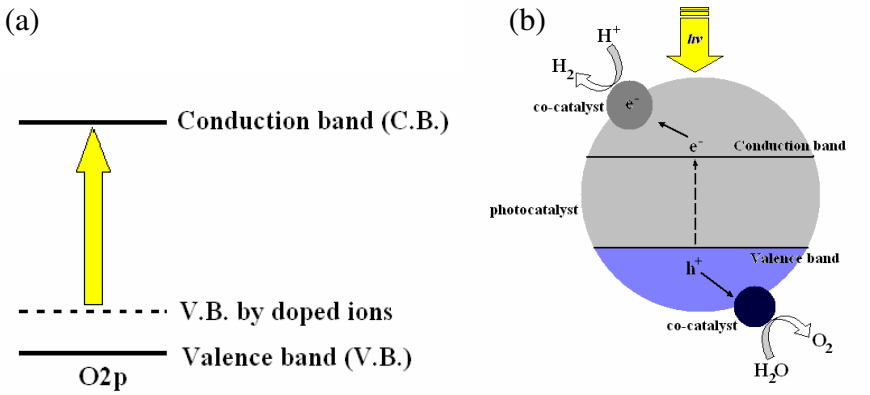

Fig. 1.6 a) band structure of ion doped photocatalyst; b) co-catalyst loaded photocatalyst

In a recent review by Osterloh[19] on photochemical water splitting using powdered photocatalysts it was concluded that only d^0 or d^{10} ions such as Ta(V), Ti(IV) and Nb(V) (d^0) or In(III), Ga(III) and Sn(IV) (d^{10}) etc. can induce the photochemical water splitting reaction. Many different types of metal oxides and their doped or co-catalyst loaded materials are summarized, for example, titanium oxide (TiO_2) and its derivatives (e,g. $SrTiO_3$, $PbTiO_3$), tantalum oxide and

tantalates (e.g. $SrTa_2O_6$, $K_2La_{2/3}Ta_2O_7$) and gallium phosphide (GaP). The best materials so far discovered which are active under visible light (λ>400nm) without sacrificial reagents are NiO/RuO_2-Ni:$InTaO_4$[20] and Cr/Rh-GaN:ZnO[21]. Typical co-catalysts for hydrogen and oxygen production are platinum (Pt), nickel oxide (NiO) and ruthenium dioxide (RuO_2). However, the evolution of H_2 and O_2 from these oxide materials is still low due to the effect of defect states that provide recombination centres and cause the rapid recombination of electron/hole pairs and lack of absorption in the visible light region. Furthermore, very little is known of the catalytic surface chemistry. Therefore, more research on co-catalysts, ion doping, crystal morphology and new semiconductor materials is needed to further enhance photocatalytic activities.

Because visible light constitutes the majority of solar energy at the Earth's surface, the development of visible light for water splitting photocatalytic activity is crucial. Nonetheless, the most studied photocatalysts are large band gap metal oxides, which are unable to function under visible light irradiation. Thus, ion doping reduces the band gap of oxide materials is an indispensable way for harvesting visible light from solar energy. Doping with cations or anions can reduce the band gap and achieve visible light absorption (Fig. 1.6a).

However, cation doping introduces defects which could also act as a recombination centres and accelerate the electron/hole recombination. Therefore, stoichiometric modification of the valence band with other elements (i.e. N, S) has also been investigated for visible light absorption, resulting in a higher valence band level, which reduces the corresponding band gap as shown in Fig. 1.7.

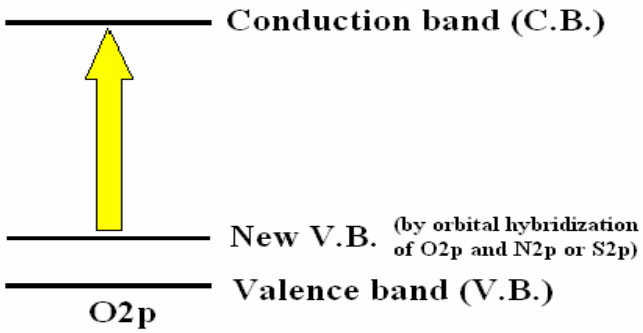

Fig. 1.7 Valence band modification

Relevant to this thesis, tantalum (oxy)nitride and tantalum nitride have been investigated and compared with tantalum oxide using sacrificial agents for hydrogen and oxygen generation. Fig. 1.8 illustrates the band energies of Ta_2O_5, TaON and Ta_3N_5 and Table 1.1 summarizes the photocatalytic activities of metal (oxy)nitride and nitride compounds.[22]

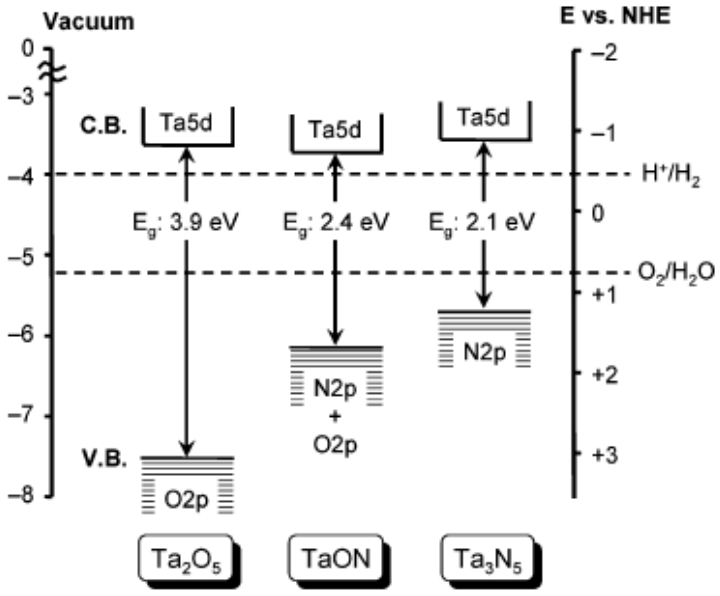

Fig. 1.8. Band structures of Ta_2O_5, TaON and Ta_3N_5

Table 1.1 H_2 and O_2 evolution using TaON and Ta_3N_5 in the presence of sacrificial reagents under visible light.[22]

		Activity (μmol/h)	
Photocatalyst[a]	Band gap energy (eV)[b]	H_2 evolution[c]	O_2 evolution[d]
TaON	2.5	20	660
Ta_3N_5	2.1	10	420

[a] Reaction conditions: 0.2-0.4 g of catalyst, 200 mL of aqueous solution containing sacrificial reagents, 300W xenon lamp light source, Pyrex top irradiation-type reaction vessel with cutoff filter(λ<420nm). [b] Estimated from onset wavelength of diffuse reflectance spectra. [c] Loaded with nanoparticulate Pt as a cocatalyst; reacted in the presence of methanol (10 vol %) sacrificial reagent. [d] Sacrificial reagent: silver nitrate (0.01 M). [19]

The use of sacrificial agents is a common strategy to determine if a semiconductor is capable of generating hydrogen or oxygen. For measuring H_2 evolution, the sacrificial reagent must have less positive oxidation potential than water, so the generated hole (h^+) oxidizes the sacrificial reagent irreversibly. The most common

sacrificial reagent for H_2 evolution measurement is methanol. Similarly, for measuring O_2 evolution, the sacrificial reagent must have a less negative reduction potential than H^+, so that the generated electron (e^-) would reduce the sacrificial reagent instead of H^+. The most common sacrificial reagent for O_2 evolution measurement is silver cations. Since both reactions are at a lower overall potential than true water splitting, for a given photon energy, there will be a greater driving force for the sacrificial reactions. Fig. 1.9 demonstrates the principle of sacrificial reagent usage for photocatalytic gas evolution measurement.

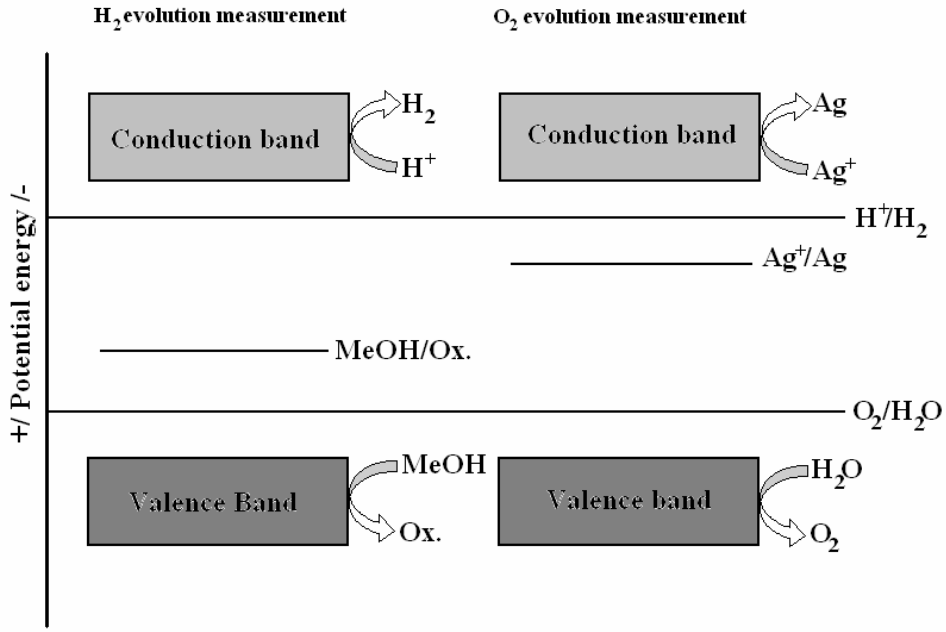

Fig. 1.9 Principle of sacrificial reagent presenting in the photocatalytic reaction

1.6 Modification of morphology to improve efficiency and photonic materials

The activities of many known photocatalysts for water splitting to produce hydrogen are still too low even with ion doping and addition of co-catalyst. In order to achieve higher catalytic activity, modification of the photocatalyst morphology and architecture is another feasible way. Many studies on morphology modification synthesize nanoparticles in order to increase the surface area of the photocatalyst, so more active sites are be exposed at the surface of the material and therefore increase the reactivity of the photocatalyst. Smaller particles can also provide shorter electron-hole diffusion pathways to the surface, which can reduce electron-hole recombination. A study of nanoparticles of tantalum(V) nitride has been reported by Domen.[19-20] The photocatalytic activity of hydrogen evolution of the tantalum(V) nitride nanoparticles is two times higher than the conventional material as shown in Fig. 1.10.

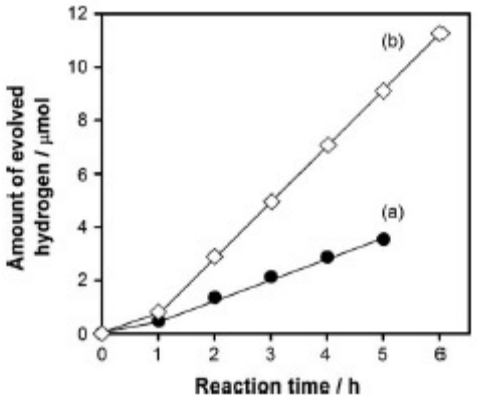

Fig. 1.10 H_2 evolution of (a) reference-Ta_3N_5 and (b) nanoparticle-Ta_3N_5 with the presence of methanol and Pt co-catalyst loaded. [23]

Nevertheless, because of the aggregation of the nanoparticles during reaction, it is still not an ideal morphology modification strategy. Hence, increasing the porosity of materials can also lead to more active sites (due to a larger surface area), capture more photons (due to the light scattering inside voids) and shorten the pathway of electron-hole diffusion to the surface of the photocatalyst (due to thinner wall thickness), which can result in better photocatalytic activity. Mesoporous materials have been studied for the water splitting reaction. For example a study of mesoporous TiO_2 and $InVO_4$ showed that the photocatalytic activities of the mesoporous materials are higher than the non-porous materials because of the presence of relatively higher surface area.[24]

Highly ordered macroporous materials have the potential for photocatalytic enhancement as well, not only because of the high surface area, short electron-hole diffusion pathway and increased photons absorption, but also the photonic properties which can potentially suppress the electron-hole recombination due to the photonic stop band. There are many studies on synthesizing marcoporous materials and determining their optical properties such as the stop band position.[25-30] However, the study of photocatalytic activities has rarely been investigated. A study by Ozin on methylene blue degradation by TiO_2 with binary sizes of pores improved the photocatalytic activities.[31] Macroporous $Ti_{1-x}Ta_xO_{2+x/2}$ (x=0.025, 0.05 and 0.075) photocatalytic activities for degradation of 4-nitrophenol has been reported by Wang.[32] It shows that the macroporous materials can enhance the photocatalytic degradation compare to the non-porous $Ti_{0.95}Ta_{0.05}O_{2.025}$ and Degussa P25. The principle of photonic solid on suppressing the electron-hole recombination is illustrated in Fig. 1.11.[33-35]

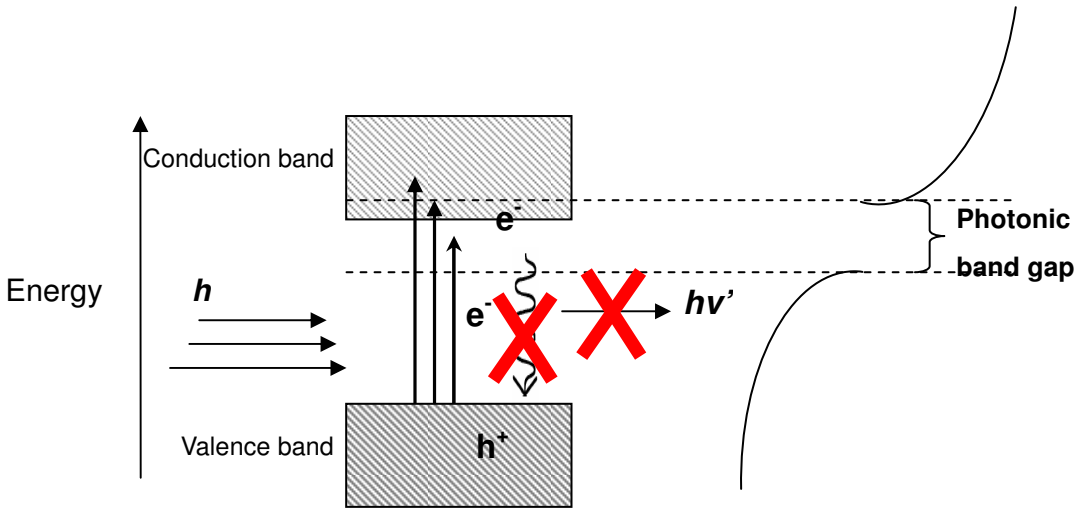

Fig. 1.11. Photonic stop band gap located at the edge of the conduction band which inhibits the photon emission and therefore electron-hole pairs' recombination is inhibited.

When a photon is absorbed by a semiconductor, an electron will be promoted to the conduction band. Due to the relative instability due to the large number of relaxation pathways, the electron can easily relax back to the valence band (electron-hole recombination) and simultaneously emit a photon. If a photonic band gap is located at the conduction band edge, then the emitted photon would be forbidden and hence, the recombination of electron-hole pairs could be inhibited. Different pore sizes of silica (SiO_2) have been studied and their relative stop bands (reflected wavelength) measured. The stop bands' wavelengths were found to be proportional to the pore size, and relative refractive indices of the framework and 'filling' medium (eq. 1.1 and 1.2). Therefore, the photonic property of porous materials can be tuned by changing the corresponding pore size and filling medium to obtain the desired photonic property of the material.[36]

$$\lambda = 2d_{hkl}/m\ [\varphi n_{wall} + (1-\varphi)n_{void}] \quad (1.1)$$

$$d_{hkl} = D(2)^{1/2}/(h^2+k^2+l^2)^{1/2} \quad (1.2)$$

λ: wavelength (nm)
d_{hkl}: interplanar spacing
m: order of Bragg diffraction
φ: volume fraction
n_{wall}: refractive index of wall material
n_{void}: refractive index of void space (solvent)
D: pore spacing

In light of the ease of control and determination of material properties, ordered porous materials are desired. There are numerous synthetic strategies for generating ordered porous materials, the most common methods are: colloidal crystal templating, nanocrystal dispersion and core-shell sphere synthetic methods.[37-38] The colloidal crystal method (Fig. 1.12) was applied in this thesis and uses a close-packed monodisperse colloid as the template, such as silica, poly (methyl methacrylate) (PMMA) or polystyrene (PS). Subsequently, a metal precursor solution (e.g. titanium ethoxide in dried ethanol) is impregnated into the intersticial spaces of the sphere template and finally calcined to remove carbonaceous material. This method can be used to prepare ternary oxides such as $LaFeO_3$.[39]

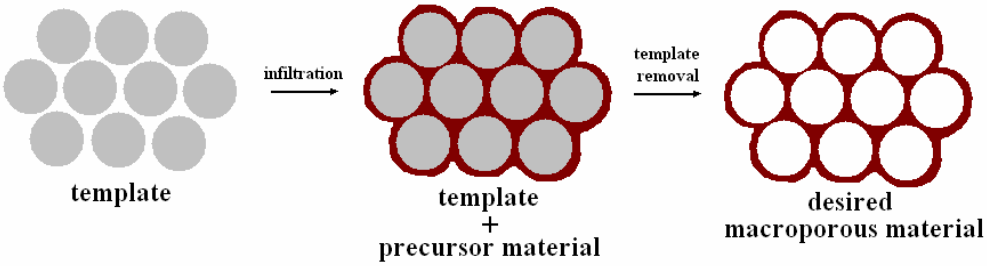

Fig. 1.12 Schematic illustration of colloidal crystal method

The nanocrystal dispersion (Fig. 1.13) method is where suspended nanoparticles in an emulsion of the template spheres are deposited on evaporation of the volatiles followed by calcination such as for SiO_2.[40]

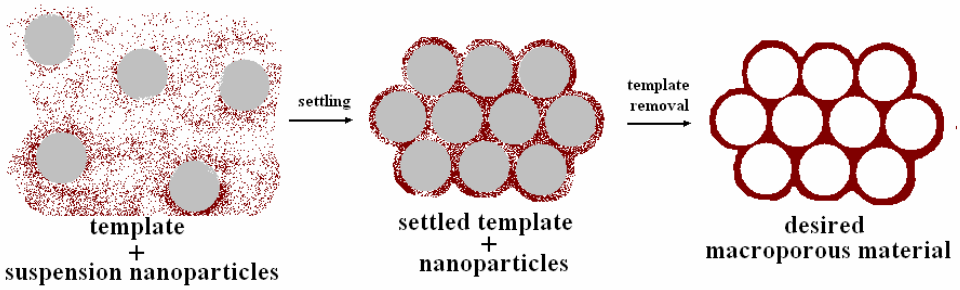

Fig. 1.13 Schematic illustration of nanocrystal dispersion method

Similarly, for the core-shell sphere synthetic method (Fig. 1.14), the spheres would be coated with a polyelectrolyte layer first and followed by coating of the precursor material (i.e. titanium isopropoxide). After drying the composite, calcination removes the template producing the macroporous material such as TiO_2.[41]

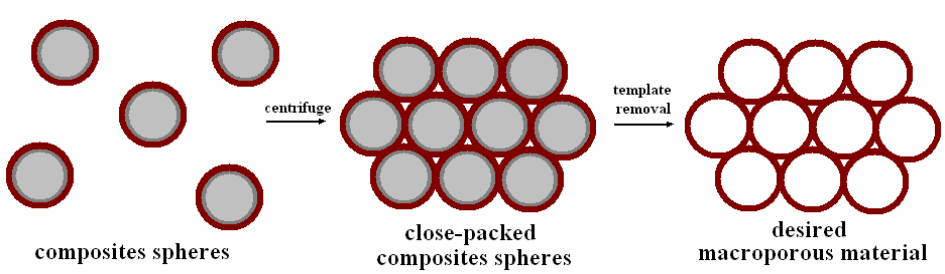

Fig. 1.14 Schematic illustration of core-shell sphere synthetic method

The most frequently used method is to impregnate a colloidal crystal of polystyrene.[38-40] Metal precursors are introduced into the interstitial spaces between the spheres as either molecules that can be hydrolysed or nanoparticles. Calcination or solvent extraction methods are applied for the removal of the organic spheres, resulting in the production of the desired porous material as mentioned above.

According to literature studies,[42-43] due to the mechanism of the formation of the polystyrene colloid, the diameter of polystyrene can be tuned by changing heating temperature, the amount of initiator, stirring speed and solvent. Styrene polymerization is typically initiated with potassium persulfate leading to oligomers that coagulate to form micelle-like spheres with a solidified core and a soft shell. The soft shell keeps growing until no monomer is left or the whole shell is solidified; consequently accomplishing the formation of a polystyrene sphere. To control the diameter of the polystyrene spheres, increasing the concentration of initiator, reaction temperature or decreasing concentration of monomer, the diameter of the ball will decrease. Also, it is important that the polystyrene spheres are homogeneous to form an ordered template, so high stirring speed is necessary to maintain an even dispersion during the polymerization process.

1.7 Considerations for photocatalytic reaction conditions

In recent decades, an increasing number of studies on photocatalytic materials have been reported. Since the efficiency of light harvesting is crucial for photocatalytic reactions, research has focused on new materials or modification of known materials to improve efficiency. Nowadays, many different kinds of new semiconductor materials have been developed, to meet criteria such as suitable band structure, visible light absorption, high crystallinity, low defect density and chemical stability etc., for both environmental applications and hydrogen production. For instance, ion doping, valence band and surface area modification

and addition of co-catalysts have been applied to enhance the photocatalytic activity. However, the operating reaction conditions will also significantly influence the photocatalytic activity because of different factors such as pH of the reaction environment, amount of photocatalyst, sacrificial reagent types, irradiance and scattering. It is therefore very difficult to compare one material to another as a defining set of reaction parameters is absent or not possible to obtain.[44]

1.7.1 Effect of pH

The pH is a measurement of the acidity of the solution, and its value represents the concentration of $[H_3O^+]$, where pH = -log $[H_3O^+]$. The pH is an important factor that would affect the photocatalytic activity, since the standard potentials of species would be changed with respect to pH of the solution due to the Nernst equation (1.3) and (1.4).

$$E = E^{\emptyset} - RT/\nu F \ (\ln K) \qquad (1.3)$$

$$K = [C]^c[D]^d/[A]^a[B]^b \qquad (1.4)$$

where,

E = potential of the system

$E^{\emptyset}$ = standard potential

R = constant ($8.314 JK^{-1}mol^{-1}$)

T = temperature

ν = the number of moles of electron involved in the system

F = Faraday constant ($9.648 \times 10^4 Cmol^{-1}$)

K = equilibrium constant ($aA + bB \rightarrow cC + dD$)

Furthermore, changes of the pH also change the surface potential of the photocatalyst via protonation of oxide and hydroxide moieties which modify the band bending and can increase or decrease the overpotential for redox chemistry. Thus, for different type of reactions, the pH can have very different effects. A study on TiO_2 photodegradation of methyl orange (MO) has been done by Devi[45] under different pH conditions. The activity of MO degradation is the highest at pH 6.6. This is due to the concentration ratio of $[MO^-]$, [HMO], [MOOH] and $[MO^+]$ present in the solution and adsorption to the photocatalyst. However, contrarily, for photocatalytic H_2 evolution reaction, the photocatalytic activity is higher in acidic solution when using acetic acid as an electron donor, which is reflective of the different mechanisms that operate in these two reactions.[46]

Variation in pH during synthesis can also affect the crystallinity, particle size and phase of a photocatalyst.[46-47] Applying hydrothermal synthetic methods for nano-titania crystalline powder, acidic conditions favor the formation of the brookite phase whereas basic conditions favor the formation of the anatase phase, where the activity is brookite > anatase > rutile.[47] The increase of pH also increases the crystallinity and purity of titania and as a result has higher photocatalytic activity. Similar effect has been observed on the hydrothermal synthesis of $BiVO_4$, where increasing the pH improves phase purity.[48] There is no evidence to suggest bulk phase transitions of the semiconductor as a function of pH, however it is possible surface reconstructions occur that could significantly effect catalysis.

1.7.2 Effect of photocatalyst concentration

The amount of photocatalyst used in the reaction would affect the photocatalytic activity not only because of the total active sites present, but also because attenuation of light absorption occurs as the concentration of photocatalyst increases.[49] For a study of 1%Pt/TiO_2 for hydrogen production, at low concentration the photocatalytic activity is proportional to the mass of photocatalyst whereas at higher concentrations the photocatalytic activity is no longer proportional to mass due to increased light scattering and attenuation.[45, 48] The photocatalytic hydrogen evolution activity increased from 0.04g/L to 0.31g/L but decreases after 0.31g/L. A similar observation has been observed in olive mill wastewater (OMW) degradation. It shows that the photocatalytic degradation rate by titania increases from 0.5g/L to 2g/L but then is slowed because the turbidity scatters the light, thus reducing photon absorption.[50]

1.7.3 Effect of amount of co-catalyst loading and composition

Although the addition of co-catalyst does enhance the photocatalytic activity, the amount of loaded co-catalyst has a non-linear effect on the enhancement. Theoretically, the greater the cocatalyst loading, the higher the photocatalytic activity until the optimum loading is reached. This is because the cocatalyst acts as an electron or hole sink to trap the migrated electron or hole and so suppress the recombination of electron and hole. Beyond the optimum coverage, the photocatalytic activity is no longer proportional to the amount of added cocatalyst, which is due to blocking of the light absorption of the semiconductor and/or the agglomeration of cocatalyst. These effects are semiconductor dependent.

A study on the effect of Pt loading on TiO_2 for photocatalytic reaction has been reported.[46] Results show that hydrogen production increases in the range of 0.2 to 1 wt% of Pt loading on titania, but reduces from 1 to 3 wt%. The increase of photocatalytic activity is due to the increase in the Schottky barriers arising from Pt nanoparticle loading, which rectify the junction current to lower voltage, helping to transfer the electron more easily to the cocatalyst from the photocatalyst and thus enhance the reactivity. Nevertheless, the depression of the photocatalytic hydrogen production activity is due to the coverage by excess Pt on the TiO_2 surface that blocks the light absorption.

Moreover, different types of metal loaded as cocatalyst would give different photocatalytic activity, which means that the optimum metal loading will differ in each case. A study on metal loading co-catalyst influence on hydrogen evolution has been reported by Puangpetch et al.[51] He suggested that the enhancement of the metal cocatalyst added depends on the electrochemical properties. The metal cocatalyst would enhance the photocatalytic activity if its electronegativity is higher than the metal from the photocatalyst, and vice versa. For example, from the study, for TiO_2 photocatalyst, Au, Ag, Pt and Ni cocatalyst loading enhance the photocatalytic hydrogen evolution, but Ce and Fe loading reduce the photocatalytic activity. This is due to the lower electronegativity of Ce and Fe compare to Ti.

1.7.4 Effect of sacrificial agents

Sacrificial agents are normally used as electron or hole scavengers to promote oxygen or hydrogen evolution respectively (see section 1.5). Scavengers can irreversibly react with the electron or hole instead of H^+ or H_2O, and therefore suppress the back reaction and the hydrogen or oxygen evolution can be measured. For hydrogen evolution, the effect of a series of alcohols as sacrificial reagents has been studied.[52] This study showed that methanol is the most active and gives the highest efficiency compared to other alcohols (ethanol, propanol and butanol). This is due to the steric hindrance of the larger alcohols, which would affect the oxygen lone-pair electron donation at the surface. Moreover, comparing other types of sacrificial reagents such as acetone, alcohol has much higher efficiency for the H_2 evolution reaction.[52]

1.7.5 Illumination methods

The light source and the reaction cell design are another important factor that would affect the photocatalytic activity. There are two types of common light source: xenon (Xe) and mercury (Hg) as they can emit continuous wavelength for the whole range of UV and visible light although the later has significantly greater UV output. The reaction cell design would also affect the photocatalytic activity as the light penetration varies due to the geometry of the reaction cell. In addition, for some reaction cell designs, foil is used to cover the whole cell to keep all photons in the reaction system, resulting in improved photocatalytic efficiency in comparison to a 'single pass' design.

For quantitative measurements, corrections should also be made for absorption by the reaction medium and scattering. The later can be estimated using similar sized particles of a material that does not absorb the wavelengths that induce photocatalysis. This is simple for visible light active systems but more problematic for UV active systems as most common materials absorb some UV photons.

1.8 Project aims

In this project, the aim is to synthesize macroporous solid state photocatalysts of metal compounds namely, tantalum oxide, tantalum oxynitride and tantalum nitride. Comparison of the photocatalytic activity of macroporous and non-porous materials under different conditions (e.g. co-catalysts and sacrificial reagents) will be performed. Scanning electron microscopy (SEM), transmission electron microscopy (TEM), Powder X-ray diffraction (PXRD), diffuse reflectance UV-Vis, diffuse absorbance UV-Vis and surface area measurement (BET) will be used for characterization.

According to the factors mentioned above, different conditions lead to very different photocatalytic activities for a particular semiconductor or composite. Therefore, it is important to clearly define the conditions under which a photocatalytic reaction is being performed. As part of this project we wished to examine the dependence of photocatalyst (Degussa P25) mass and concentration for our reactor.

Results and Discussion

Chapter 2

2.1 Synthesis of macroporous photonic crystals

In this thesis, the synthesis of macroporous photonic crystals was achieved using a common polystyrene templating method.[53] Briefly, homogeneous polystyrene spheres are packed into a face-centred cubic (fcc) opal structure and the interstitial sites are impregnated with a metal precursor. Hydrolysis and subsequent calcination gives the inverse opal macroporous solid, with pore size reflective of the polystyrene template.

Before synthesis of the polystyrene spheres by emulsifier free polymerization, the styrene monomer was washed by water and sodium hydroxide solution in order to remove the inhibitor which prevents styrene polymerization. The polymerization reaction was conducted under anaerobic conditions, as the polymerization is radical in nature and the initiator will react with oxygen from air, which will inhibit polymerization.

The polystyrene colloidal product was filtered through glass wool to remove larger polystyrene aggregates which prevent the formation of the close-packed polystyrene colloidal crystal. Centrifugation was applied for template preparation not only to accelerate the process, but also to improve the quality of the crystal packing. Subsequently, the crystalline polystyrene template is dried lower than its glass transition temperature, T_g (>100 ^oC) to prevent melting and the development of a rubbery appearance which prevents metal precursor impregnation. Fig. 2.1 shows SEM images of the polystyrene template with the (111) face of an fcc lattice.

Polystyrene was chosen as the template because of its ease of synthesis, tunable particle size and ease of removal at low temperature. The infiltration process of $Ta(OEt)_5$ was done under inert conditions using Schlenk techniques, as $Ta(OEt)_5$ is easily hydrolyzed in air by water to form insoluble Ta_2O_5 and impregnation cannot be completed.

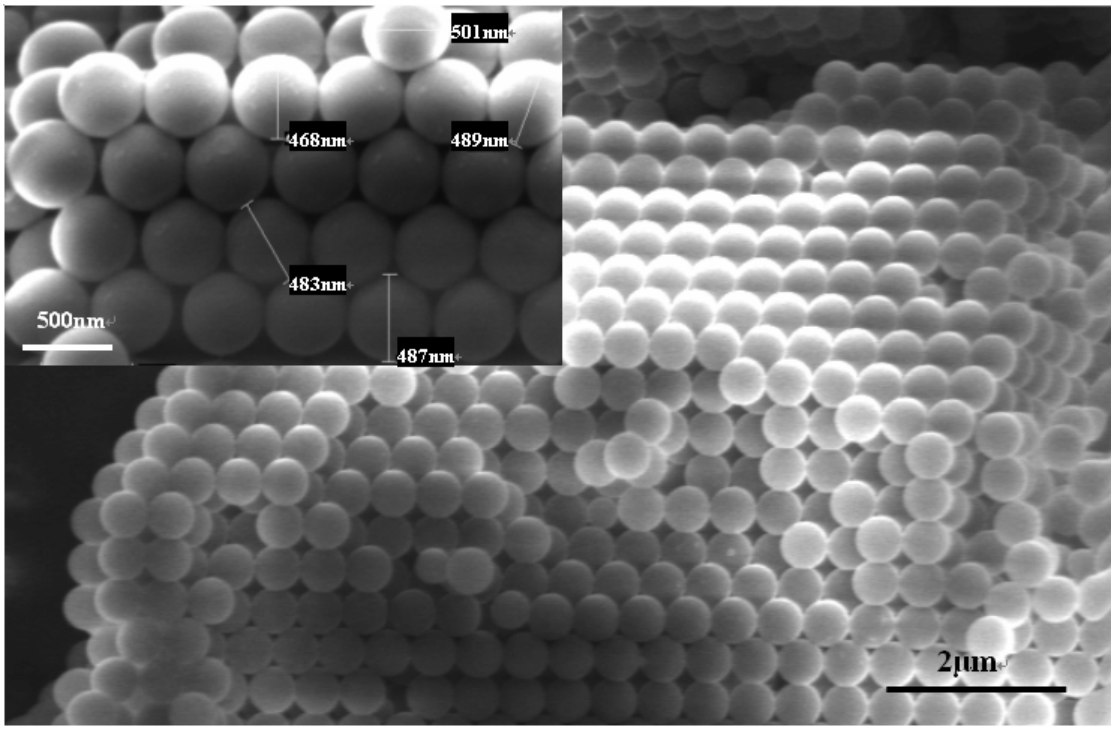

Fig. 2.1 SEM images of (a) PS (high mag.), (b) PS (low mag.)

A relatively high temperature (700 ^{o}C) was applied for calcination of the PS-precursor composite to ensure complete removal of the PS template and increase the crystallinity of the macroporous Ta_2O_5, as a crystalline oxide can increase the robustness of the macroporous structure, and prevent collapse on further treatment or modification. It was found that using 500nm PS template gave Ta_2O_5 with pore diameter of c.a. 370nm which is because of the physical shrinkage of the material during calcination.

Synthesis of tantalum(V) oxynitride and nitride were both performed under an ammonia atmosphere. However, the macroporous structure of Ta_2O_5 required accurate control of reaction conditions for TaON as it is the intermediate material between tantalum(V) oxide and tantalum(V) nitride.

$$Ta_2O_5 \rightleftharpoons TaON \rightleftharpoons Ta_3N_5$$

The formation of TaON relies on the equilibrium between nitridation of the oxide and hydrolysis of nitride respectively. An excess of water or ammonia in the reaction, leads to mixtures of Ta_2O_5 –TaON or TaON-Ta_3N_5 with different ratio.

$$3Ta_2O_5 + 10NH_3 \rightleftharpoons 2Ta_3N_5 + 15H_2O$$

The synthetic conditions of nitridation for the synthesis of macroporous TaON and Ta_3N_5 were milder in comparison to the bulk materials both in temperature and heating duration because of the volume fraction of the macroporous materials is much less than the bulk materials, so that the ammonia gas can pass through the whole material more easily and efficiently to undergo N^{3-} and O^{2-} ion exchange. It is also necessary, to heat the macroporous materials at a lower temperature than bulk solids to avoid pore collapse.

2.2 Addition of Pt cocatalyst

Platinum was chosen as the co-catalyst for H_2 evolution not only because of its high stability under the reaction conditions, but also because of its high conductivity that can efficiently trap the electron and act as a sufficient media to transfer the electron to the surface for reduction of H^+ to H_2. The easiest way to deposit Pt co-catalyst onto the photocatalyst surface is H_2 reduction of dispersed H_2PtCl_6. However, the main drawback is the inhomogeneous dispersion that occurs during the drying process under vacuum and aggregation of Pt is unavoidable.

Pt-citrate sol is a desirable method for the homogeneous dispersion of Pt co-catalyst. The Pt in the resulting Pt-citrate sol is protected by citrate to avoid aggregation. When mixing Pt-citrate sol with photocatalyst, sodium chloride (NaCl) was added to remove the protecting citrate group from Pt, and the photocatalyst must be washed with water to remove chloride ion. To ensure the removal of all chloride ion from the photocatalyst, testing by nitric acid and silver nitrate were used on the filtrate solution. The presence of chloride ion will cause the formation of white AgCl precipitate. The drawback of this deposition method is that the citrate sol is not removed from the Pt completely which would affect the photocatalytic activity of the materials. Therefore, further reduction by H_2 was used to ensure the complete removal of citrate sol.

2.3 Photocatalytic testing for H_2 evolution

For the measurement of H_2 evolution, sacrificial methanol was used because it would be oxidized instead of H_2O by h^+, so formation of O_2 would be suppressed and the recombination of H_2 and O_2 would not occur. Furthermore, oxidation of water is a difficult reaction which can cause suppression of H_2 production due to recombination of e^- and h^+ because the h^+ concentration increases. Measurements

were performed under Argon in a closed system. Since H_2 is much less dense than air, a closed system is used to avoid H_2 loss before entering the GC machine for quantitative measurement.

2.4 Characterization of Materials

2.3.1. Powder X-ray Diffraction

Fig.2.2 shows PXRD patterns of porous and non-porous Ta_2O_5, TaON and Ta_3N_5. The porous and non-porous materials are the same phases, however the broader peaks observed in the PXRD patterns of the porous materials imply that the crystallite size is smaller.

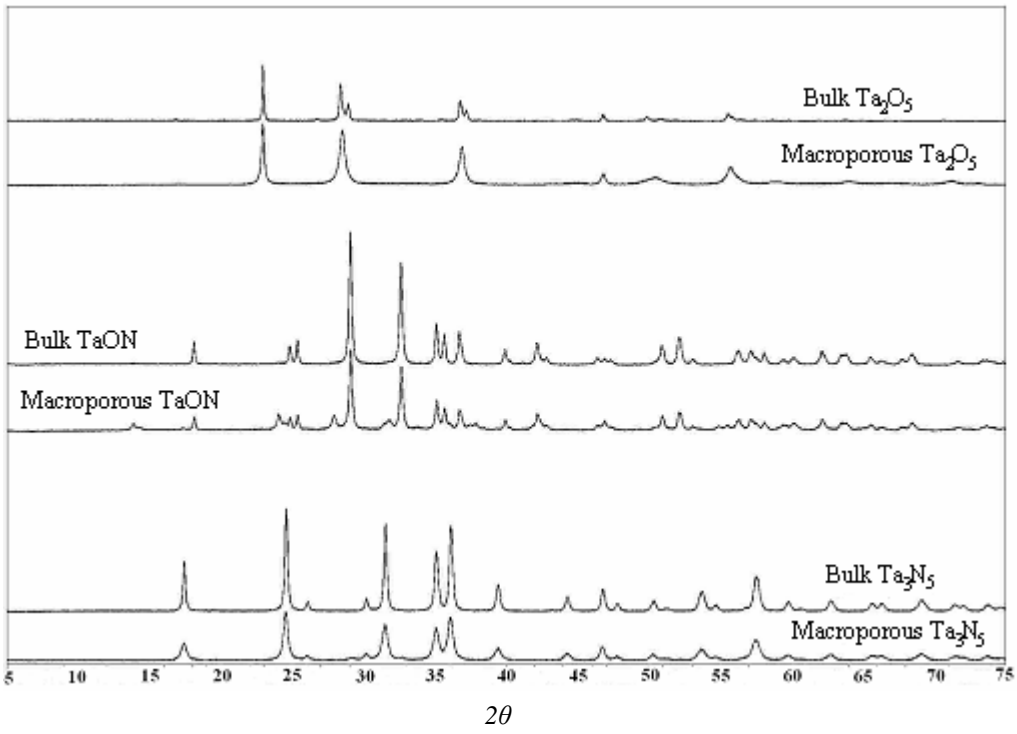

Fig. 2.2 PXRD of conventional and macroporous tantalum(V) oxide, oxynitride and nitride.

Comparing bulk to macroporous TaON the later exhibits extra peaks. The bulk TaON is the phase pure β-TaON polymorph, whereas macroporous TaON contains two phases of TaON, which are identified as the β- and γ-TaON polymorphs.[54] The difference is presumably due to the heating time of Ta_2O_5 to TaON where bulk TaON requires 15 hours wet NH_3 nitridation, whereas 6 hours are required for macroporous TaON. It has been shown that the γ-TaON phase is observed at

lower temperature, shorter heating time and lower total pressure, although phase pure γ-TaON has not been obtained.[54] To investigate the effect of heating duration on TaON synthesis, three samples were prepared heating between 4-8 hr as shown in Fig. 2.3.

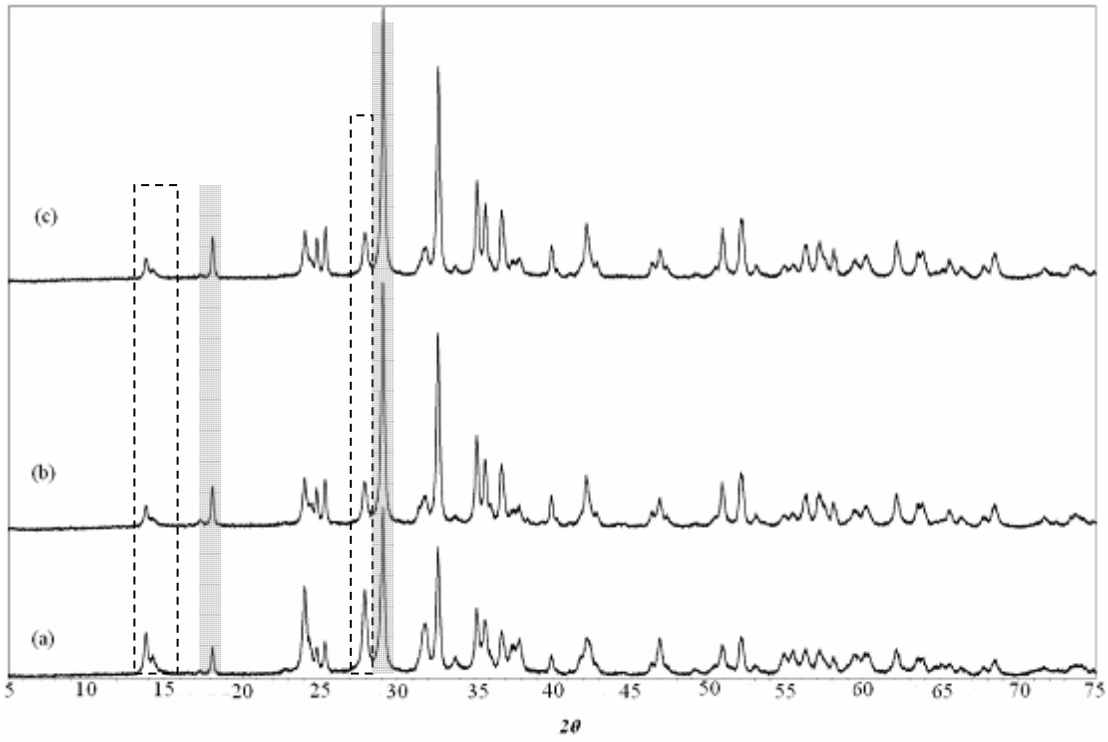

Fig. 2.3 Synthesis of macroporous TaON for different durations; a) 4 hr; b) 6 hr; c) 8 hr. Peaks within the dashed boxes are from γ-TaON; highlighted grey areas represent part of the peaks from β-TaON.

As shown in Fig. 2.3, the peak intensity from γ-TaON is reducing with respect to longer heating time.

The TaON crystallite size can be estimated from the PXRD using the Scherrer equation (2.1) [55]:

$$\tau = \frac{K\lambda}{\beta \cos\theta} \tag{2.1}$$

where K is shape factor
λ is x-ray wavelength
β is the full width half maximum value (FWHM) in radians
θ is Bragg angle

τ is particle size in nanometre(nm)

The crystallite size calculation results are shown in the table below:

	β	θ	τ(particle size (nm))
Bulk Ta_2O_5	$2.36x10^{-3}$	11.47	59.90
Macroporous Ta_2O_5	$3.50x10^{-3}$	11.51	40.37
Bulk TaON	$3.88x10^{-3}$	14.54	36.90
Macroporous TaON	$4.27x10^{-3}$	14.57	33.55
Bulk Ta_3N_5	$3.10x10^{-3}$	12.29	35.47
Macroporous Ta_3N_5	$7.79x10^{-3}$	12.31	18.23

Table 2.1: Crystallite size calculation results of bulk and macroporous Ta_2O_5, TaON and Ta_3N_5. Calculation is based on the most intense peak from PXRD with 2θ of Ta_2O_5, TaON and Ta_3N_5 are 23°, 29° and 25° respectively.

The calculated results show that the crystallite size of bulk and marcroporous tantalum compounds decrease across the series Ta_2O_5 > TaON > Ta_3N_5. This is consistent with ion exchange of the O^{2-} ion by N^{3-} during the Nitridaiton reaction which would cause structural strain and lead to fracture of the crystallites. A schematic representation is shown in Fig. 2.4.

The crystal structure of Ta_2O_5, TaON and Ta_3N_5 are quite different, where Ta_2O_5 exhibits an orthorhombic phase, TaON is monoclinic with a structure similar to baddeleyite and Ta_3N_5 is orthorhombic with a structure similar to anisovite.[56] Thus, it is a challenge to maintain the macropore structure during synthesis of TaON and Ta_3N_5 from Ta_2O_5 due to structural strain.

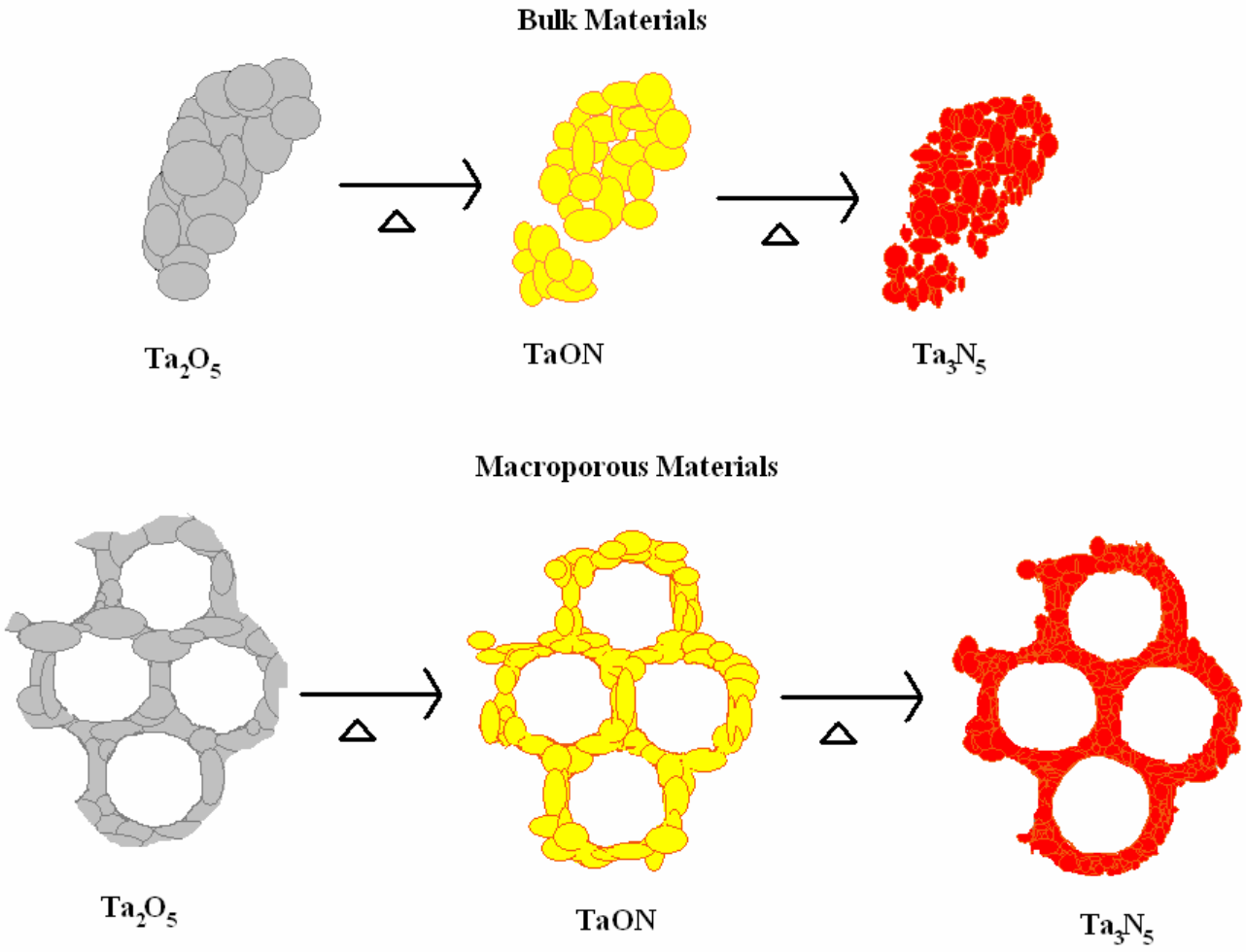

Fig. 2.4 Illustration of crystallite size reduction during nitridation of bulk and macroporous tantalum compounds.

Comparison between bulk and macroporous tantalum compounds, shows the calculated crystallite size of macroporous tantalum compounds is smaller than the bulk. This can be explained by the relative size of the precursor Ta_2O_5 crystallites compounds, which for the macroporous materials are prepared in the interstitial sites by hydrolysis and relatively low temperature sintering during the calcination process.

2.4.2. Electron Microscopy

Fig. 2.5 and 2.6 show SEM images of bulk Ta_2O_5, TaON and Ta_3N_5 and their macroporous analogues respectively. The SEM images of the bulk materials (Fig. 2.5) show that the particle size decreases on ion exchange as indicated from the crystallite size changes observed in the PXRD.

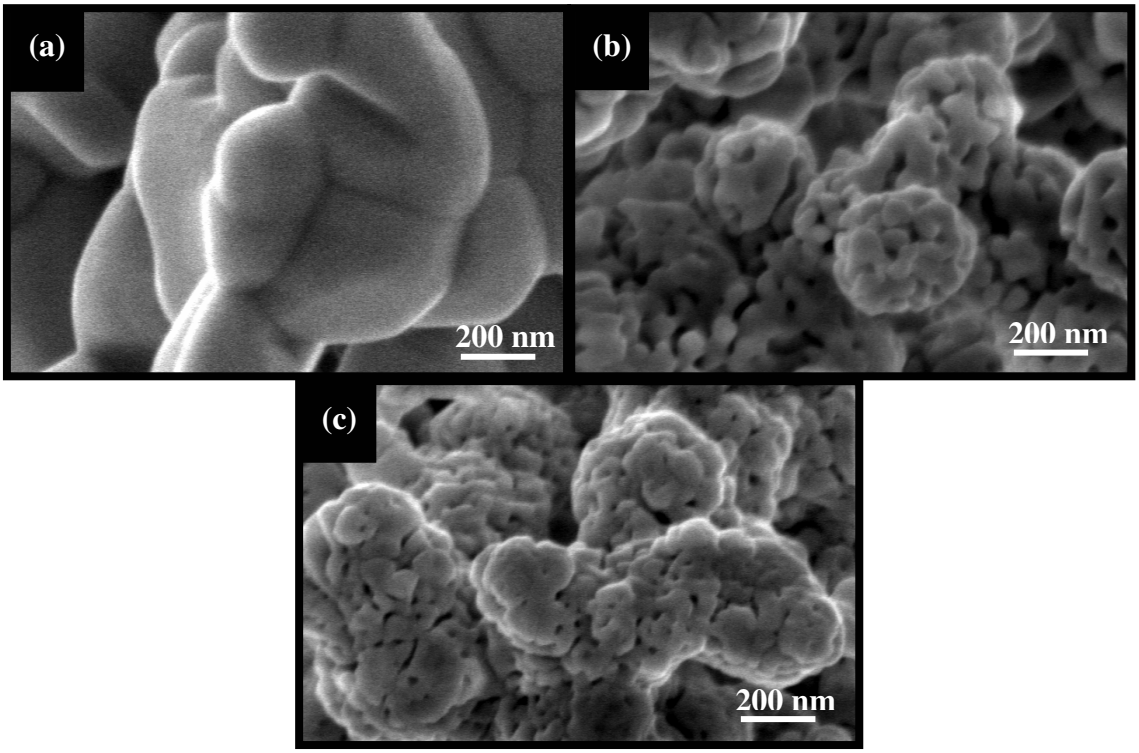

Fig. 2.5 SEM of a) bulk Ta_2O_5; b) bulk TaON; c) bulk Ta_3N_5

Fig 2.6 shows that as expected the periodicity of the macroporous structure is consistent with the (111) face of an fcc lattice. The relative pore size of Ta_2O_5 is 370±10 nm and the wall thickness is 70±5 nm, whereas the pore size and wall thickness of TaON and Ta_3N_5 are 380±10, 400±10, 60±5, and 60±5 nm respectively. It can also be seen that similar fragmentation occurred in macroporous materials as observed for the bulk examples.

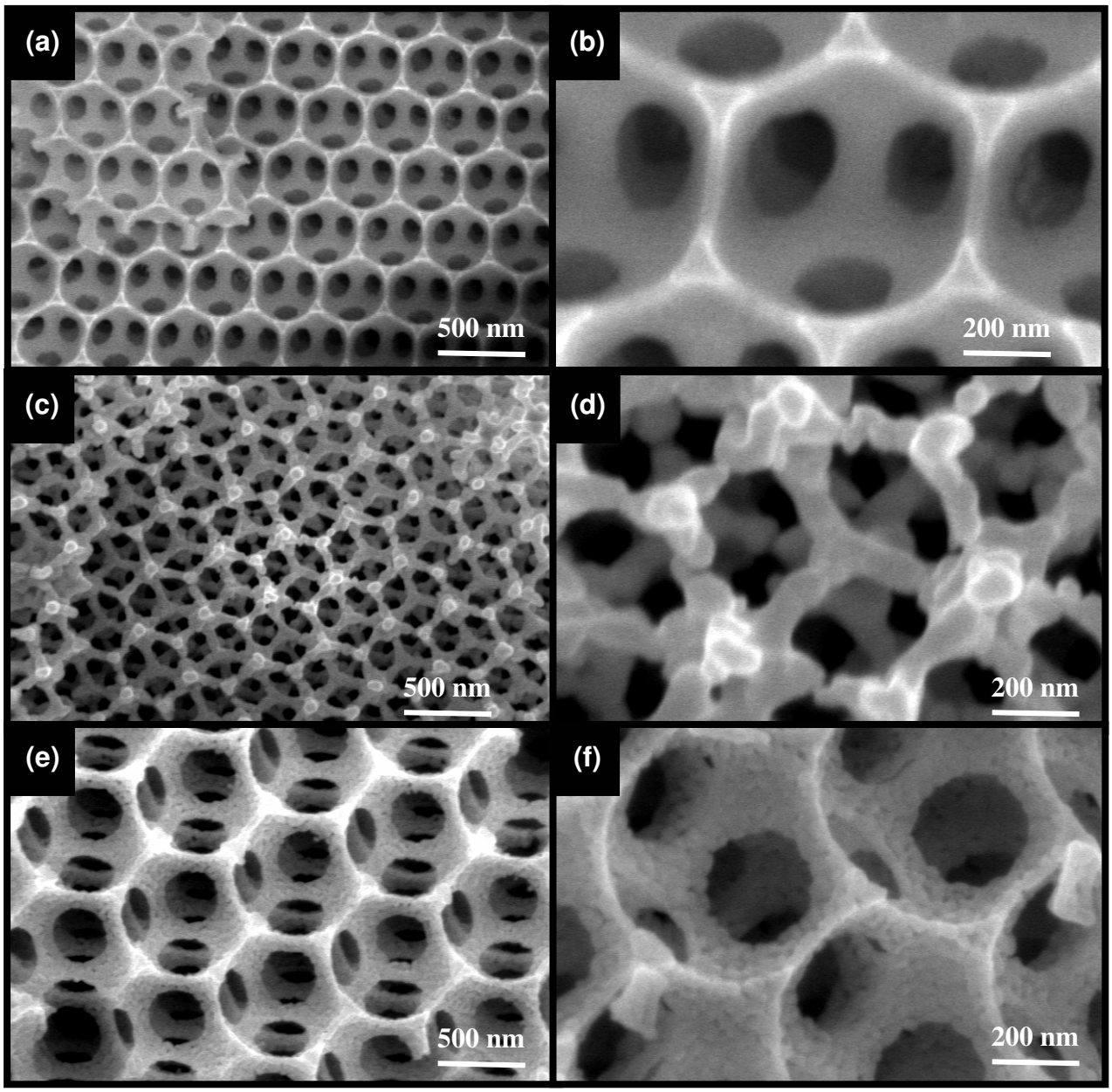

Fig. 2.6 SEM images of macroporous a) Ta_2O_5 (low mag.); b) Ta_2O_5 (high mag.); c) TaON (low mag.); d) TaON (high mag.); a) Ta_3N_5 (low mag.); b) Ta_3N_5 (high mag.)

Based on the SEM data, the pore size slightly increases on nitridation, whereas the wall thicknesses are very similar within error. Measurement errors of pore sizes and wall thicknesses can be caused by manipulation errors or non-focussed images. To reduce the inaccuracy, wide areas of the materials have been investigated with various magnifications.

Fig. 2.7 shows TEM images of bulk and macroporous tantalum compounds. High resolution images were obtained and fragmentation can be clearly observed.

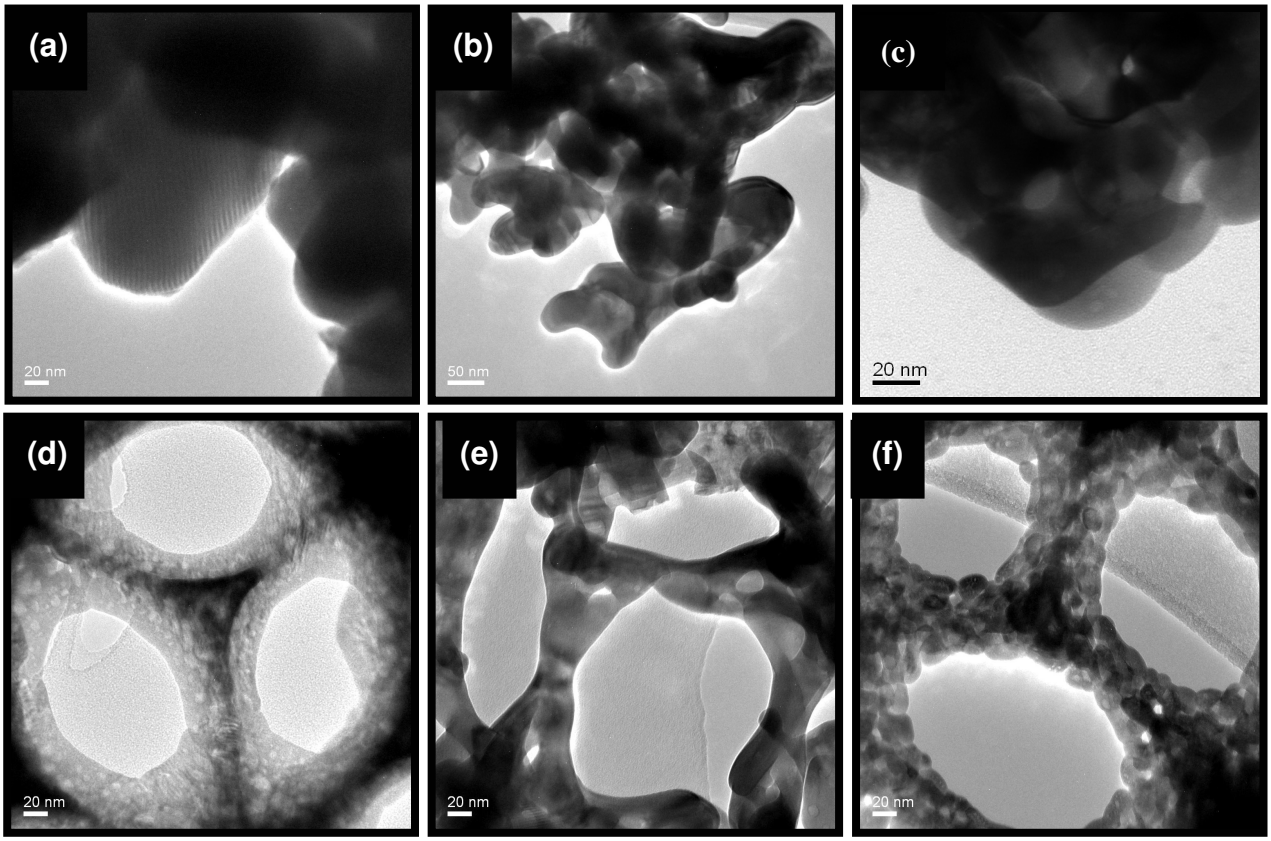

Fig. 2.7 TEM images of bulk a) Ta_2O_5; b) TaON; c) Ta_3N_5 and macroporous d) Ta_2O_5; e) TaON; f) Ta_3N_5

Fig. 2.8 shows the result of Pt co-catalyst deposition on bulk Ta_2O_5 and macroporous Ta_2O_5 by H_2 reduction of a H_2PtCl_6 dispersion. The diameter of Pt is in the range of 5 to 15nm.

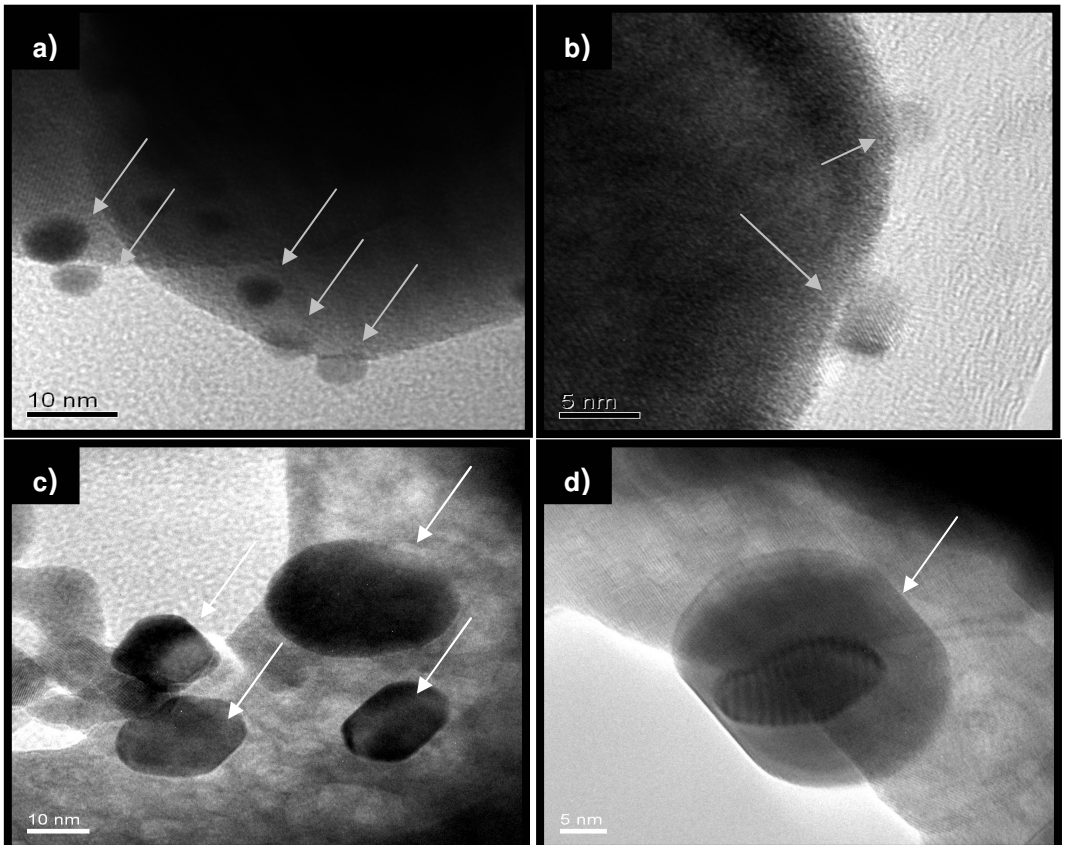

Fig. 2.8 0.5wt% Pt co-catalyst deposit on a&b) bulk Ta_2O_5; c&d) Macroporous Ta_2O_5 which Pt co-catalysts are pointed by grey and white arrows.

As shown in the images, the Pt distribution is not homogeneous and the particles are of various sizes. This is caused by inhomogeneous dispersion during the deposition process or aggregation of Pt particles during the reduction process. Unfortunately time prevented the extensive use of the Pt citrate sol deposition method, which may lead to a more homogeneous dispersion of more homogeneous Pt nanoparticles. However this method was used and tested for the Ta_2O_5 samples.

2.4.3. Surface Area Measurement

Table 2.2 shows the surface area of each bulk and macroporous Ta_2O_5, TaON and Ta_3N_5. From the BET surface area measurement results, the surface area of porous Ta_2O_5 is ca. 10 times higher than the non-porous Ta_2O_5; porous TaON is ca. 4 times higher than the non-porous TaON and porous Ta_3N_5 is ca. 3 times higher than the non-porous Ta_3N_5.

Table 2.2. Summary table of BET surface area of bulk and macroporous Ta_2O_5, TaON and Ta_3N_5.

BET surface area measurement (m^2/g)			
	Ta_2O_5	TaON	Ta_3N_5
Bulk	1.35±0.03	3.22±0.15	7.91±0.17
Macroporous	11.53±0.13	12.12±0.04	22.98±0.14

In general, the surface areas of tantalum materials follow the trend Ta_2O_5 < TaON < Ta_3N_5, which is in agreement with the electron microscopy images that show increasing fragmentation on nitridation. Much larger surface areas are observed for macroporous materials compared to the bulk compounds due to the wall thickness of the macroporous materials and lower particle-crystallite size.

BET surface area measurement is based on the relative pressure (P/P_0) with respect to isothermal adsorption/desorption of materials using nitrogen gas. The surface area increase of macroporous materials from Ta_2O_5 to Ta_3N_5 (2 times) is less than for the bulk compounds (7 times). This observation can be explained by retention of the macroporous structure and densification of the walls as suggested by SEM, whereas nitridation of the bulk materials results in more extensive particle fragmentation.

2.4.4. Diffuse Reflectance and absorbance Uv-Vis Spectroscopy

Photonic stop bands can be observed by solid state diffuse reflectance UV-Vis spectroscopy. Using equation (2.1) (see section 1.6), the stop band position, from the Uv-Vis, and pore size, from the SEM can be used to determine the wall filling fraction φ of the macroporous material.

$$\lambda = 2d_{hkl}/m\ [\varphi n_{wall} + (1-\varphi)n_{void}] \qquad (2.1)$$

The existence of a stop band was initially investigated by measuring the reflectance of macroporous Ta_2O_5 filled with air and a range of liquids including water. Fig. 2.9 shows the clear evidence of three stop bands consistent with a periodic photonic structure that shifts on filling of the pores with different fluids. The three bands can be indexed to 111, 220 and 311 Bragg reflections respectively.

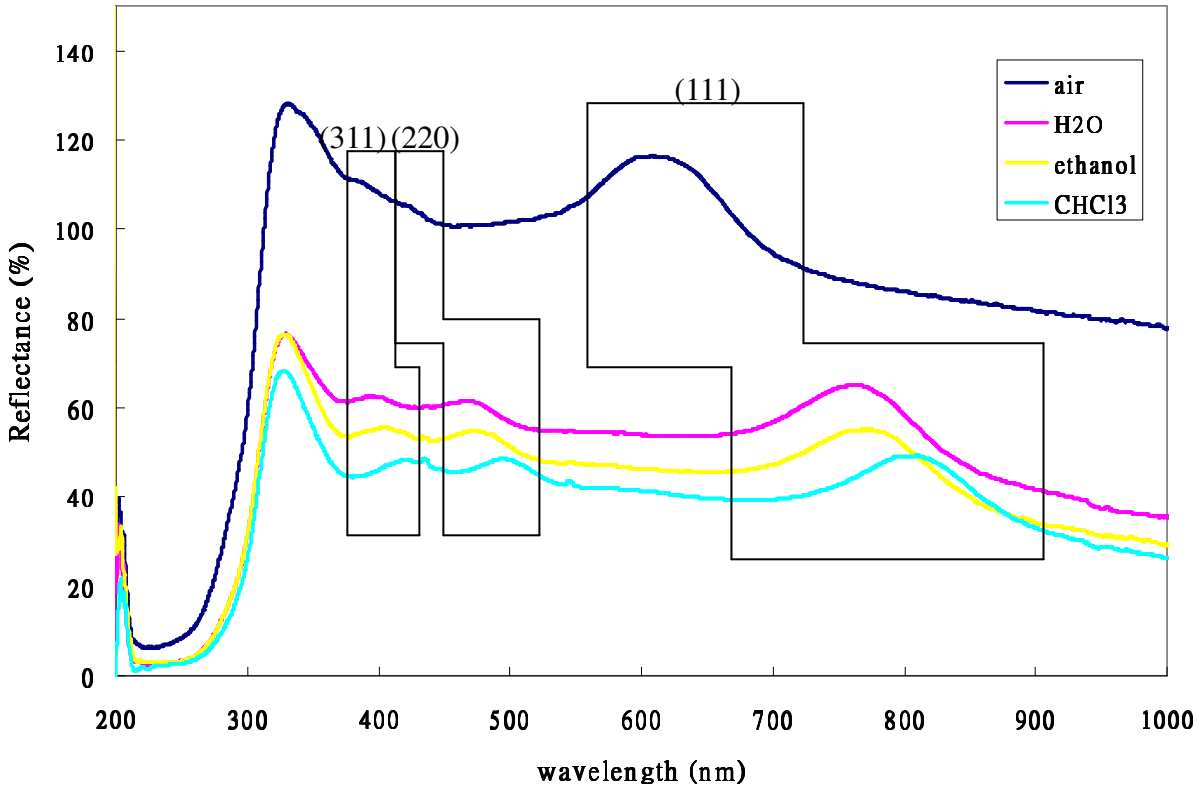

Fig. 2.9 Macroporous Ta_2O_5 reflectance filled with air, water, ethanol and chloroform respectively (original in colour).

As shown in Fig. 2.9, the stop band maxima are shifted to longer wavelengths along the series air < H_2O < ethanol < $CHCl_3$. According to equation 1, wavelength is proportional to n_{void} (refractive index of void/solvent filled) and the corresponding volume fraction (φ) can be calculated. Table 2.3 shows the theoretical refractive index of void/solvent and its related volume fraction.

Table 2.3.Refractive Index of air, water, ethanol and chloroform and the corresponding calculated volume fraction (φ) of Macroporous Ta_2O_5.

	Refractive Index	Ta_2O_5
Air	1.00	11.98%
Water	1.33	10.81%
Ethanol	1.36	9.63%
Chloroform	1.45	9.17%

The volume fractions of macroporous Ta_2O_5 are variable which can be explained by the degree of wetting between the surface of macroporous Ta_2O_5 and solvents. Using equation 2.1, φ has been calculated for macroporous Ta_2O_5, TaON and Ta_3N_5, the results are shown in Table 2.4

Table 2.4. Volume fraction of macroporous Ta_2O_5, TaON and Ta_3N_5 in percentage (%).

	Ta_2O_5	TaON	Ta_3N_5
Max. point of stop band	720.64	683.74	748.52
Refractive index	2.21	2.29	3.80
Volume fraction φ (%)	15.92	7.89	5.21

The volume fraction of tantalum compounds are: Ta_2O_5 > TaON > Ta_3N_5. The trend to decreased filling on nitridation is consistent with the PXRD and electron microscopy data, where slight pore expansion and wall densification is observed. However, possible errors exist in this calculation due to the determination of the maximum stop band position and also the value used for the refractive index. To reduce the errors, ideally the refractive index as a function of wavelength should be measured rather than a single value because the refractive index can change with respect to the wavelength of light absorption.

Comparison of the reflectance spectra between bulk and macroporous materials are shown in Fig. 2.10 and no stop band can be observed for bulk materials. The grey highlighted areas are the energy that is absorbed by the materials.

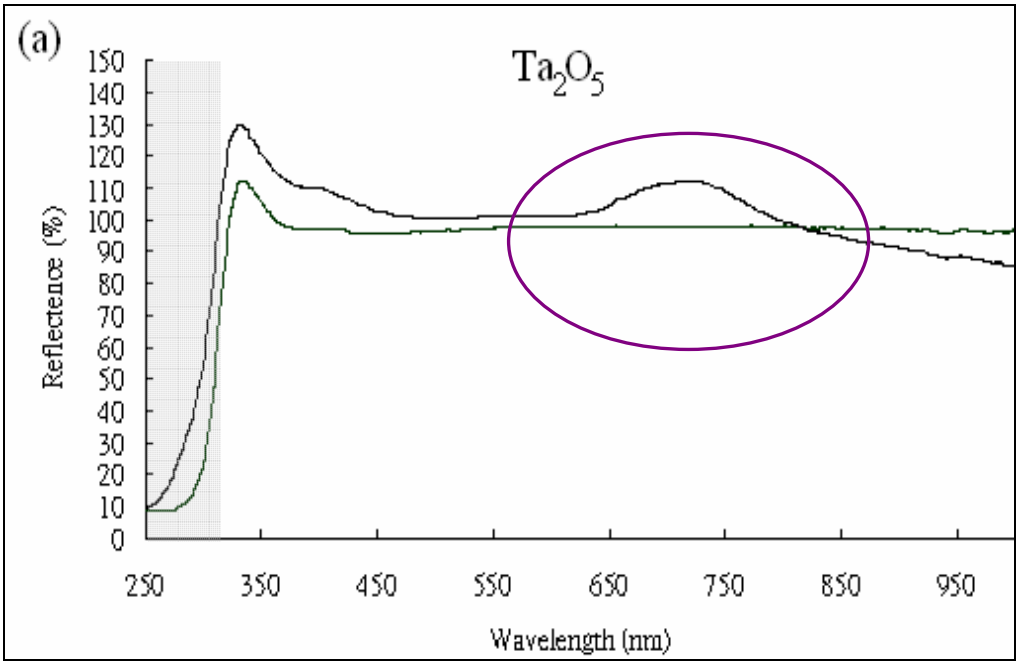

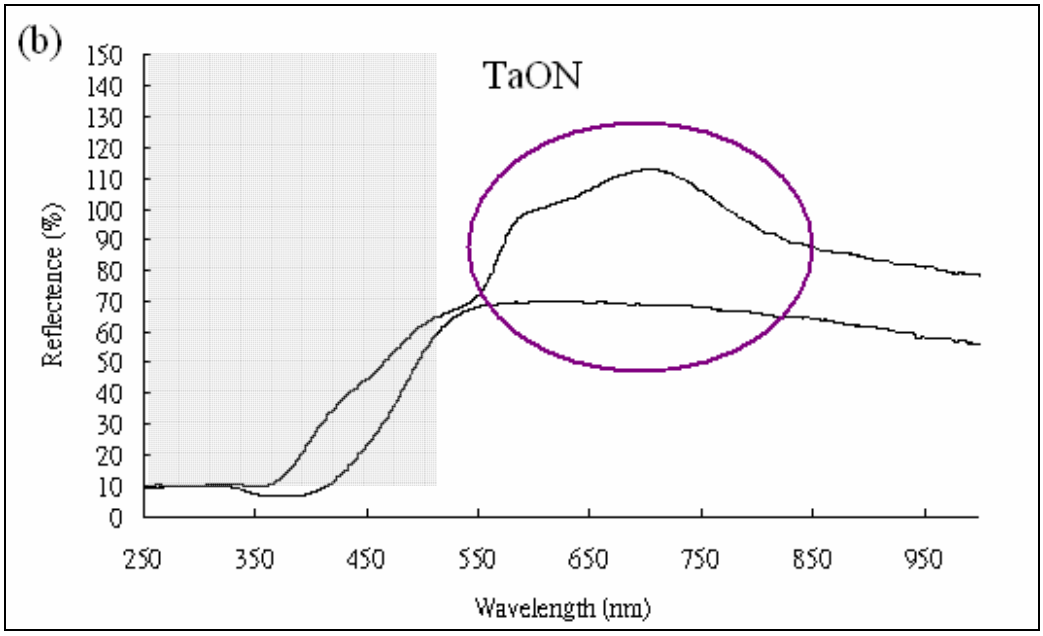

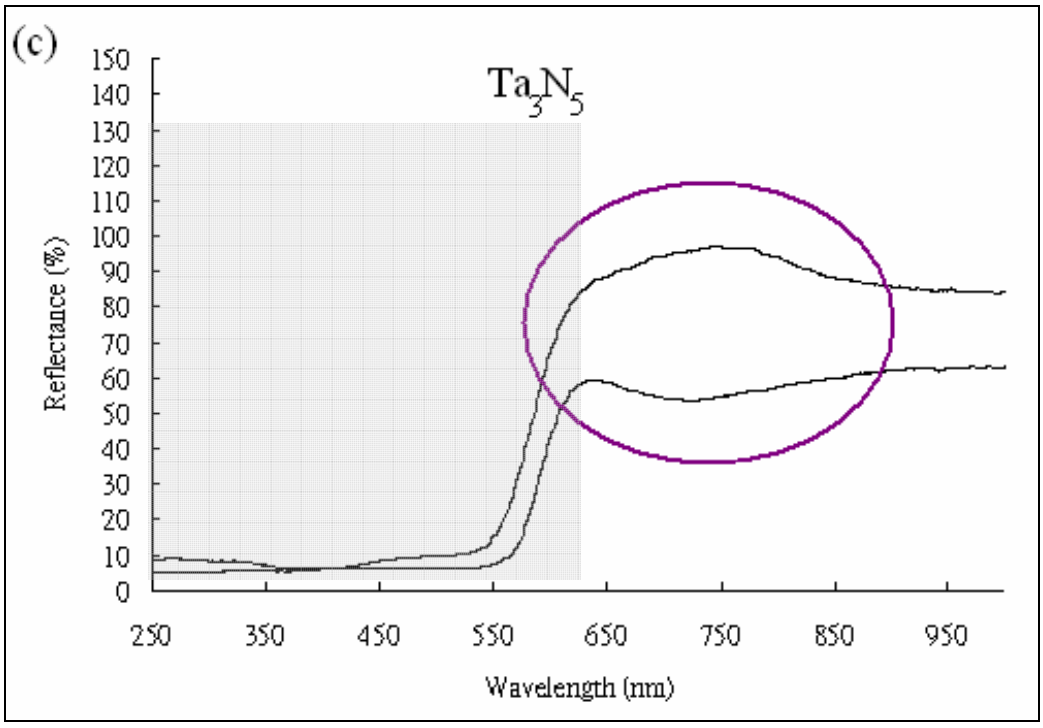

Fig. 2.10 Reflectance of a) Ta_2O_5; b) TaON and c) Ta_3N_5

It is also possible to determine the electronic band gap from the spectroscopic data and Fig. 2.11 shows the absorbance of macroporous Ta_2O_5, TaON and Ta_3N_5 and the vertical line indicates the wavelength used to calculate the band gap energy.

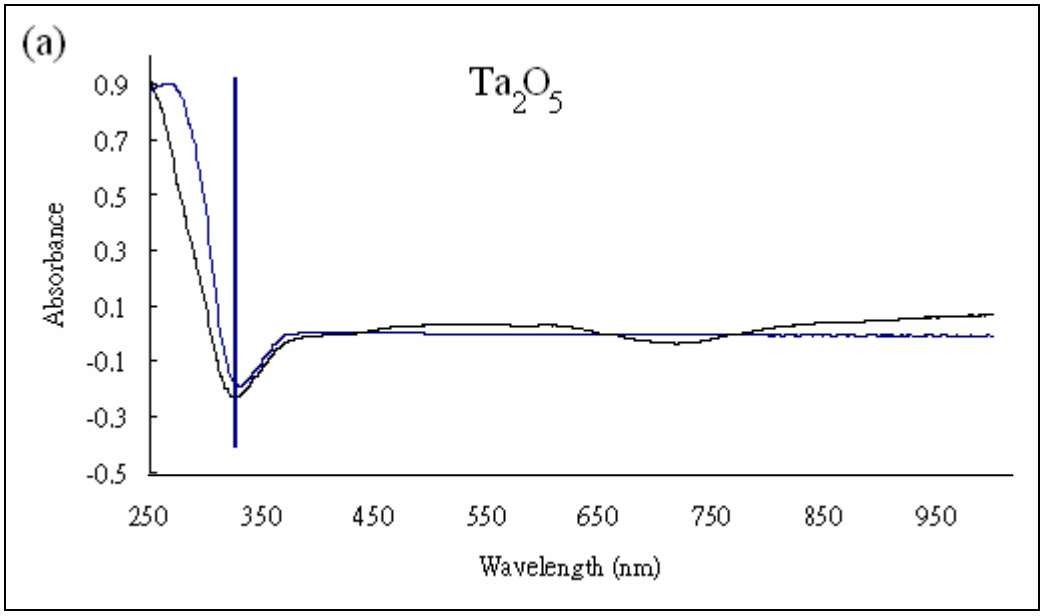

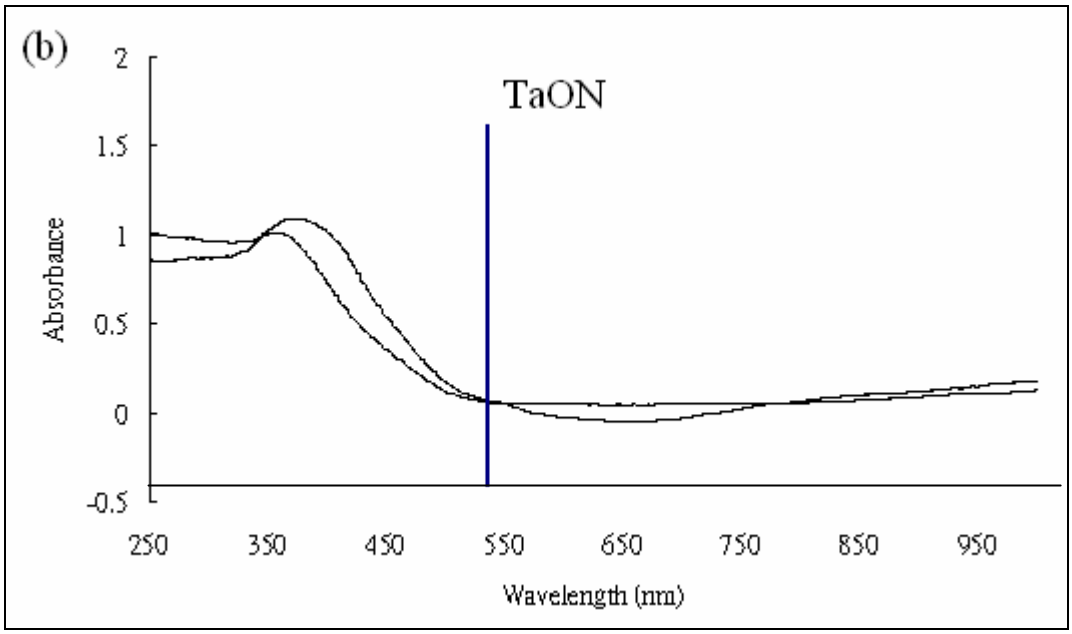

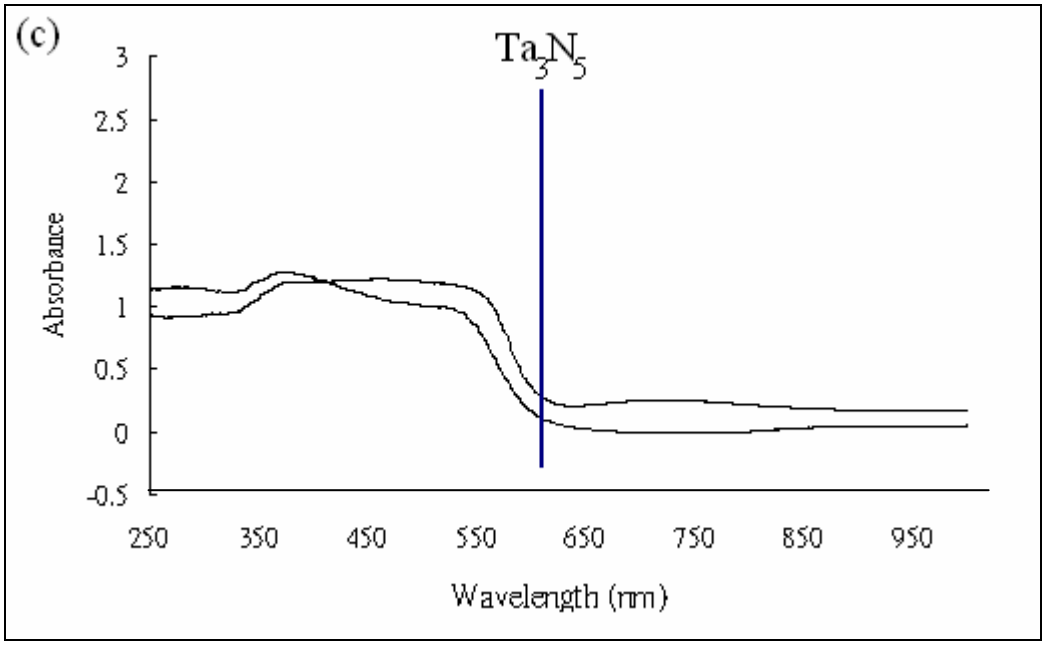

Fig.2.11 Absorbance of a) Ta_2O_5, b) TaON and c) Ta_3N_5.

Table 2.5 Summarizes the experimental values of band gap energy as shown below.

Summary Table 2.5			
	Ta_2O_5	TaON	Ta_3N_5
Absorption edge (nm)	325±10	525±10	625±10
Band gap energy (eV)	3.82±0.12	2.37±0.04	1.99±0.03

The absorption edge of bulk and macroporous Ta_2O_5, TaON and Ta_3N_5 are measured manually so possible errors are estimated in Table 2.5. The band gap energies of those compounds are calculated from the relevant absorption edges using the equation $E=hc/\lambda$.

The band gap decreases in a trend of Ta_2O_5> TaON > Ta_3N_5, this is because of the changes of valence band that N 2p is in higher potential energy than O 2p, but there is a similar potential energy of Ta 5d conduction band level for all compounds. For TaON, hybridization of O 2p and N 2p orbitals cause the overall valence band level increase and therefore decrease the band gap. Similarly, for Ta_3N_5, the valence band is purely constructed by N 2p, resulting in higher valence band level compared to TaON and hence Ta_3N_5 has the smallest band gap.

2.5 Photocatalytic Testing

As described in section 1.5, Ta based compounds have been shown to be active photocatalysts in the bulk phase. Ta_2O_5 and Ta_3N_5 have also been prepared as mesoporous materials and it was shown that the H_2 evolution photocatalytic activities of both mesoporous Ta_2O_5 and Ta_3N_5 are higher than the bulk materials.[57-58] The band gap and position of Ta_2O_5, TaON and Ta_3N_5 have been determined to span the reduction and oxidation of water and TaON and Ta_3N_5 can mediate both half reactions in the presence of a sacrificial agent. Although overall water splitting is not achieved these materials could be used as one component of a two component device. In this thesis hydrogen production was studied using methanol as the sacrificial agent.

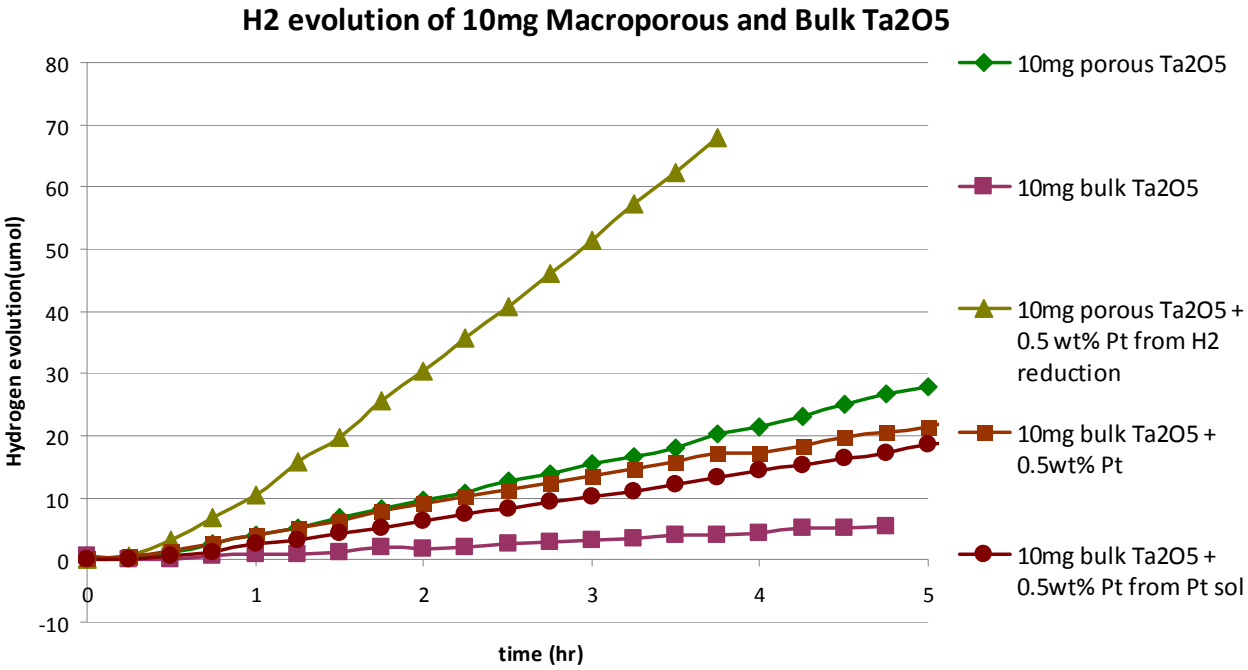

Fig. 2.12 Hydrogen evolution of bulk and macroporous Ta_2O_5 with/without presence of 0.5wt% Pt co-catalyst illuminated using Uv-Vis from a 300 W Xe lamp.

Fig.2.12 and Table 2.5 shows the photocatalytic H_2 evolution data of bulk Ta_2O_5, macroporous Ta_2O_5, bulk Pt-Ta_2O_5 and macroporous Pt-Ta_2O_5 and it was observed that H_2 evolution is in the order bulk Ta_2O_5 < bulk Pt-Ta_2O_5 < macroporous Ta_2O_5 < macroporous Pt-Ta_2O_5.

Table 2.6. H_2 evolution of Ta_2O_5 and Pt-Ta_2O_5 and the corresponding light absorption determined with a power meter.

Photocatalyst[a]	H_2 evolution after 4 hour photolysis (μmol)	Irradiance absorbed by photocatalyst (mW/cm^2)[b]
Bulk Ta_2O_5	4.39	329
Bulk Ta_2O_5 + 0.5wt% Pt by H_2 reduction	17.20	332
Bulk Ta_2O_5 + 0.5wt% Pt by Pt sol depositon	14.36	326
Macroporous Ta_2O_5	21.27	316
Macroporous Ta_2O_5 + 0.5wt% Pt by H_2 reduction	67.68	323

[a] 10 mg of catalyst in 110 mL of 100:10 water:methanol. [b] 300W Xe lamp measured with a power meter.

Fig. 2.13 and table 2.7 shows the photocatalytic H_2 evolution data of bulk TaON, macroporous TaON and macroporous 3 wt% Pt-TaON. 3 wt% of Pt co-catalyst used instead of 0.5 wt% and 40mg of samples were tested in order to increase the activity. There are several reports by Domen using TaON and several loadings of Pt.[59-61] The greatest activity is observed for 3 wt% TaON,[60, 62] which is a very large loading in comparison to many other systems that use Pt loadings << 1%. TaON has also been reported to exhibit visible light activity above 420 nm.[60-61] An analogous experiment with a 400 nm high band pass filter was performed which showed no evolution of H_2 (Fig. 2.13). It was observed that H_2 evolution occurs in the order bulk TaON < macroporous Pt-TaON < bulk Pt-TaON < macroporous TaON).

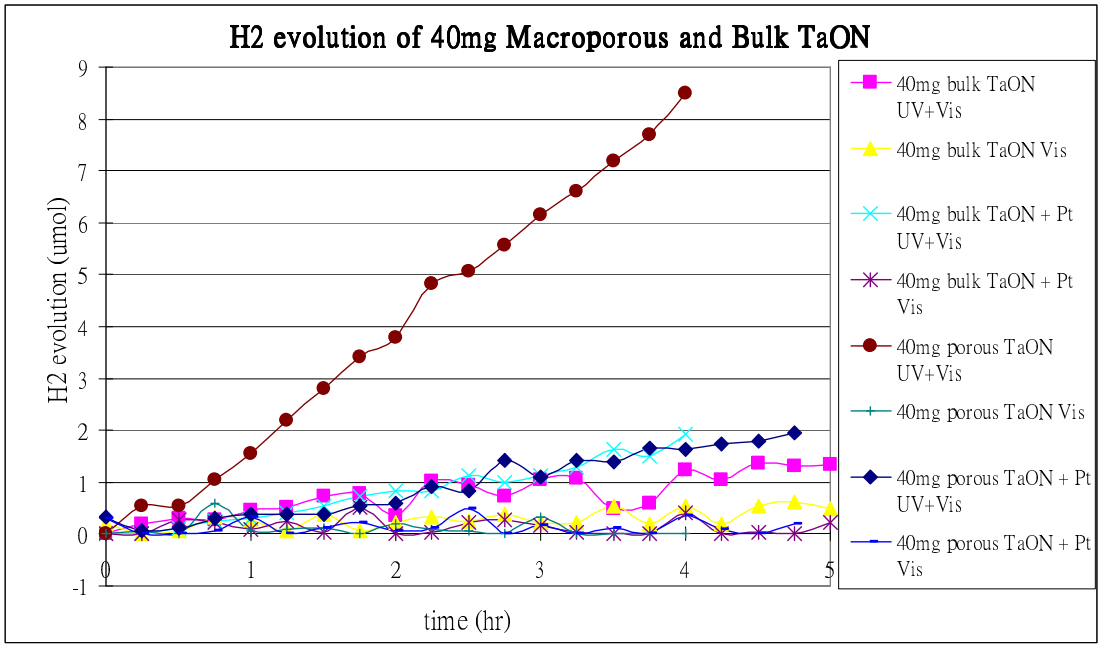

Fig. 2.13 Hydrogen evolution of bulk and macroporous TaON with and without presence of 3wt% Pt co-catalyst

Table 2.7. H_2 evolution of TaON and Pt-TaON and its corresponding light absorption

40mg Photocatalyst[a]	H_2 evolution after 4 hrs photolysis (μmol)		Irradiance absorbed by photocatalyst (mW/cm^2)[b]	
	UV+Vis	Vis	UV+Vis	Vis
Bulk TaON	1.23	0.53	300	111
Bulk TaON + 3wt% Pt by H_2 reduction	1.92	0.40	306	175
Macroporous TaON	8.49	0.33	409	189
Macroporous TaON + 3wt% Pt by H_2 reduction	1.63	0.34	384	192

[a] 40 mg of catalyst in 110 mL of 100:10 water:methanol. [b] 300W Xe lamp measured with a power meter.

Fig. 2.14 and table 2.8 show the photocatalytic H_2 evolution data of bulk Ta_3N_5, macroporous Ta_3N_5 and macroporous Pt-Ta_3N_5. Similar to TaON, Ta_2N_5 has also been shown to exhibit visible light activity.[60] An analogous experiment was performed using a 400 nm high band pass filter. Again no H_2 evolution was observed under these conditions. It was observed that H_2 evolution occurs in the order (bulk Ta_3N_5 < macroporous Pt-Ta_3N_5< macroporous Ta_3N_5 < bulk Pt-Ta_3N_5)

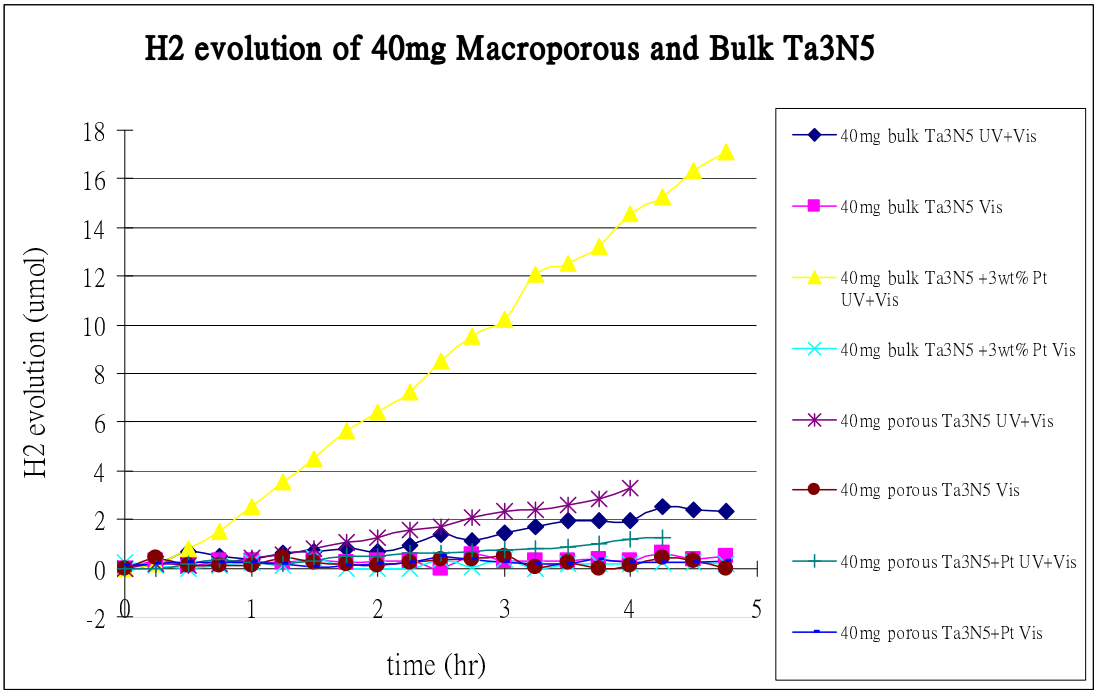

Fig. 2.14 Hydrogen evolution of bulk and macroporous Ta_3N_5 with/without presence of 3wt% Pt co-catalyst

Table 2.8. H_2 evolution of Ta_3N_5 and Pt-Ta_3N_5

40mg Photocatalyst [a]	H_2 evolution after 4 hrs photolysis (μmol)		Light absorbed by photocatalyst (mW/cm^2)[b]	
	UV+Vis	Vis	UV+Vis	Vis
Bulk Ta_3N_5	1.95	0.30	472	261
Bulk Ta_3N_5 + 3wt% Pt by H_2 reduction	14.54	0.16	466	284
Macroporous Ta_3N_5	3.32	0.13	351	158
Macroporous Ta_3N_5 + 3wt% Pt by H_2 reduction	1.21	0.22	326	132

[a] 40 mg of catalyst in 110 mL of 100:10 water:methanol. [b] 300W Xe lamp measured with a power meter.

From the above data it can be seen that the absolute activity of the macroporous materials is greater than the analogous bulk materials. However, Pt loading clearly leads to a range of results across the three materials in bulk and macroporous form. Addition of Pt to all the bulk materials results in an increase in activity, as expected from literature reports and in line with Pt being a cocatalyst. The most significant enhancement is observed for bulk Ta_3N_5. For macroporous materials addition of 0.5 wt% Pt to Ta_2O_5 increases the activity whereas for both TaON and Ta_3N_5 3 wt% Pt addition reduce activity. The implication from these data is that either the Pt is not dispersed through the macropores but is concentrated at the surface partially blocking the inner volume or that the Pt loading process results in loss of activity. Unfortunately time prevented the microscopic analysis of the 3 wt% loaded samples from appearing in this thesis but as seen in Fig 2.8 dispersion is not homogeneous and it is likely that much larger Pt particles may be present. With respect to the Pt loading process, hydrogen is used to reduce the deposited H_2PtCl_6 which could reduce the nitride surface to Ta^{3+}, which on exposure to air/water results in oxide formation. The macroporous materials are less crystalline and will therefore have a greater surface energy and reactivity. Nevertheless, for TaON the macroporous material is the most active of all the TaON based materials indicating that if Pt deposition can be controlled a significant increase in activity should be observed. In contrast to literature reports we did not observe any visible light activity for TaON or Ta_3N_5 when loaded with Pt cocatalyst. It is not clear why this is the case, although again the Pt loading method may be the key.

The surface area of the macroporous materials is greater and the photocatalytic results can be normalized against the surface area (Table 2.9). For Ta_2O_5 and Ta_3N_5, the activity of the macroporous materials per m^2 is lower; however, it seems reasonable to suggest that H_2 is occurring in the pores of all the macroporous materials and not just at the particle surface. In contrast to Ta_2O_5 and Ta_3N_5, for TaON, the activity of macroporous material is higher per m^2, which is possibly due to the presence of the γ-TaON phase which has not been previously tested for photocatalytic activity.

Table 2.9. Summary of bulk vs macroporous materials surface area and H_2 generation without Pt co-catalyst additon.

	Bulk vs Macroporous		
	Ta_2O_5	TaON	Ta_3N_5
Surface area	1 : 10	1 : 4	1 : 3
H_2 evolution	1 : 5	1 : 7	1 : 1.7

Simplistically, in the absence of any photonic effects or differences in the micro- and surface structure of the bulk and macroporous materials, the surface area normalised H_2 evolution should be similar. However, it is unknown if the surface chemistry of the bulk and macroporous materials is the same and XPS would be useful to examine the surface oxidation composition and Ta oxidation states.

For H_2 production, active sites trap the migrated e^- on the surface of the photocatalyst. Since not all trapping sites exist on the surface, the number of active sites is not directly proportional to an increase in surface area and is dependent on the crystal quality. For the macroporous materials which are prepared at lower temperature, the number of bulk crystal defects may be greater resulting in lower activity.

Light absorption by the photocatalyst is also clearly important and for bulk materials, the active areas are mostly on the surface of the photocatalyst particles. In contrast, for the macroporous materials, a high proportion of the active surface area is within the inner part of the photocatalyst, so the light cannot directly penetrate to the inner surface area because of light scattering or the internal 'shadow effect'. Hence, for bigger particles of the macroporous photocatalyst, a higher portion of active surface area would be located at the inner of the photocatalyst, so relatively less area would be directly irradiated potentially causing a lower photocatalytic activity. The effect of external scattering was estimated by preparing a macroporous solid of similar particle dimensions and pore size that does not absorb such as SiO_2, and measuring the power loss of the transmitted light. Figure 2.15 shows the absorbance of SiO_2 and Table 2.10 shows the light absorbed-scattered with and without a cut off filter (> 400 nm).

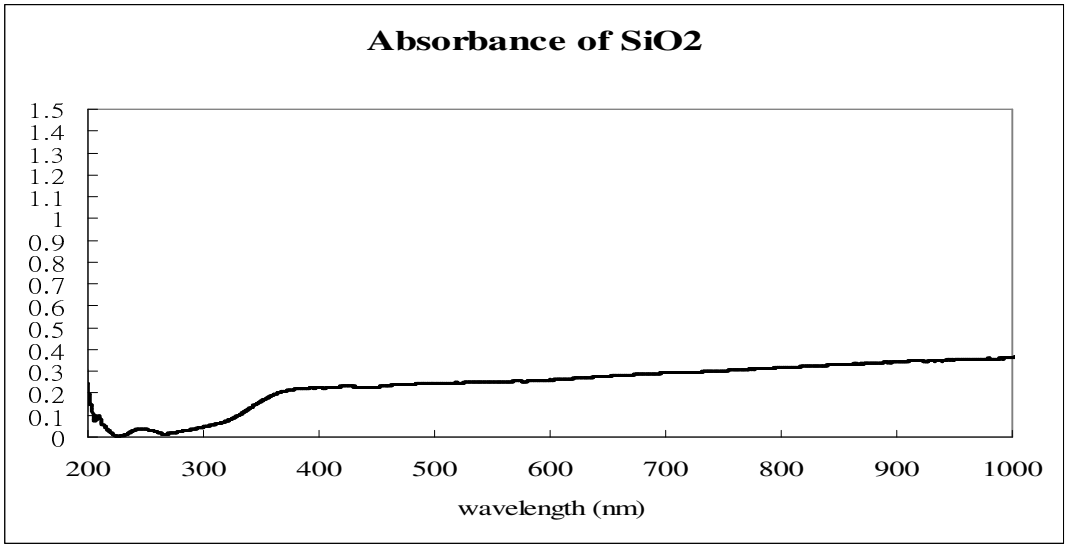

Figure 2.15. Absorbance of SiO_2.

Table 2.10. Light absorbed-scattered of SiO_2 and the normalized light absorption of bulk and macroporous Ta_2O_5, TaON and Ta_3N_5.

	Light absorbed-scattered (mW/cm^2)[b]	
SiO_2[a]	UV + Vis	Vis
Light absorbed-scattered (mW/cm^2)	134	104

Photocatalysts	Light absorbed by photocatalyst (mW/cm^2)[b]	
10mg Bulk Ta_2O_5	329	---
10mg Macroporous Ta_2O_5	316	---
40mg Bulk TaON	300	111
40mg Macroporous TaON	351	158
40mg Bulk Ta_3N_5	472	261
40mg Macroporous Ta_3N_5	409	189

[a] 2mg SiO_2 in 110 mL of 100:10 water:methanol. [b] 300W Xe lamp measured with a power meter.

The light absorbed-scattered value of SiO_2 in both UV + Vis and Vis are similar, indicating that the majority of photons are being scattered in both cases. The lamp output of ca 1500 $mWcm^{-2}$ indicates that the light absorbed-scattered by SiO_2 is about 9% and 7% in UV+Vis and Vis range, respectively.

Conversely, internal scattering could lead to an increase in activity as the effective path length of the photon would be increased, thus increasing the probability of absorption. Measurement of the irradiance loss on passing through the reaction

vessel containing macroporous or bulk material respectively, did not show a significant difference which implies that the internal surface of the macroporous materials is being illuminated.

The band gap locations of Ta_2O_5, TaON and Ta_3N_5 are shown in Fig. 2.16. The conduction band (C.B.) of tantalum compounds are constructed mainly from the 5d Ta orbital, and the valence band (V.B.) of Ta_2O_5 from O 2p, TaON from hybrid O and N 2p, and Ta_3N_5 from N 2p orbital, respectively.

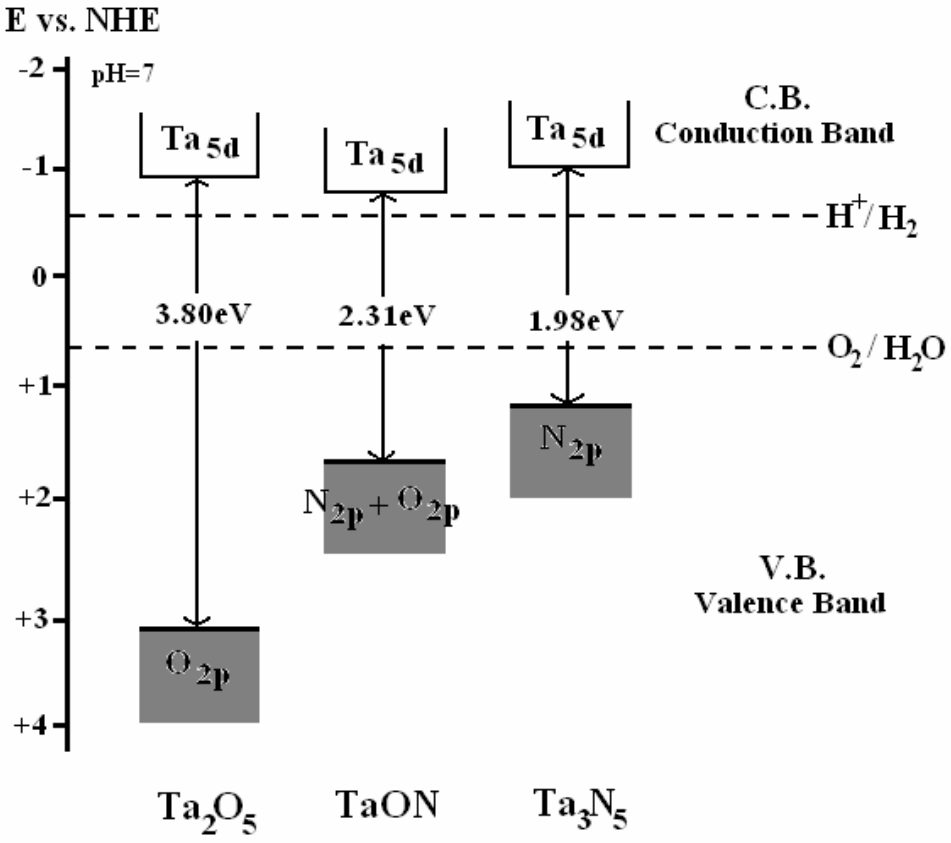

Fig. 2.16 Band structure of Ta_2O_5, TaON and Ta_3N_5.

Since the reduction reaction to produce H_2 occurrs at the conduction band, according to the location of the conduction band of Ta_2O_5, TaON and Ta_3N_5, the H_2 evolution of those tantalum compounds would be similar. However, the experimental results show that the H_2 evolution of TaON and Ta_3N_5 are about an order of magnitude lower than Ta_2O_5. Clearly, without Pt cocatalyst the surface catalysis for proton reduction will be different. Using Pt cocatalyst, where the reduction step should be identical these observed differences could be due to the

defect formation during the nitridation process that produce a Schottky barrier to hinder the e^- diffusion to the surface of Ta_3N_5.[63] Similar defects may also occur on TaON that cause its low photocatalytic activity. Besides, Frenkel defect could also be one of the defect interference for the low photocatalytic activity of both TaON and Ta_3N_5 during the displacement of O^{2-} by N^{3-} that the ion is lodged in the interstitial site of the lattice. As explained, crystallinity is a major factor to influence the defect formation, so the low H_2 evolution of TaON and Ta_3N_5 may be caused by the low crystallinity of the structures.

Furthermore, from an energetic perspective, the lower the band gap energy, the easier the excited electron can relax back to the valence band and recombine with the hole. TaON and Ta_3N_5 have much smaller band gaps compared to Ta_2O_5, and the lifetime of the excited electron is relatively lower, which would lead to a lower activity.

Chapter 3

There are many published studies describing photocatalytic degradation of organic molecules or water splitting experiments using a range of light sources, catalyst concentrations, cell geometries and filtering methods. Unfortunately many reports do not provide sufficient experimental detail to interpret results rigorously and allow comparison of activities from different materials.[44, 64] As part of this project we wished to calibrate the photocatalytic cell and understand the effect of various experimental parameters to help in the interpretation of future work. Fig 3.1 shows the experimental apparatus used in this thesis. The cell is cylindrical and the outer curved walls covered with reflective foil. The apparatus is designed to allow measurement of any light transmitted through the length of the cell, because ultimately we would like to obtain either absolute or apparent quantum efficiencies which can be problematic measurements. Experiments were designed so that total attenuation of the light does not occur so that all the photocatalyst should be under illumination irrespective of its location in the cell.

3.1. Absorption Measurements

Initially a series of measurements were performed to examine the attenuation of the light passing through the cell. Fig. 3.1a shows the solid state UV-Vis absorption spectrum for P25 and Fig 1b the absorption spectrum of water.

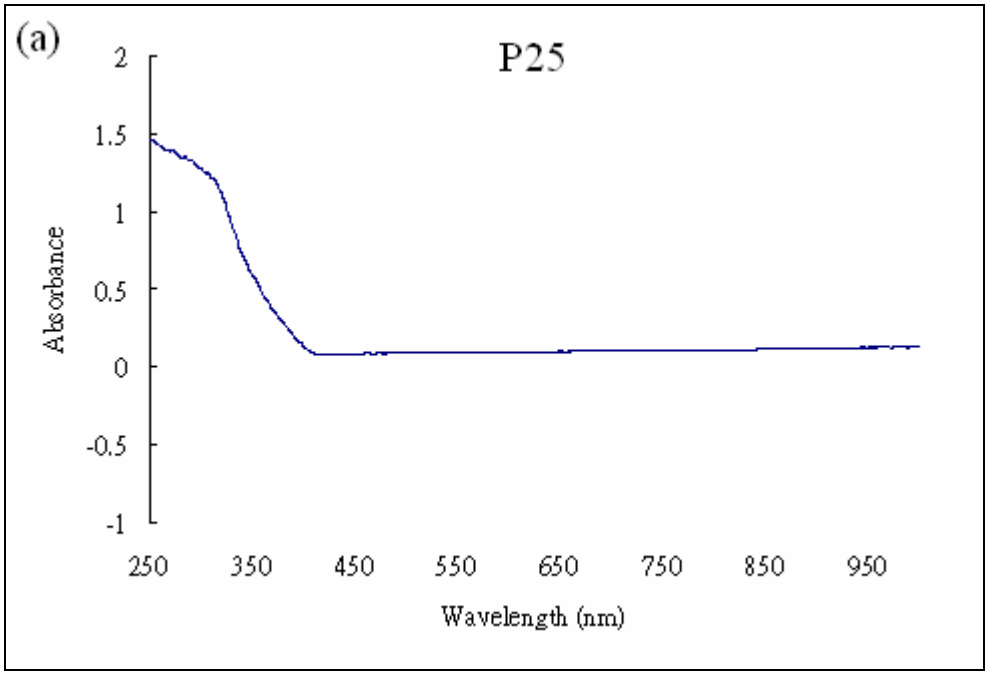

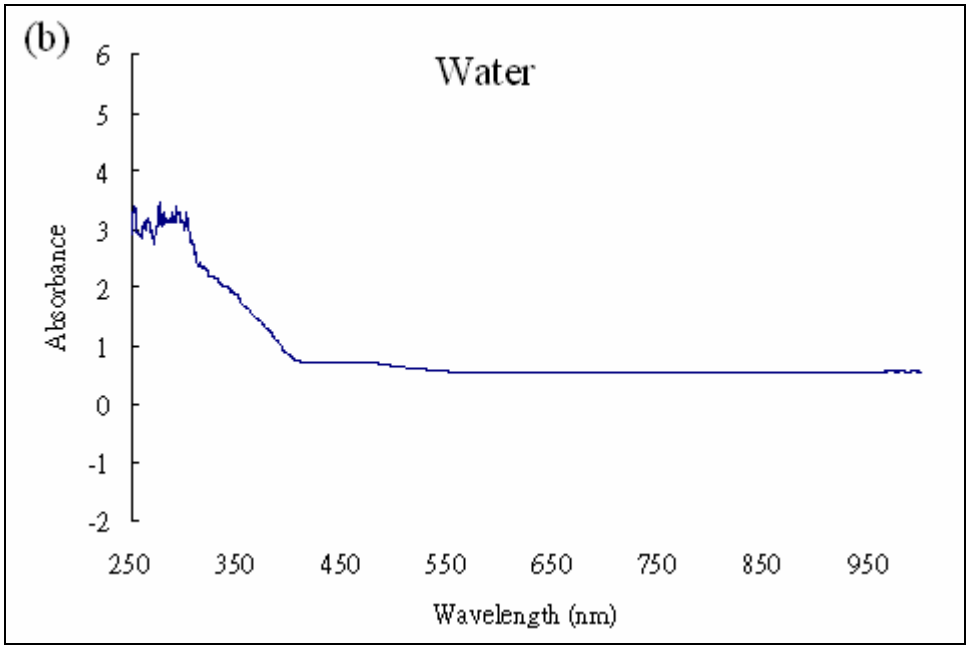

Fig. 3.1 shows the absorbance of (a) P25 and (b) water.

Fig. 3.2 shows the light passing through the cell as a function of increasing concentration of P25 and it can be seen that as expected there is a decrease due to absorption and scattering. Using a power meter, the lamp output is about 1500 mW/cm^2, and the light being absorbed by the blank system without photocatalyst (catalytic cell + 100ml water + 10ml MeOH) is about 60 %. The maximum percentage of light being absorbed by P25 in the range of 2.5mg to 150mg is about 37%.

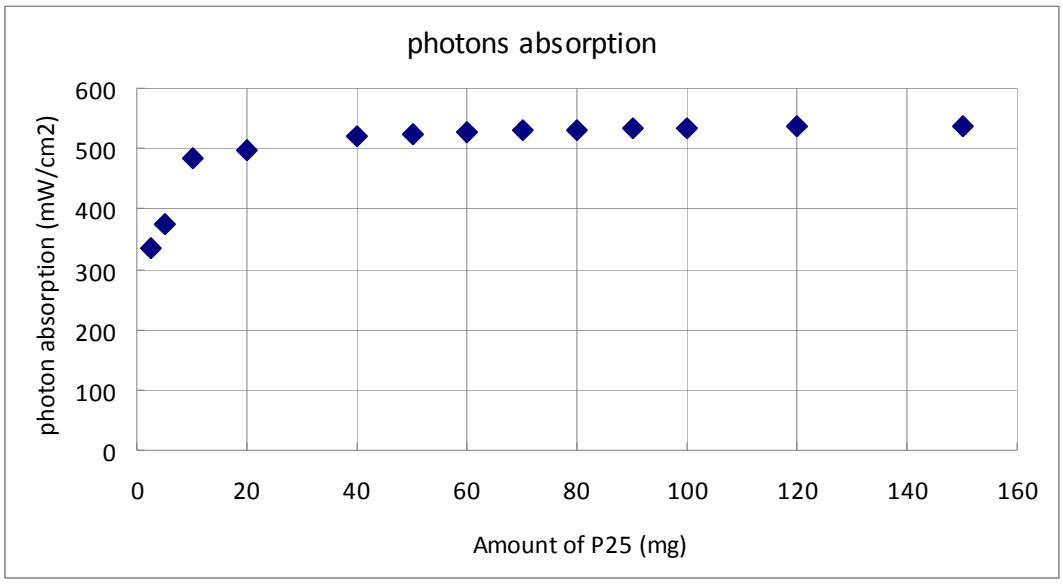

Fig. 3.2 pure P25 light absorption in 100ml H_2O + 10ml MeOH system.

Fig. 3.3 shows the background measurement of light absorption of different water volume added into the catalytic cell. The more the water volume, the more light the system absorbs.

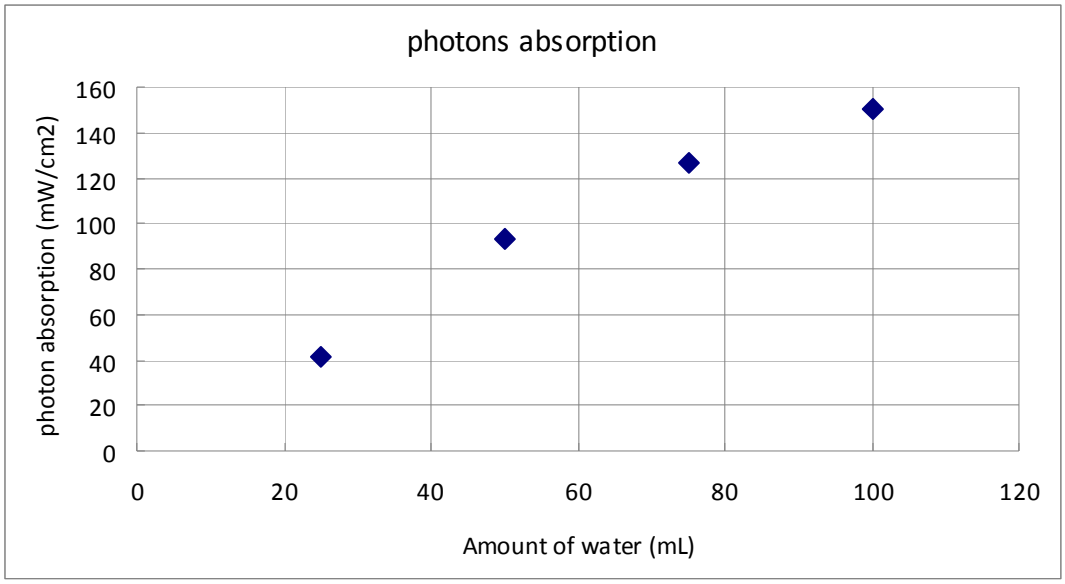

Fig. 3.3 light absorption of water (25ml, 50ml, 75ml and 100ml).

Fig. 3.4 shows the photon absorption of P25 in 50ml or 100ml H_2O, respectively. It shows that the light absorption is more or less the same for both systems. Comparing figures 3.2-3.4 it can be seen that the photocatalyst dominates absorption rather than water, indicating that the water does not have significant effect for the light absorption.

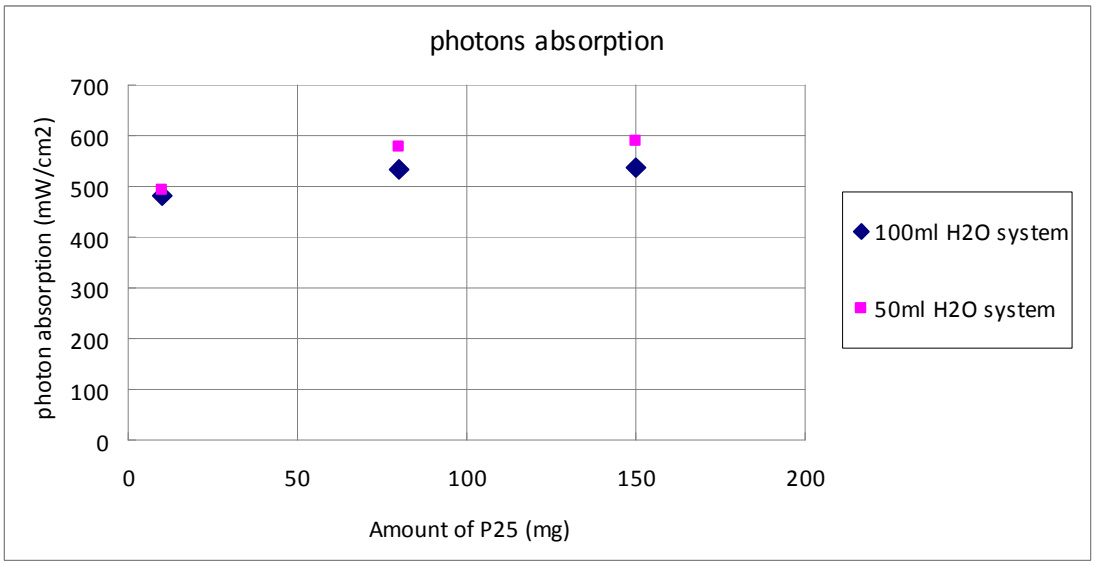

Fig. 3.4 Comparison of photon absorption of P25 in 50 and 100 ml H_2O.

Fig. 3.5 shows H_2 evolution as a function of P25 mass for 5 hours in the range 2.5mg to 150mg. It shows that the amount of H_2 generated is increasing until 80mg, then decreases, although the data is somewhat scattered. The implication is that there are an optimum number of photons per TiO_2 particle or per m^2 of illuminated surface to maximize the H_2 evolution.

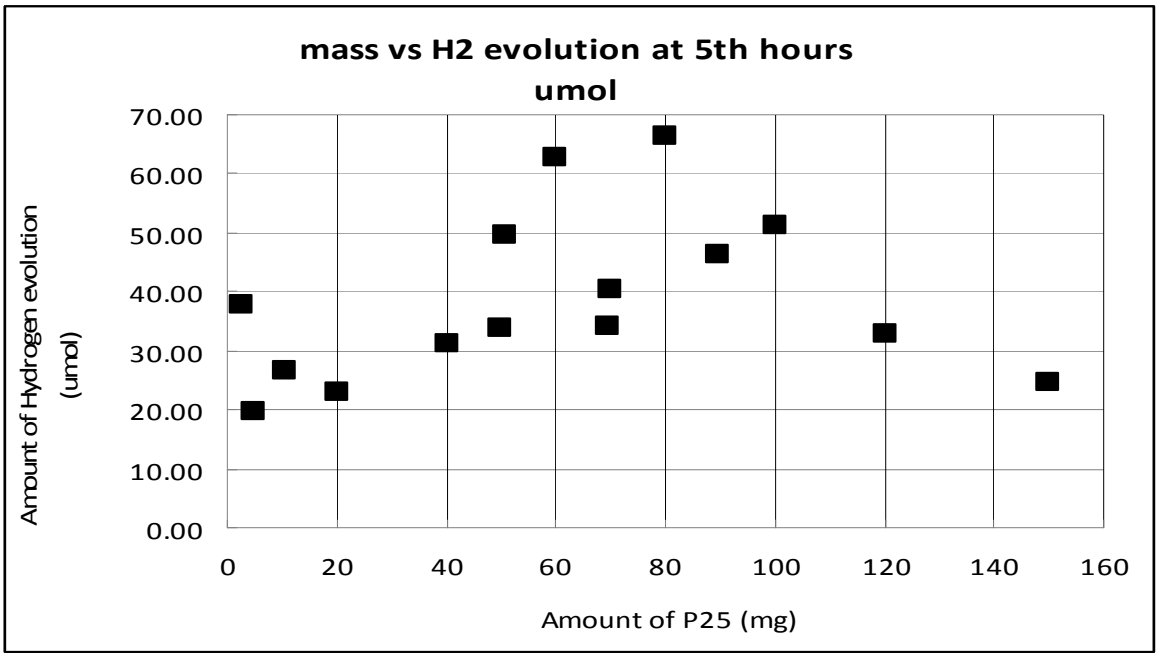

Fig. 3.5 A series amount of P25 vs actual H_2 evolution photocatalytic activity

Fig. 3.6 shows the comparison using 50 and 100 ml H_2O with three masses of P25. The result shows that for each mass there is no significant concentration effect, although again 80 mg shows the greatest evolution indicating an optimum photon-particle parameter. Further work would be required to determine if the parameter to be optimized is surface area or volume.

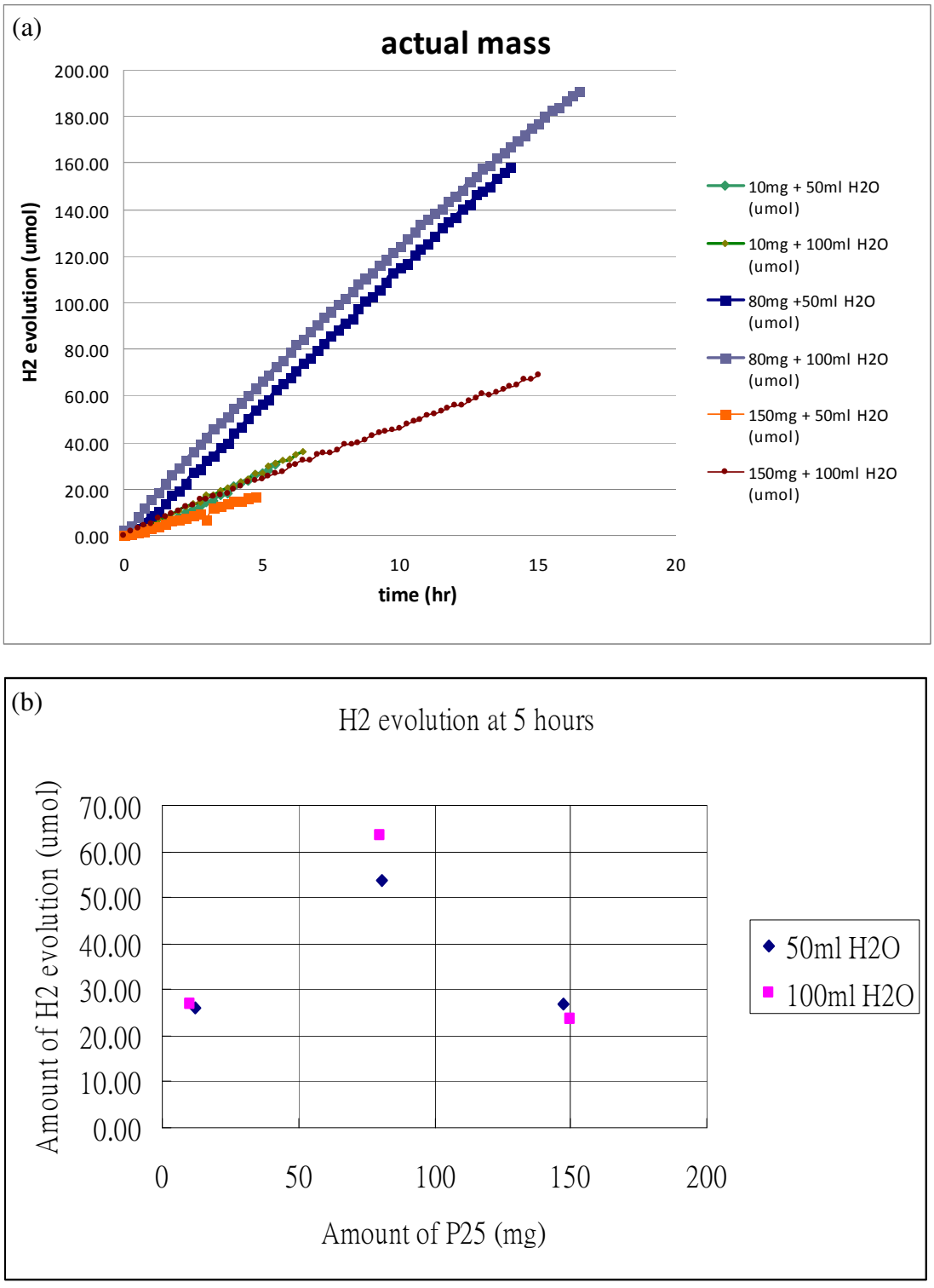

Fig. 3.6 Comparison of 50ml and 100ml H_2O added to the catalytic cell with 10ml MeOH at 40 ^oC. a) The amount of H_2 production of the P25 catalytic system; b) amount of H_2 evolution after 5 hours photolysis of P25.

By comparing the H_2 evolution activity of different amount of P25 under the same condition in Fig. 3.5, in general, the amount of H_2 produced keeps increasing up to 80mg. It is because the amount of P25 is proportional to photon absorption. However, after 80mg, the H_2 evolution is decreasing, presumably because of light attenuation across the system (Fig 3.7) and potentially an optimum photon-particle ratio. Since the volume of the cell is fixed, the more photocatalyst is used, the higher the concentration of photocatalyst in the system, so less light can penetrate to the bottom of the system but is absorbed by the upper layer of the photocatalyst. Thus, the photon absorption of the bottom part of the photocatalyst would be blocked. However, if this was the case using 50 and 100 ml of water should show for the 80 mg case an evolution similar to 150 mg in 100 mL of water. Indeed, there is a drop (Fig 3.6b) but considering the inherent error in these measurements as indicated by the scatter in Fig 3.5 and 3.6a it is difficult to judge if the drop is significant. These experiments need to be repeated many times to gain some statistical averaging.

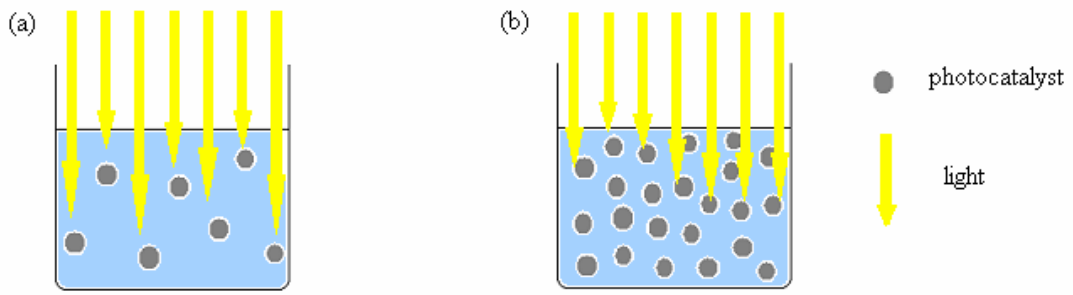

Fig. 3.7 Schematic illustration of the influence of light attenuation, which can prevent some of the phootcatalyst from being illuminated. a) low concentration of photocatalyst in system; b) high concentration of photocatalyst in the system.

An additional factor could be the requirement for an optimum photon-particle/surface area ratio due to the number of electrons generated and their lifetime. H_2 evolution is formally a two electron-two proton reaction, which is probably not concerted but two electrons should be generated approximately at adjacent sites and similar time to produce one H_2 and minimize non-productive reactions (Fig 3.8). Therefore the amount of hydrogen would be expected to increase where more photons are absorbed per particle or per m^2 generating more electrons. However, it is possible that if the illumination is very intense a high concentration of electrons and holes would result in recombination and a decrease in H_2 evolution, but this is not likely here as intensities >> ca. 1 Wcm^{-2} (our lamp output) are required.

For a constant irradiance and assuming a constant particle size, for the case where the light is in excess, an increase in photocatalyst concentration would result in an increase in the amount of H_2 evolved, but the rate per particle (or per m^2) would be the same. As the concentration of photocatalyst increases, light attenuation becomes important and when the light is limited the number of photons absorbed per particle would be reduced. When no light passes through the cell, the maximum number of photons is being absorbed and the hydrogen evolution may be expected to plateau. However, Fig 3.4 and 3.6 show that a decrease is observed indicating a mimimum number of photon absorption events are required per particle (or per m^2) per second, which would be expected for a biphotonic or two electron process.

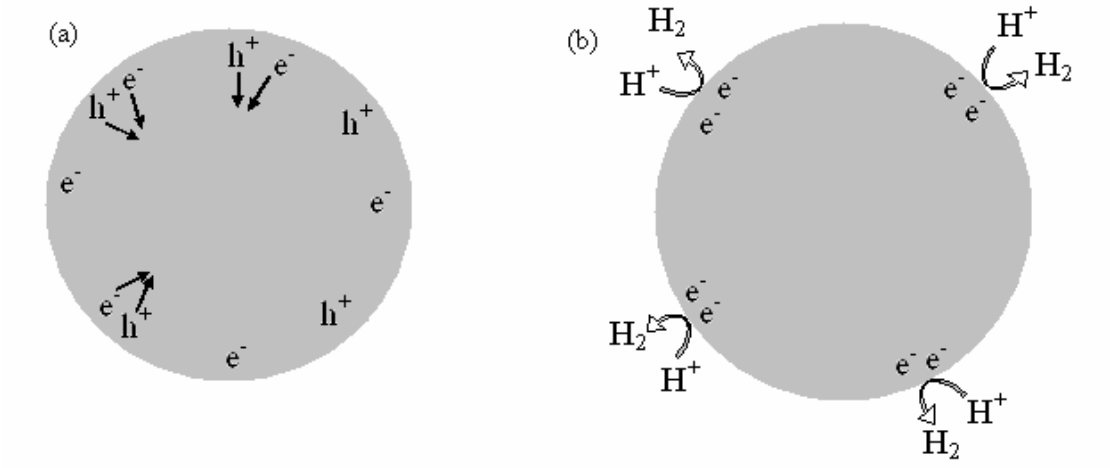

Fig.3.8 Schematic illustration of a) occurrence of e^-/h^+ recombination; b) H_2 formation on the surface of photocatalyst by two electrons.

Overall there will probably be an optimum photon-particle (surface area) ratio to maximize electron-hole concentration and H_2 evolution.

Unfortunately the heterogeneous nature of these reactions means that there are other factors that may be significant such as inhomogeneous dispersion of P25 in the system, which would influence the photon absorption; as well as the aggregation of P25 during photocatalytic reaction that will affect the surface area. Further controlled experiments should be done and if possible kinetic analysis. For instance, the influence of particle size, would help to define the importance of surface area, and immobilisation of a monolayer of particles could be used to study the effect of different light intensities and determine the optimum photon concentration.

An important point is that comparison of the H_2 evolution of different materials by calculating the activity per gram (μmol/g) is not accurate, since different amount of photocatalyst for the same materials would give various amounts of H_2 evolution because of the effects mentioned above. Also, different photocatalytic systems would give various results as well, because their light absorption and electron-hole lifetimes would be different. Therefore, ideally the same conditions and cell configuration should be used for the photocatalytic testing of solid state materials, for the purpose of comparison, if this is not possible then a comprehensive description of the experimental method.

Experimental
Chapter 4

4.1 Materials and reagents

Styrene (99%), potassium persulfate, sodium carbonate, sodium chloride, ethanol, methanol and 70% nitric acid were supplied by Fisher Scientific. Tantalum (V) ethoxide (99%), citric acid, 99.9% metal basis hexachloroplatinic acid, 99% silver chloride and tantalum(V) oxide were supplied by Sigma Aldrich. P25 was supplied by Degussa. Ammonia gas and 99.995% hydrogen gas were supplied by BOC.

4.2 Characterization methods

Powder XRD measurement

Macroporous tantalum photocatalysts were analyzed on a Bruker-AXS D8 Advance instrument fitted with a Lynxeye detector. Data was acquired using Cu Kα radiation between 5 and 75° 2θ, with a step size of 0.01 and time per step of 0.2 s.

UV-Vis spectroscpy (Reflectance and Absorbance)

Reflectance and absorbance spectrum of materials were measured by Ocean Optic Inc. HR2000+ High Resolution Spectrometer, with scan average of 10, boxcar width of 5 and light source from Helium and Deuterium by Photonic Solutions Ltd. DH-2000-BAL.

Brunauer-Emmett-Teller (BET) surface area measurement

Surface areas of materials were measured by Micromeritics Tristar 3000 from the nitrogen adsorption isotherm, at the temperature of liquid nitrogen (-195 ℃) and samples were pre-dried under nitrogen at 150 ℃ for 6 hours

Scanning Electron Microscopy (SEM)

SEM images were obtained from FEI Sirion scanning electron microscopy, with EDAX Phoenix EDS x-ray spectrometer. Tiny amount of samples were broken into powder and put on the carbon tape with an aluminum stand and Carbon-coating with 10nm thickness was used for all samples.

Transmission Electron Microscopy (TEM)

TEM images were obtained from JEOL JEM-2010 transmission electron microscope, with 200kV ultrahigh resolution analytical electron microscope. Small amount of samples were dispersed in acetone and grounded by mortar and pestle, following by adding 4-5 drops of dispersed solution on the carbon grid and dried in air for a minute.

Photocatalysis equipment

Illumination was performed using a 300W Xe lamp from LOT-Oriel fitted with a 15cm IR filter and a wideband $AlMgF_2$ coated mirror. Gas analysis was performed using a GC instrument from Shimadzu Corporation with an automated sample loop of 50 μL. Gases were separated on a 25 cm long column packed with 5 Å molecular sieves and detection was performed using a thermal conductivity detector (TCD). The gas samples were analyzed using the following conditions; 20 mL/min flow rate of Ar gas, 90℃ column temperature and 120℃ detector temperature. Under these conditions the retention time of H_2 is 1.5 min, O_2 2.5 min and N_2 3 min.

4.3 Materials synthesis

4.3.1 Polystyrene (PS) template

An emulsifier-free emulsion polymerization method was used based on a literature report.[53] To a three-necked 3L round-bottomed flask containing deionised water (1700 mL) heated to 70°C under N_2 was added styrene (200 mL, 1.745 mol) which had been prewashed with an aqueous NaOH solution (10 mL, 0.1 M). To this mixture was added potassium persulfate initiator ($K_2S_2O_8$) (1.989 g, 7.329 mmol) dissolved in 100 mL of deionised water all at once and the mixture was kept at 70°C and stirred at 360 rpm using a Teflon overhead stirrer for 28 h. After cooling the colloidal solution was filtered through glass wool to remove larger polymer fragments and the milky filtrate stored for future use. To obtain the template, the colloidal solution was centrifuged at 4000 rpm for 3 h and dried in an oven at 55°C for 12 h, then broken into a powder form using a spatula. A sphere diameter of 500±20 nm was estimated by scanning electron microscopy (SEM).

4.3.2 Macroporous tantalum(V) oxide (Ta_2O_5)

Dried ethanol (10ml) was added to a powdered sample of the PS template (2.5g) under argon in a Schlenk flask, and the volatiles were removed from the mixture

at 55 ^{o}C under vacuum for 30 min. A dried ethanol solution (5 mL) of tantalum(V) ethoxide (2 g, 4.92 mmol) was added to the dried PS template and left to stand for 30 min. The volatiles were then removed at 55 ^{o}C under vacuum for an hour. The tantatlum/PS composite was then heated in air at 700 ^{o}C for 8 hr in a muffle furnace. The pore size of the macroporous Ta_2O_5 is 370±10nm and the wall thickness 70±5nm, by SEM.

4.3.3 Macroporous tantalum(V) oxynitrde (TaON)

Macroporous tantalum(V) oxynitride was prepared from macroporous Ta_2O_5, and required very careful control of the synthetic conditions to minimize impurity phases of Ta_2O_5 or Ta_3N_5. Ta_2O_5 powder (0.20 g, 0.452 mmol) was heated in a tube furnace under flowing wet NH_3 (20 mL/min) where NH_3 gas (at a flow rate of 20 ml/min) was passed through a round-bottomed flask containing deionized water (30 ℃; 50mL) at 825 ^{o}C for 6 hr with 1 ^{o}C/min heating rate. The reaction was then cooled to 25 ^{o}C to give the product as a yellowish powder. The pore size of macroporous TaON is 380±10nm and the wall thickness is 60±5nm, by SEM.

4.3.4 Macroporous tantalum(V) nitride (Ta_3N_5)

Macroporous tantalum(V) nitride was prepared from macroporous Ta_2O_5. Ta_2O_5 powder (0.2 g, 0.452 mmol) was heated in a tube furnace under flowing NH_3 (20 mL/min) at 800 ^{o}C for 2 hr with 1 ^{o}C/min heating rate. The product is a bright orange colour. The pore size of macroporous Ta_3N_5 is 400±10nm and the wall thickness is 60±10nm, by SEM.

4.3.5 Bulk tantalum(V) oxynitride(TaON)

Bulk tantalum(V) oxynitride was synthesized from bulk Ta_2O_5 (Aldrich)[65-66]. Ta_2O_5 powder (0.5 g, 1.13 mmol) was heated in a tube furnace under flowing wet NH_3 (20ml/min) where NH_3 gas was passed through a round-bottomed flask contained deionized water (30℃; 50ml) at 825 ^{o}C for 15 hr with 5 ^{o}C/min heating rate. The reaction was then cooled to 25^{o}C to give the product as a dull yellow powder.

4.3.6 Bulk tantalum(V) nitride(Ta_3N_5)

Bulk tantalum(V) nitride was synthesized from bulk Ta_2O_5 (Aldrich)[56]. Ta_2O_5 powder (0.5 g, 1.13 mmol) was heated in a tube furnace under flowing NH_3 (20ml/min) at 800 ^{o}C for 15 hr with 5 ^{o}C/min heating rate. The product is a bright red colour.

4.3.7 Deposition of Pt co-catalyst

Method 1 H_2 reduction

To obtain 0.5wt% and 3wt% Pt deposited photocatalyst composites. An ethanol solution of $H_2PtCl_6.xH_2O$ (0.0145 mol L^{-1}) and photocatalyst were stirred for 30 min and the mixture was dried under vacuum for 30 min (on a Schlenk line), and in an oven at 55°C for 1 hr. The dried mixture was heated under hydrogen at 200°C with 1°C/min heating rate for 1 hr, to reduce the hexachloroplatinic acid ($H_2PtCl_6.6H_2O$) to Pt.

Method 2 Pt-citrate sol deposition

To obtain 0.5 wt% Pt deposited photocatalyst composites. Pt-citrate sol was prepared from H_2PtCl_6 (10 mg, 0.019 mmol), sodium citrate aqueous solution (10mL, 1 wt% sodium citrate) and deionized water (40 ml).[67] The mixture was refluxed for 4 hr and then cooled to room temperature to give a grey liquid. A portion of the resulting Pt-citrate sol (2.5 mL) was stirred with photocatalyst (0.1g) for 30 min, and then sodium chloride (0.28g, 4.79mmol) was added and the mixture was stirred for 6 hr. The mixture was filtered and dried in the oven at 55°C for 30min. The grey photocatalyst residue was washed with water and dried in the oven at 55°C for 30 min and repeated for 3 to 4 times. The solid was then dried for 12 hrs at 55°C, following by further reduction under H_2 gas at 200°C for 1 hour. Silver nitrate and nitric acid were used to test for removal of chloride from the photocatalyst-Pt composite.

4.4 Photocatalytic hydrogen evolution measurements

4.4.1 General procedure

A pyrex cell with a quartz window was connected to a closed Ar gas circulation system. Illumination of the macroporous photocatalyst was carried out in the presence of methanol as a sacrificial reagent. 100mL of water, 10mL of methanol and the photocatalyst were added to the cell and the reaction was processed at 600rmp. The whole system was evacuated by a pump and back-filled with Ar as a carrier gas. The reaction was maintained at a constant temperature of 40 °C using an oil bath and illuminated with a 300 W xenon lamp with an output of ca. 1 W/cm^2. A UV high band pass filter (λ> 400 nm) was used for measuring visible light activity. The evolved gases were analyzed by gas chromatography at 15 min intervals.

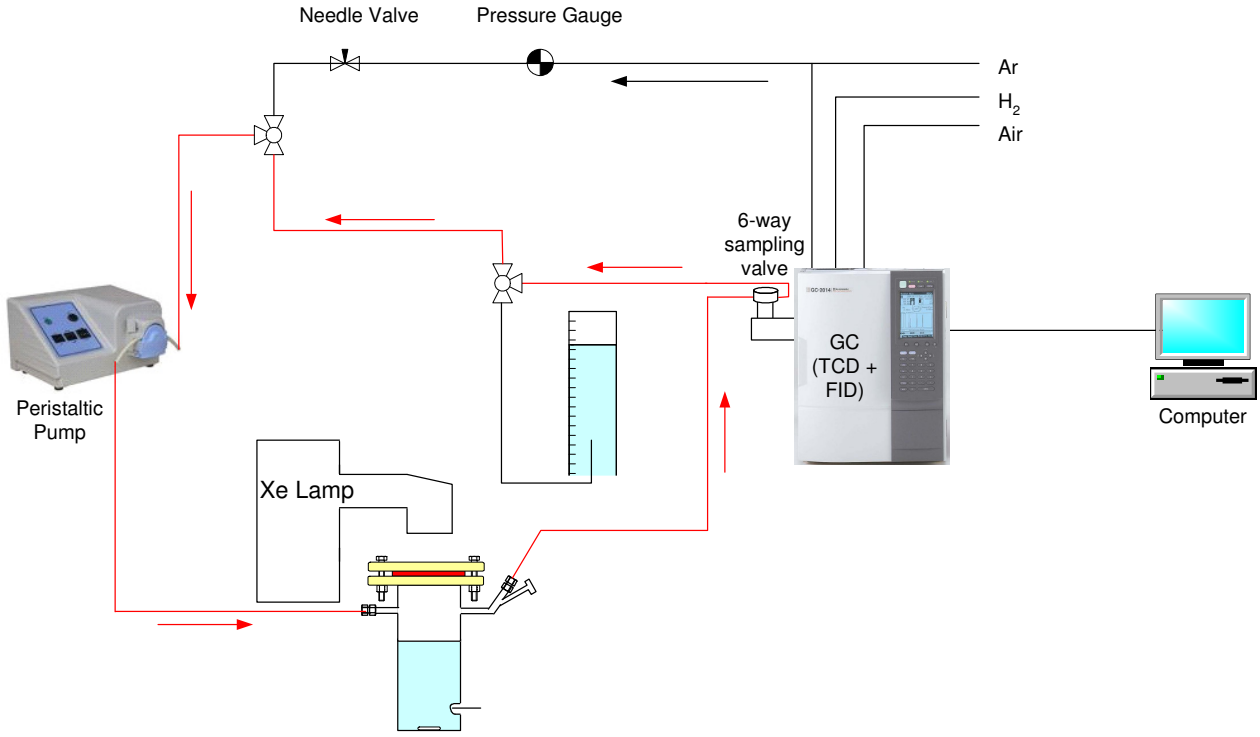

Fig. 4.1 experimental setup of Photocatalytic hydrogen evolution measurement

4.4.2 P25 calibration experiments

Using the apparatus shown in Fig 1iIllumination of the TiO_2 photocatalyst was carried out in the presence of methanol as a sacrificial reagent. Various volumes of water and methanol and masses of P25 were added to the cell as shown in Table 4.1. The whole system was evacuated by pump and back-filled with Ar as a carrier gas. The reaction was maintained at a constant temperature of 40 ^{o}C using an oil bath and illuminated with a 300 W xenon lamp with an output of ca. 1 W/cm^2. The evolved gases were analyzed by gas chromatography at 15 min intervals.

Water volume (mL)	Amount of P25 (mg)										
50	10	80	150								
100	2.5	5	10	40	50	60	70	80	90	100	150

Table 4.1: Different amount of P25 in certain volume of water

Conclusions and Future Work
Chapter 5

Bulk quantities of macroporous Ta_2O_5 can be prepared using a polystyrene templating technique and DRUVS shows photonic behaviour. Bulk nitridation can be achieved, to synthesize TaON and Ta_3N_5 respectively whilst retaining the macroprous structure and photonic properties. Electron microscopy and PXRD indicate that nitridation is associated with crystallite size reduction and wall densification. Comparison between TaON as a micron sized powder and macroporous material indicate that the lower temperatures required to synthesize macroporous TaON result in a mixture of γ- and β-TaON, whereas β-TaON is formed for the micron sized powder. Surface area measurements showed that the macroporous materials have a higher surface area per gram than the bulk powder, which is attributed to a smaller crystallite size. Given the relatively small difference in size between the crystallites/particles of powder and macroporous material for a particular composition, it is likely the walls are permeable to N_2, which is the gas used for the area measurements. The walls would therefore also be permeable to O_2 and H_2.

Future work should include further characterisation of the surface and wall structure of the macroporous materials and XPS would be particularly valuable. It is also critical that Pt dispersion be achieved and alternative loading methods from sols should be examined more thoroughly. To improve the quality of the photonic properties and the macroporous architecture, silica template can be used instead of PS to maintain the structure during nitridation process and remove the template by leaching, rather than high temperature calcination. Looking toward matching the optical and electronic band gaps to increase the electron-hole lifetime the pore-size should be tuned. Now that the wall filling factor and shrinkage on calcination can be estimated it is possible to calculate the required macropore size. It will also be critical to perform time resolved spectroscopy to determine if there is any evidence for electron-hole lifetime enhancement in the macroporous materials.

Macroporous and powder forms of Ta_2O_5, TaON and Ta_3N_5 were also tested for photocatalytic hydrogen production under Uv-Vis and visible light (> 400nm) illumination using a 300 W Xe source. In addition, hydrogen production was measured for Ta_2O_5 loaded with 0.5wt% Pt and TaON and Ta_3N_5 loaded with 3 wt% Pt, which is the optimum loading reported in the literature. It was found that

none of the materials exhibit significant visible light activity which is in contrast to the literature. All the non-Pt loaded macroporous materials exhibited higher activity than the powder analogues and when normalized to surface area macroporous-TaON showed a ca 40% enhancement, whereas Ta_2O_5 and Ta_3N_5 showed a ca 50% decrease in activity per m^2. As judged by Fig 4.2 large errors are likely with these numbers. Nevertheless the reduced activity was not sufficient to suggest reaction was not occurring in the inner volume of the macroporous particles. On addition of Pt to bulk powder materials and macroporous Ta_2O_5 an enhancement in H_2 evolution was observed. However, for macroporous TaON and Ta_3N_5 Pt addition resulted in a drop in activity. This is ascribed to problems dispersing the Pt nanoparticle precursors H_2PtCl_6 throughout the macroporous structure, resulting in larger aggregates at the surface that may block the pores or surface to light. However, further electron microscopy is required to confirm this, which was unfortunately prevented by time.

Future work should focus on achieving good nanoparticle dispersion, and proving this by Fast-Ion Bombardment (FIB) modified samples to examine the inner regions by electron microscopy. Determination of surface composition after photocatalytic reaction would also indicate if hydrolysis of the nitride surface is occurring. The photocatalytic reactions also need to be repeated to reduce the errors involved, although this does not explain why these materials are not active under visible light as reported in the literature. In order to understand important parameters in photocatalytic testing using our apparatus a short study on the effect of mass and concentration of photocatalyst showed that the concentration did not show significant influence on the photocatalytic activity, but the mass of photocatalyst did have a significant effect where for Degussa TiO_2 the optimum amount of photocatalyst used in our reaction system is 80mg. The results indicated that there is an optimum photon incidence per particle or per unit of surface area for solar hydrogen production from a water-methanol mixture.

Overall, there is enough in this study to suggest further work is warranted. If Pt homogeneous nanoparticle metal deposition can be achieved in macroporous materials then enhancement on Pt addition should be achieved. Furthermore reaction appears to be occurring inside the pores and therefore ultimately these materials could find use in monolithic type devices. A key question still to be answered is if photonic enhancement can be achieved but materials are now available to answer this question in the near future.

Appendices

Appendix A Photonic Stop band calculation data

Appendix B Scanning Electron Microscope (SEM) images

Appendix C Transmission Electron Microscope (TEM) images

Appendix D Brunauer-Emmett-Teller (BET) Surface Area

Appendix A

Photonic Stop band calculation data[68]

Materials	Refractive Index	Band Gap
Ta_2O_5	2.21	3.9
TaON	2.29	2.1
Ta_3N_5	3.80	2.4
Air	1.00	---
Water	1.33	---
Ethanol	1.36	---
Chloroform	1.45	---

$\lambda = 2d_{hkl}/m*[\varphi n_{wall} + (1-\varphi)n_{void}]$ (1)

$d_{hkl}=D(2)^{½}/(h^2+k^2+l^2)^{½}$ (2)

For example:

By calculating the stop band position of macroporous Ta_2O_5 with m=1, pore size 370nm, $n_{wall} = n_{Ta2O5} = 2.21$, $n_{void} = n_{air} = 1$, and materials in {111} phase, assuming the volume fraction is 10%.

$d_{hkl} = (370)(2)^{1/2}/(1^2 + 1^2 + 1^2)^{1/2}$

$= 302.10$ (3)

By substituting (3) into (1)

$\lambda = (2*302.10/1)*(0.1)[0.1*2.21 + (1-0.1)*1]$

$= 677.32nm$

Therefore, the stop band position of macroporous Ta_2O_5 in air is at about 677nm.

Appendix B

Scanning Electron Microscope (SEM) images at different magnifications (5000x, 10000x, 20000x 40000x, 80000x and 160000x) for Polystyrene (PS) template, PS and precursor composite, bulk and macroporous Ta_2O_5, TaON and Ta_3N_5.

Polystyrene packed template

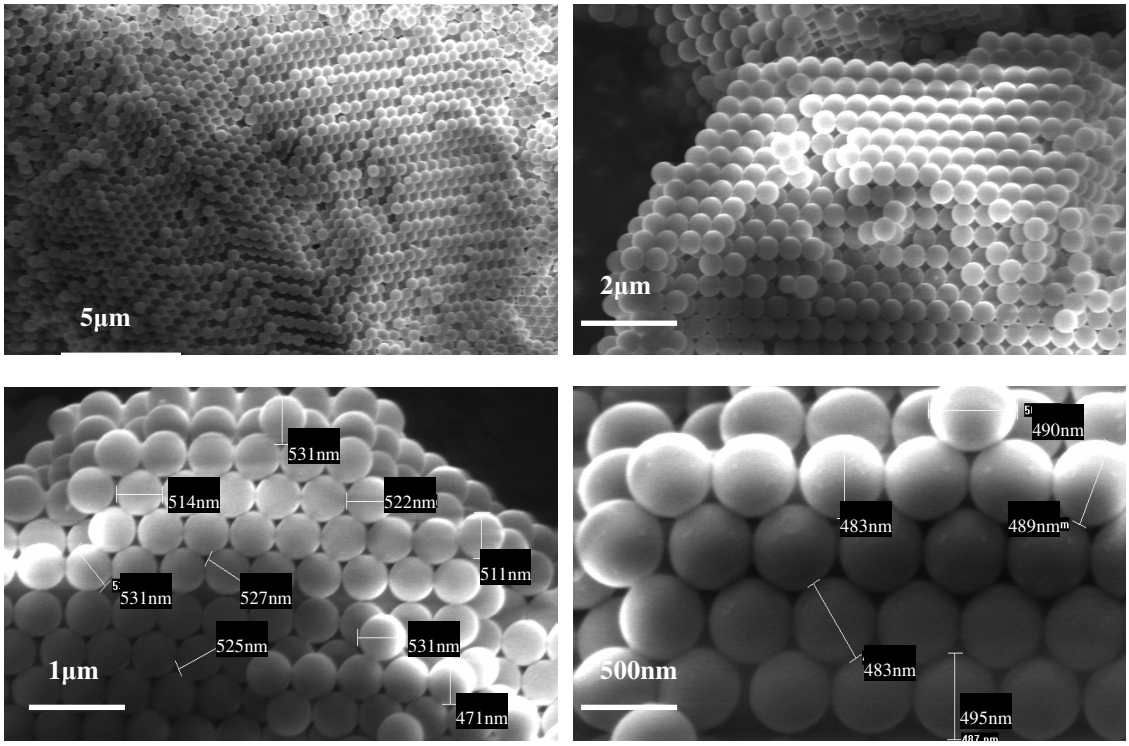

Polystyrene packed template with tantalum ethoxide precursor

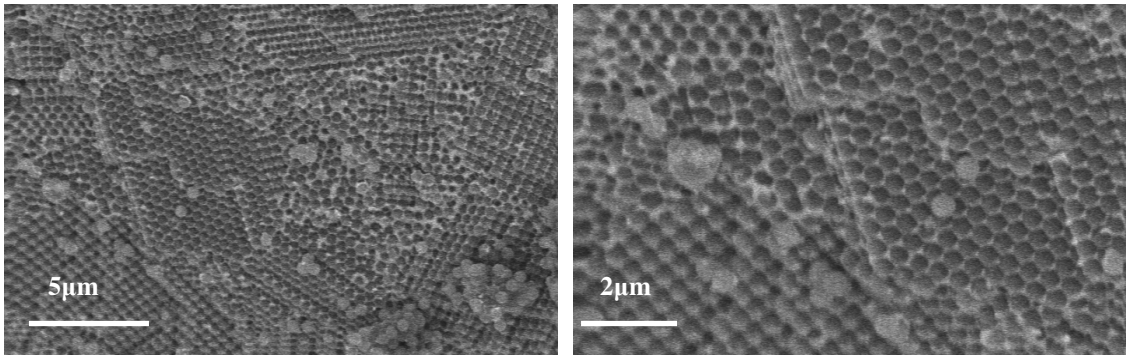

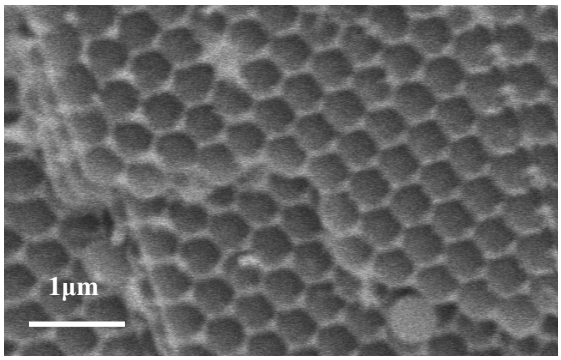

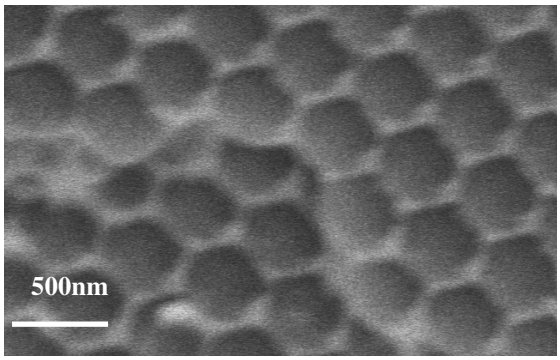

Bulk Ta_2O_5 and Macroporous Ta_2O_5

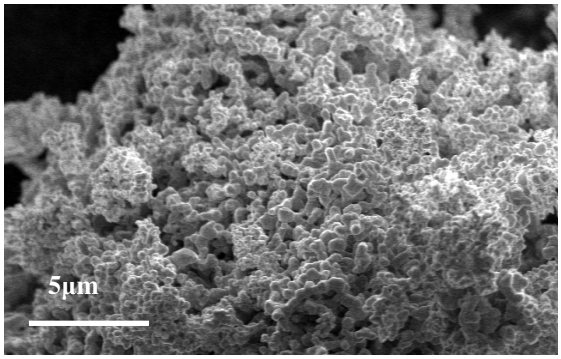

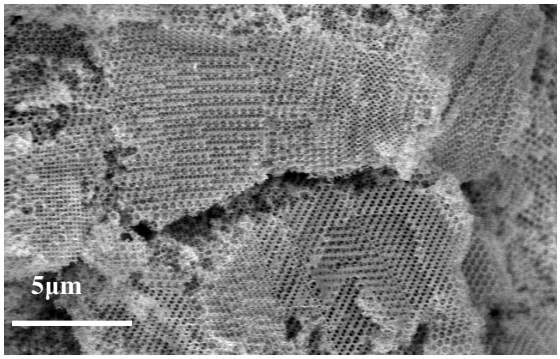

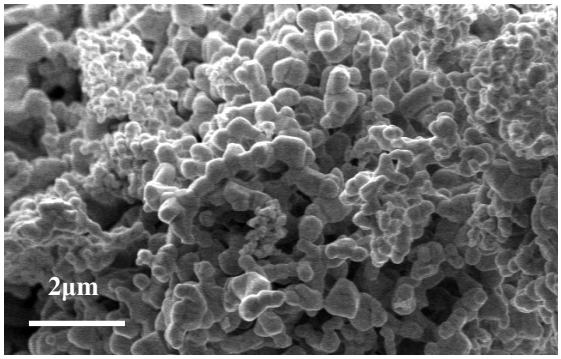

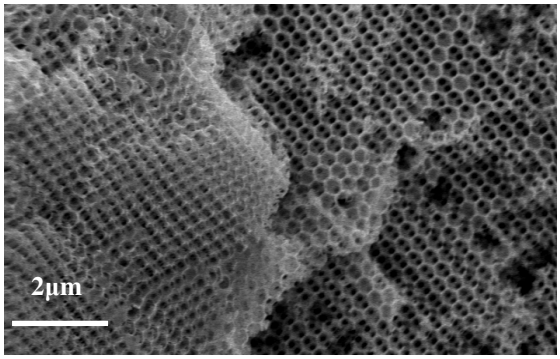

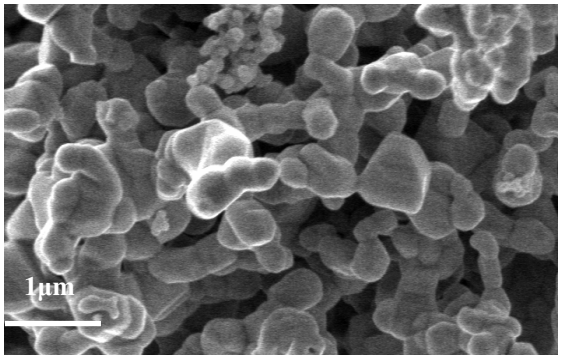

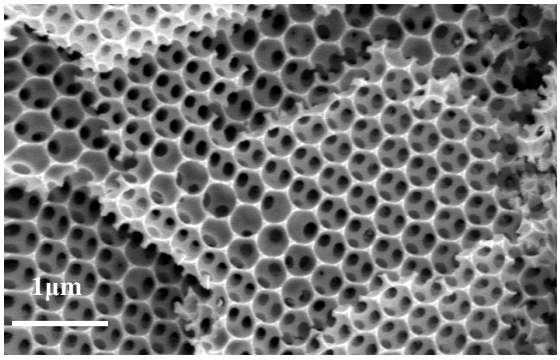

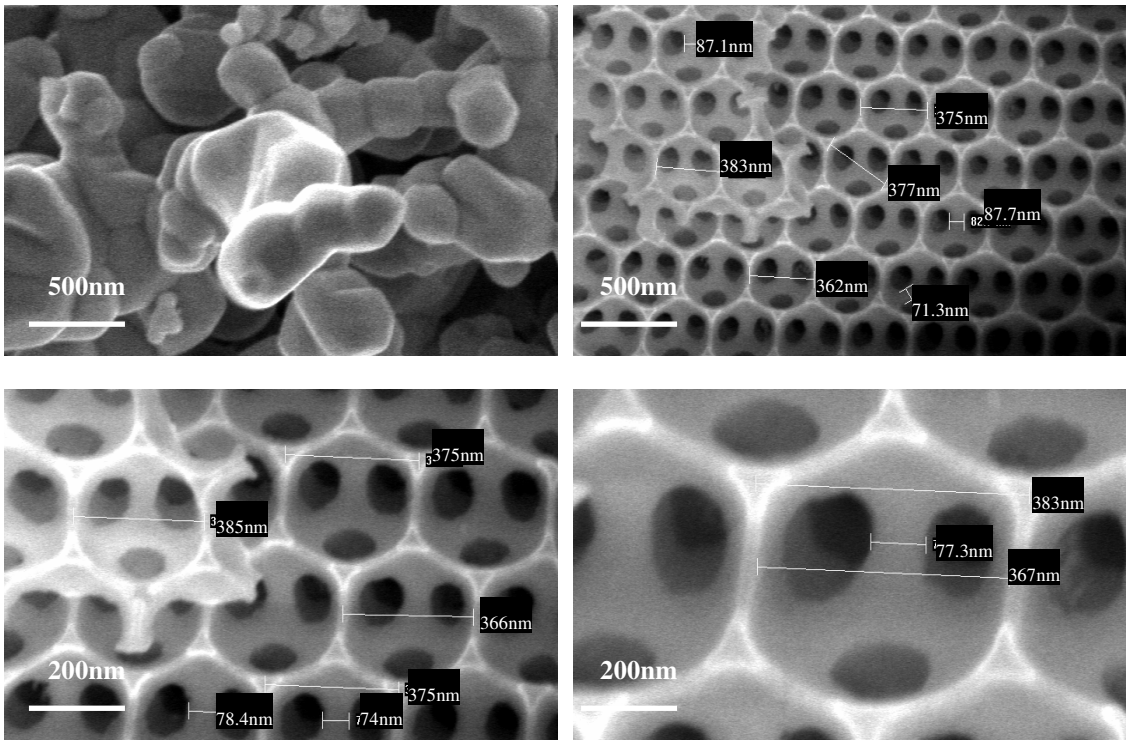

Bulk TaON and Macroporous TaON

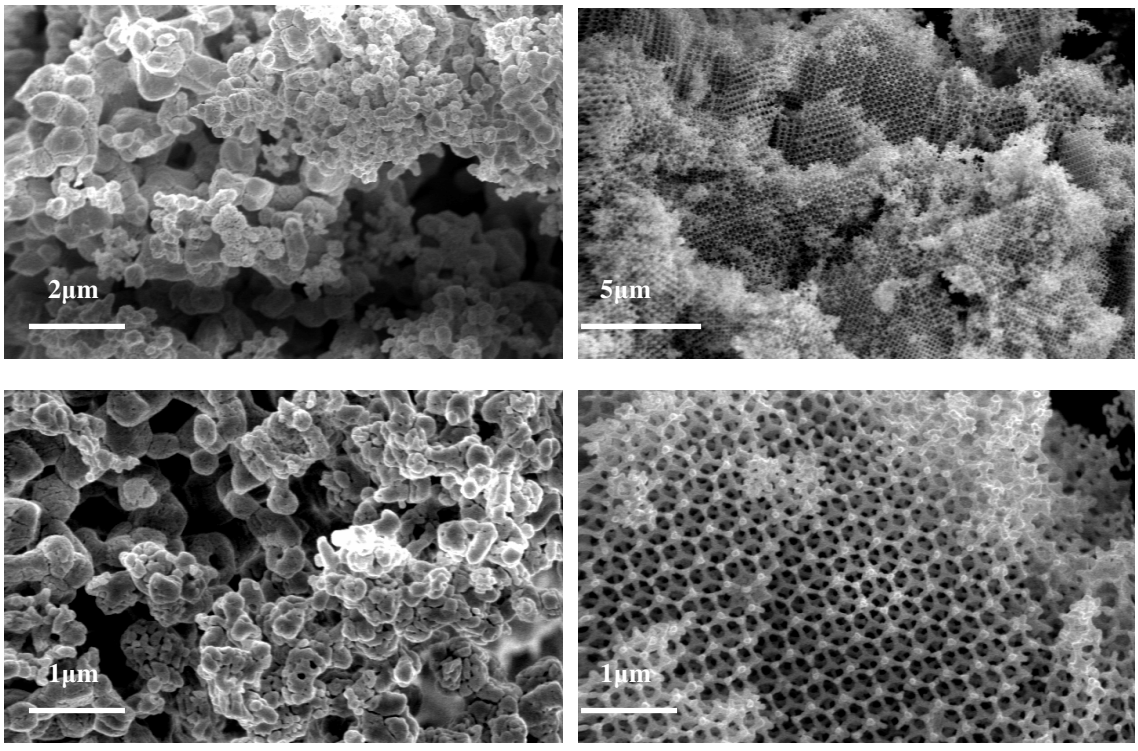

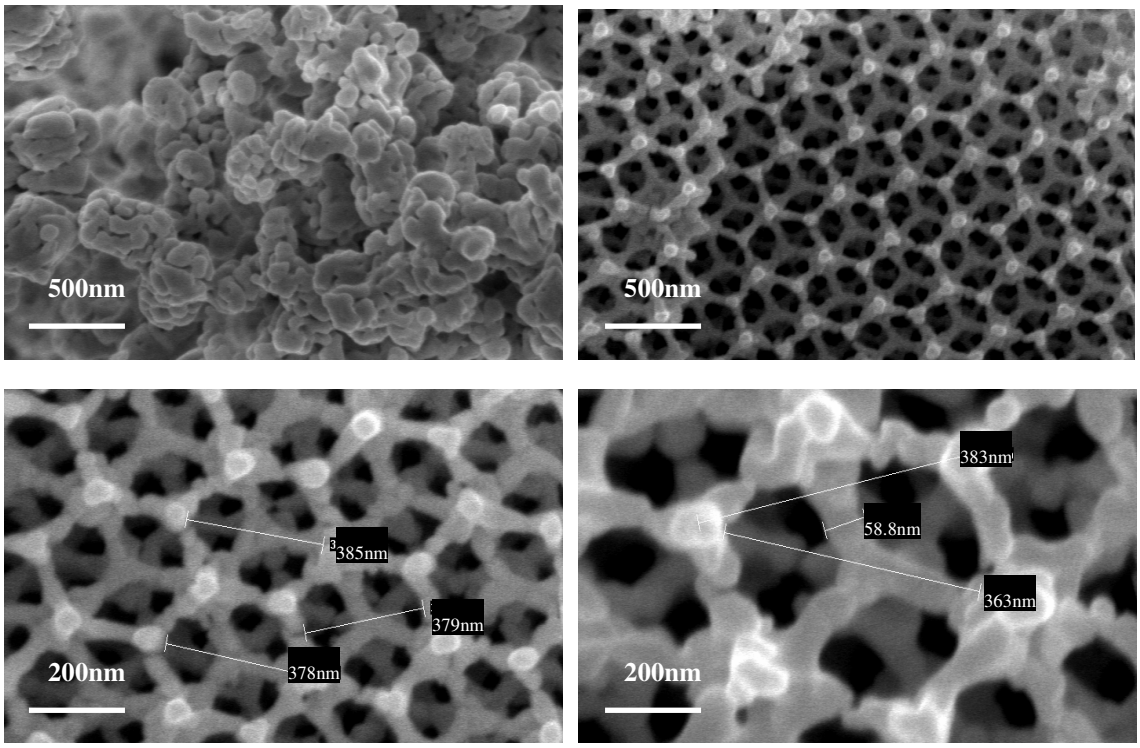

Bulk Ta_3N_5 and Macroporous Ta_3N_5

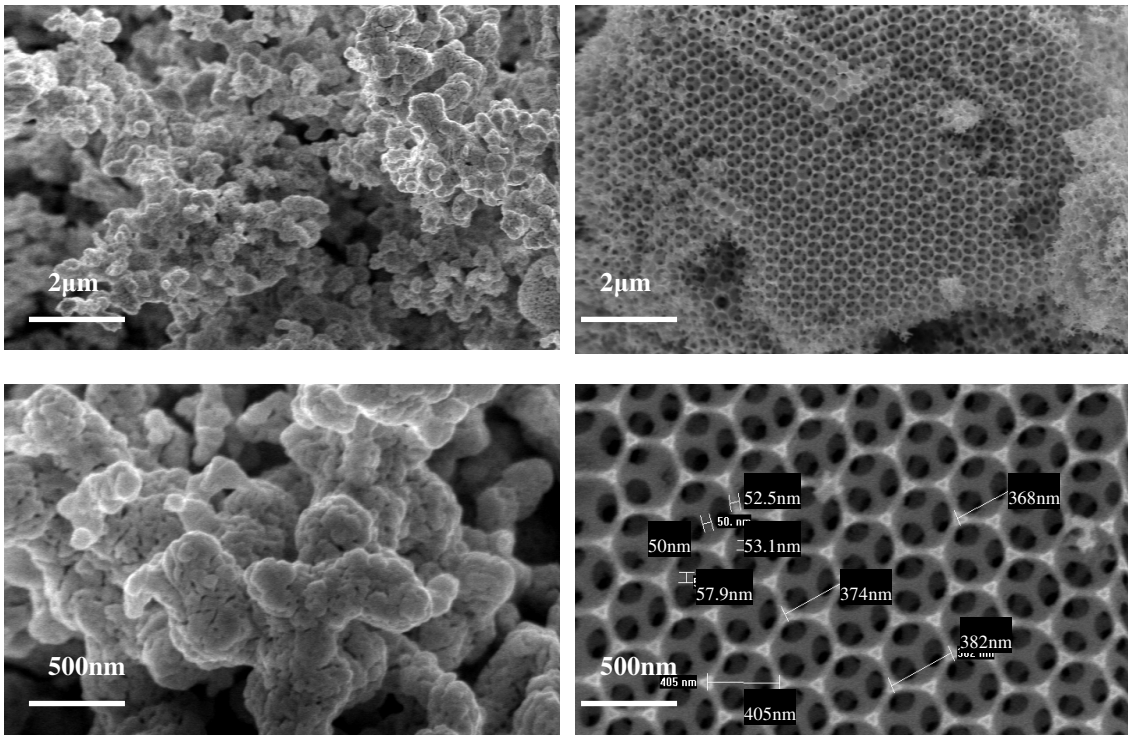

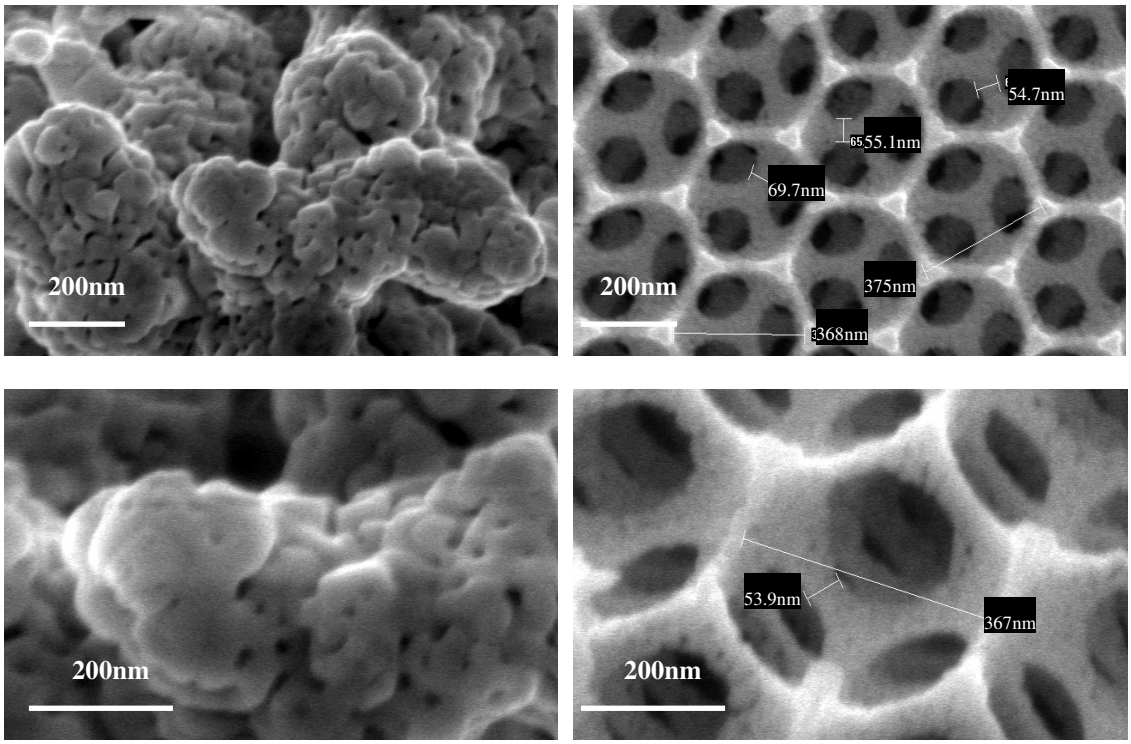
200nm
54.7nm
55.1nm
69.7nm
200nm
375nm
368nm
200nm
53.9nm
367nm
200nm

Appendix C

Transmission Electron Microscope (TEM) images at different magnifications for bulk and macroporous Ta_2O_5, TaON and Ta_3N_5; Pt-deposition bulk Ta_2O_5 and macroporous Ta_2O_5.

Bulk and Macroporous Ta_2O_5

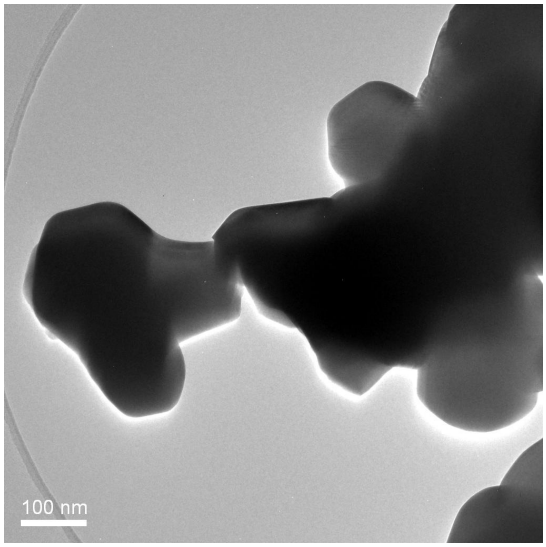

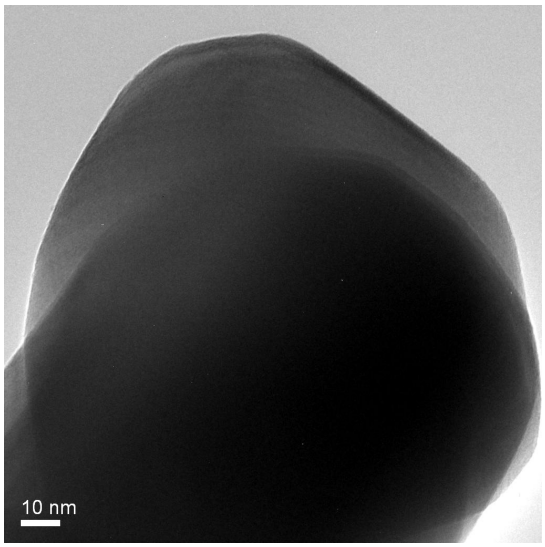

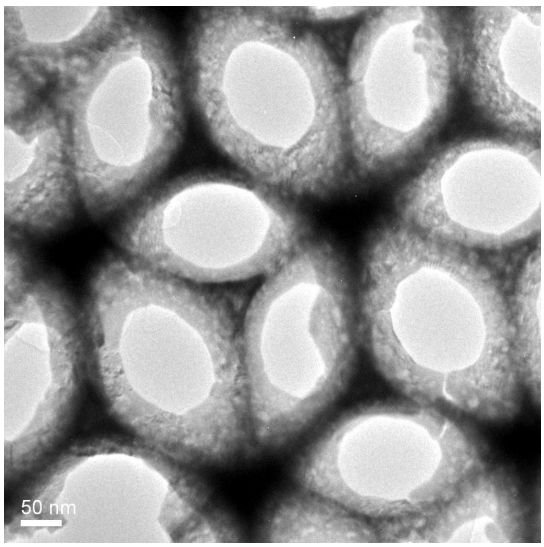

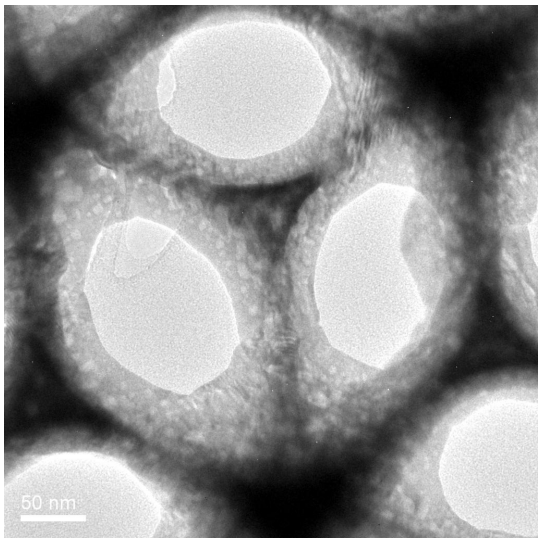

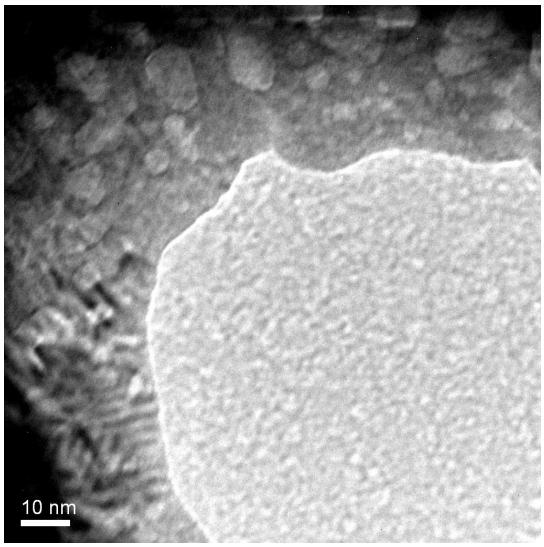

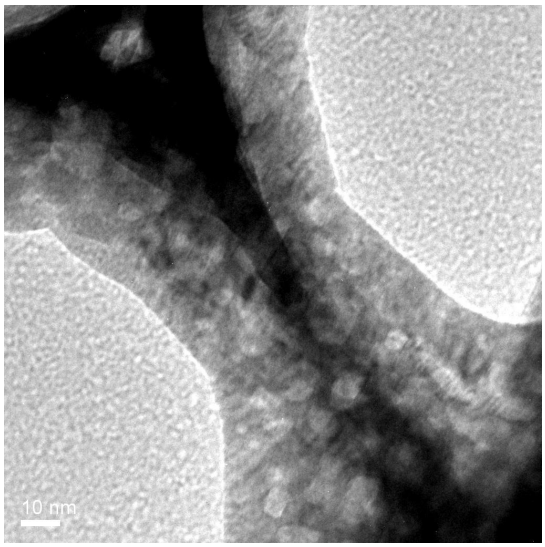

Bulk and Macroporous TaON

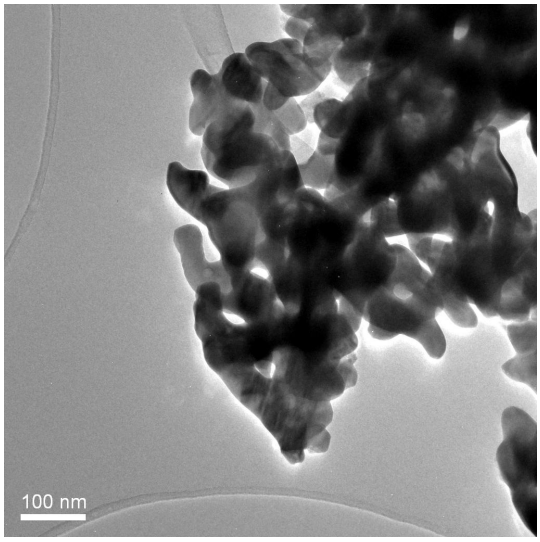

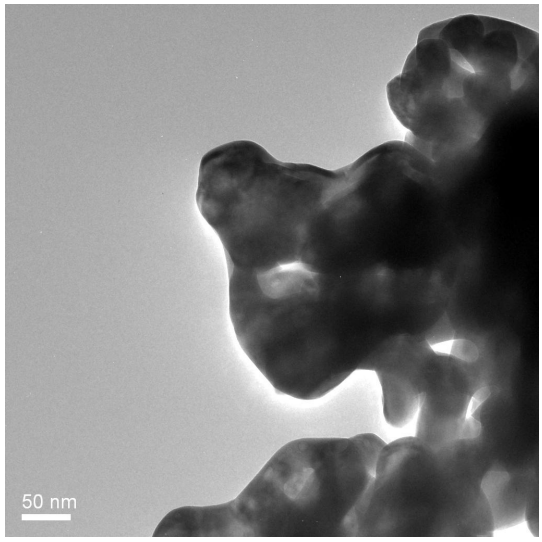

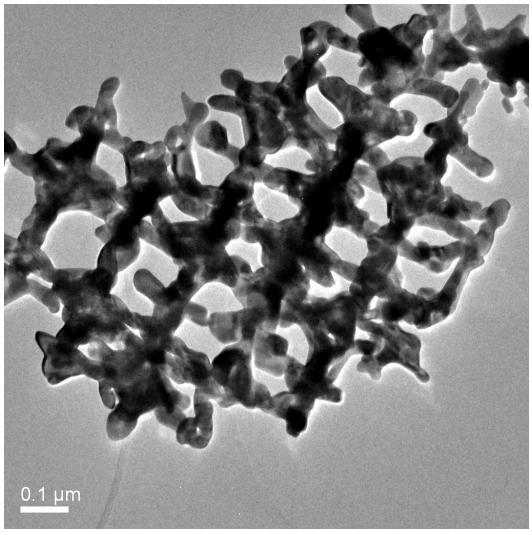

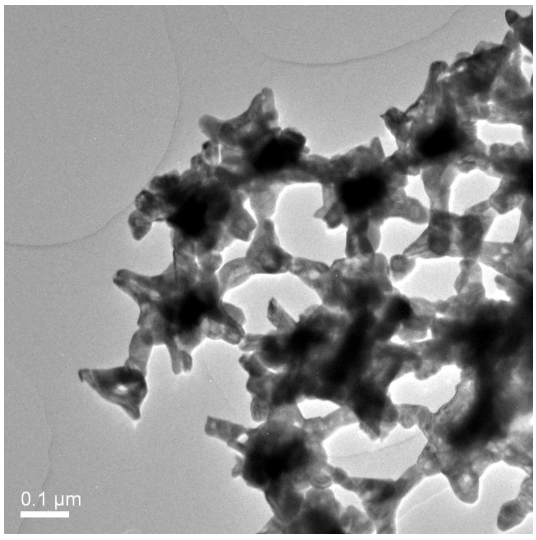

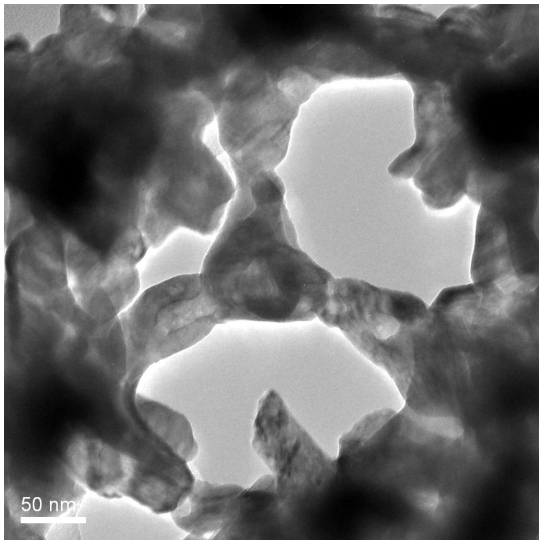

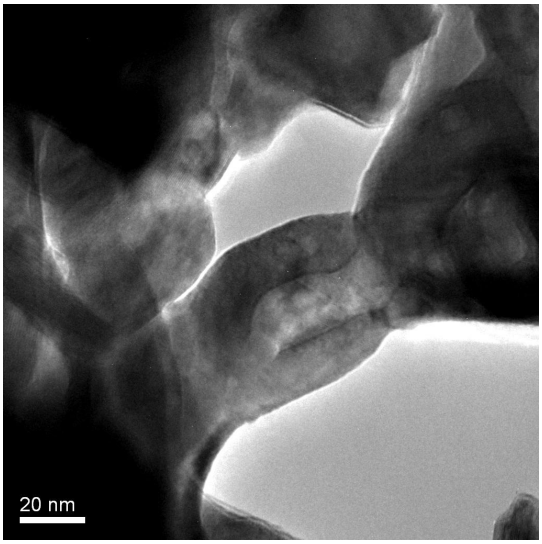

Bulk and Macroporous Ta_3N_5

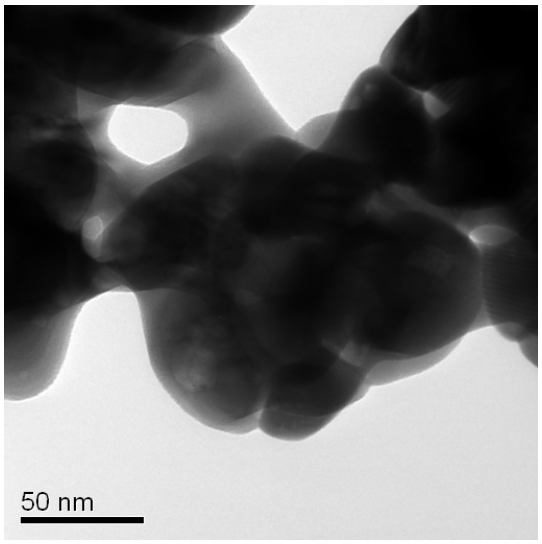

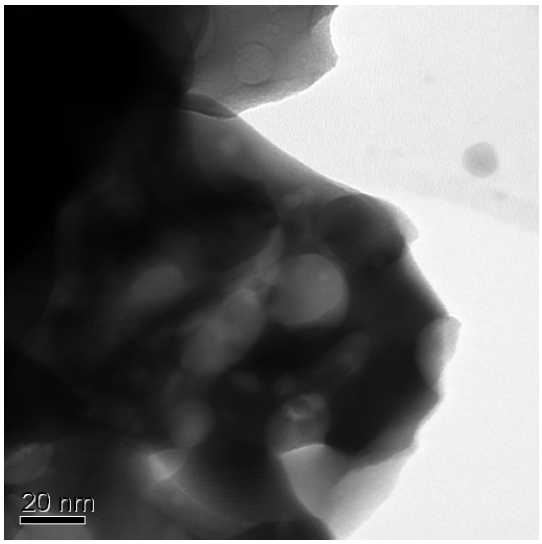

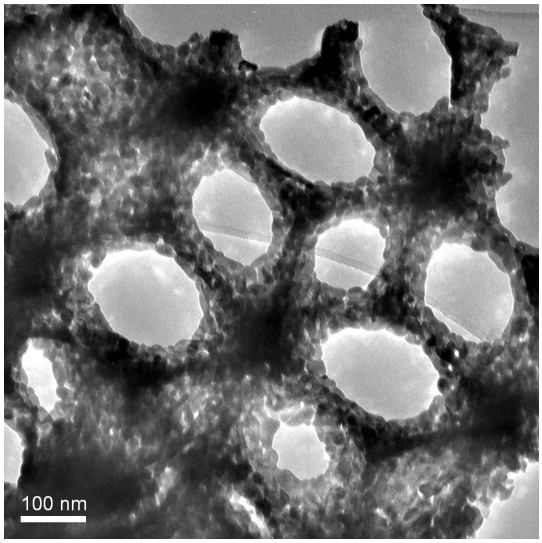

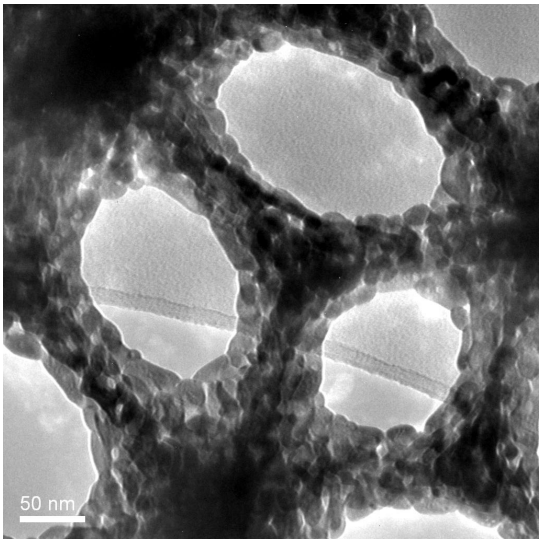

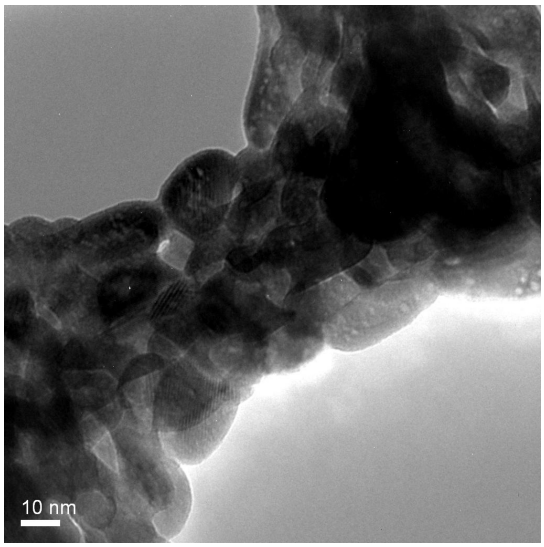

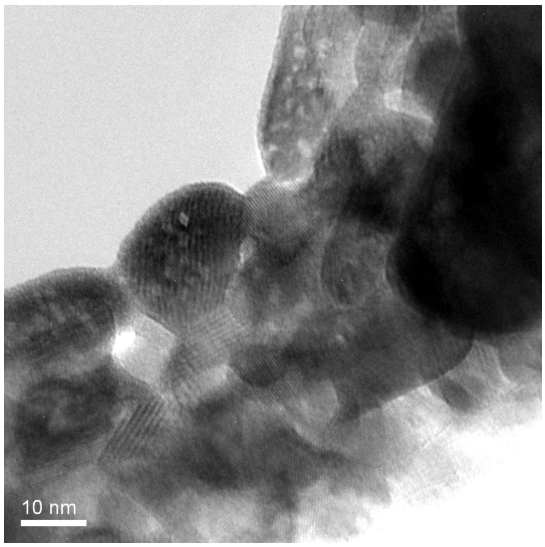

Pt-deposition of Bulk and Macroporous Ta_2O_5

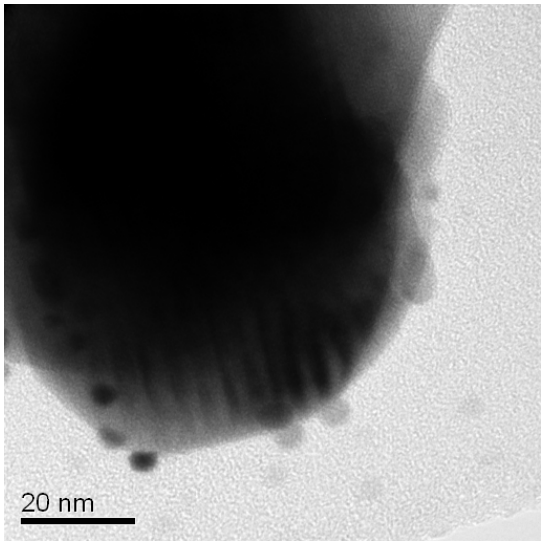

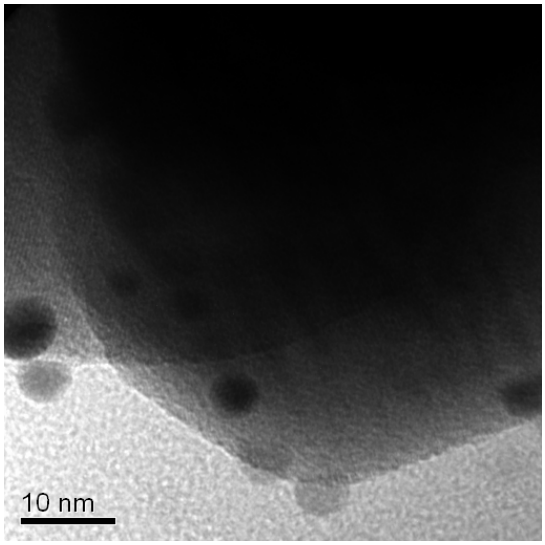

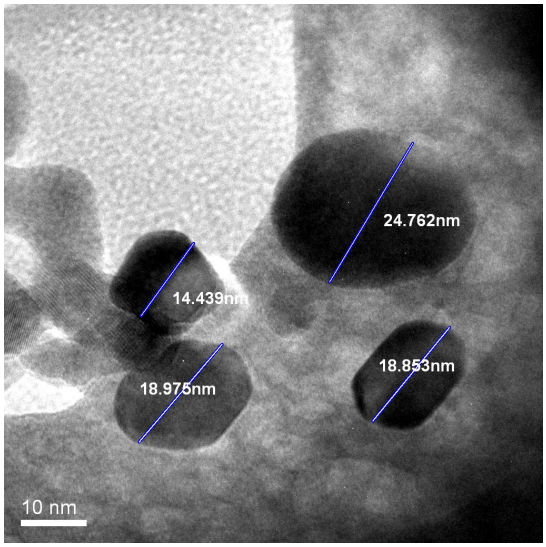

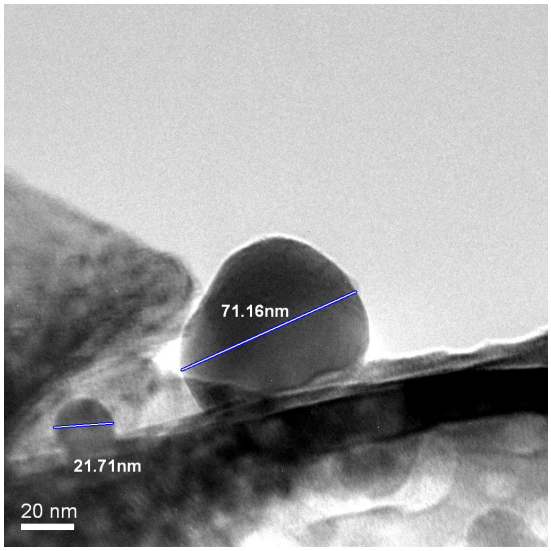

Appendix D

Brunauer-Emmett-Teller (BET) Surface Area nitrogen desorption and absorption graphs for bulk and macroporous Ta_2O_5, TaON and Ta_3N_5.

Bulk and Macroporous Ta_2O_5

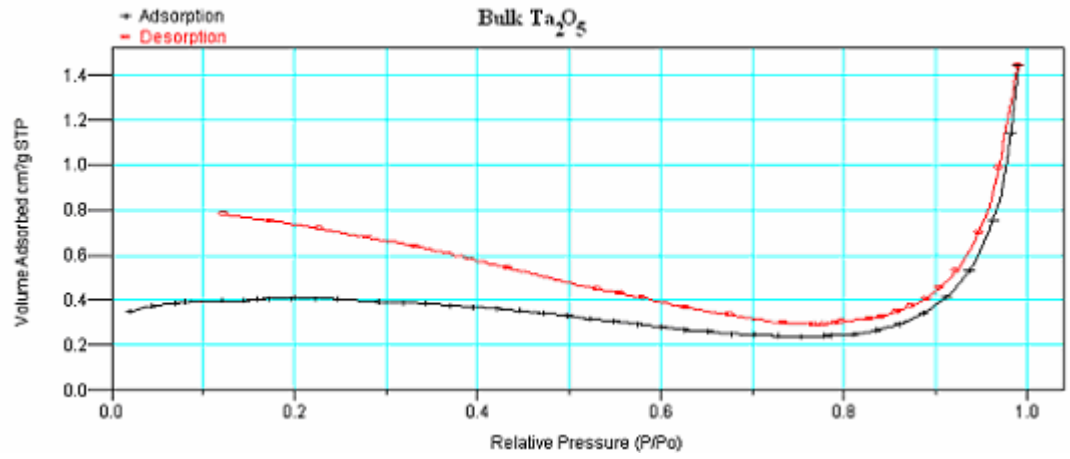

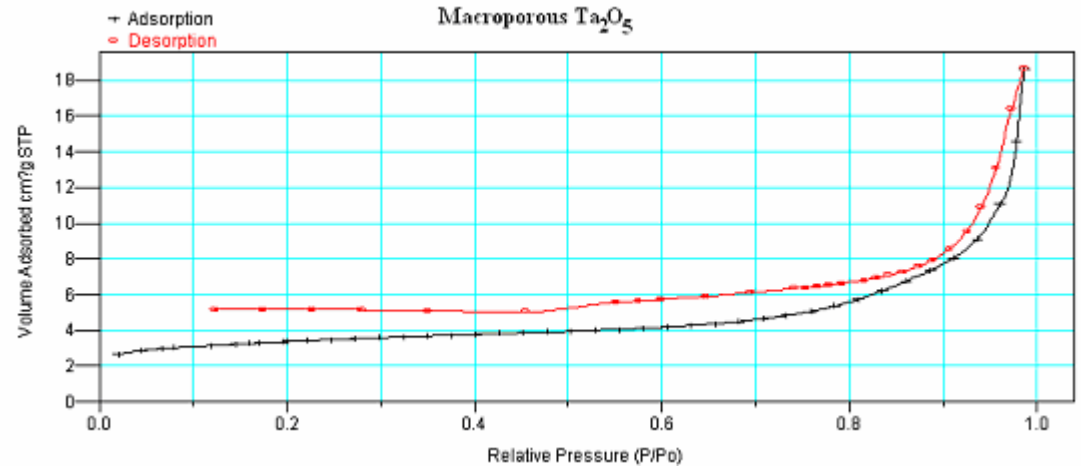

Bulk and Macroporous TaON

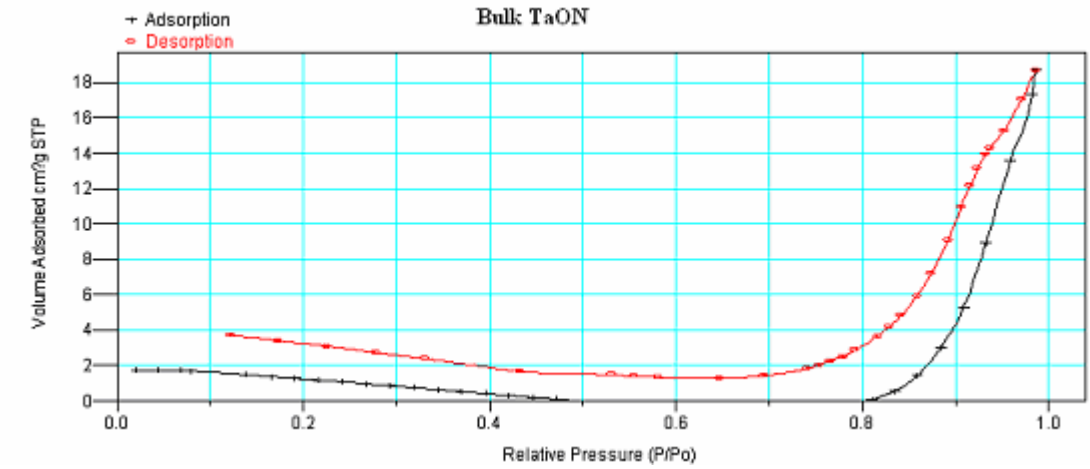

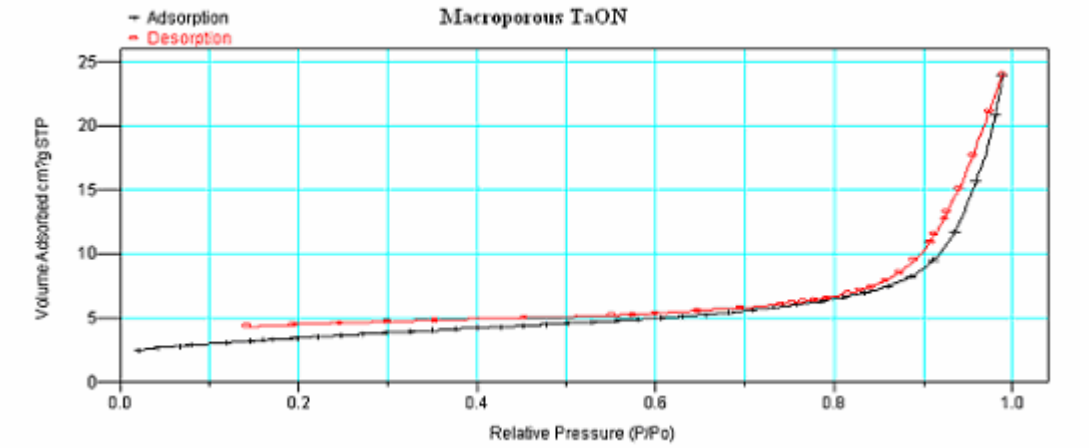

Bulk and Macroporous Ta_3N_5

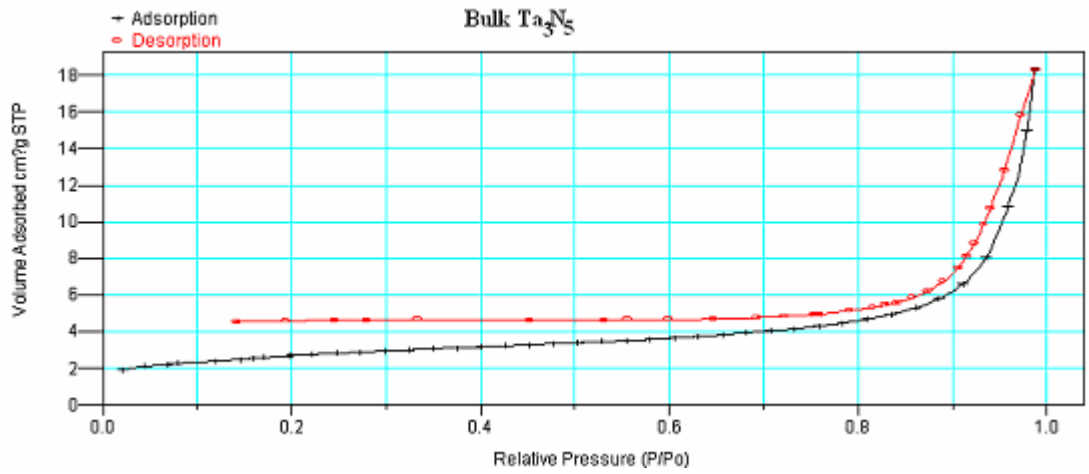

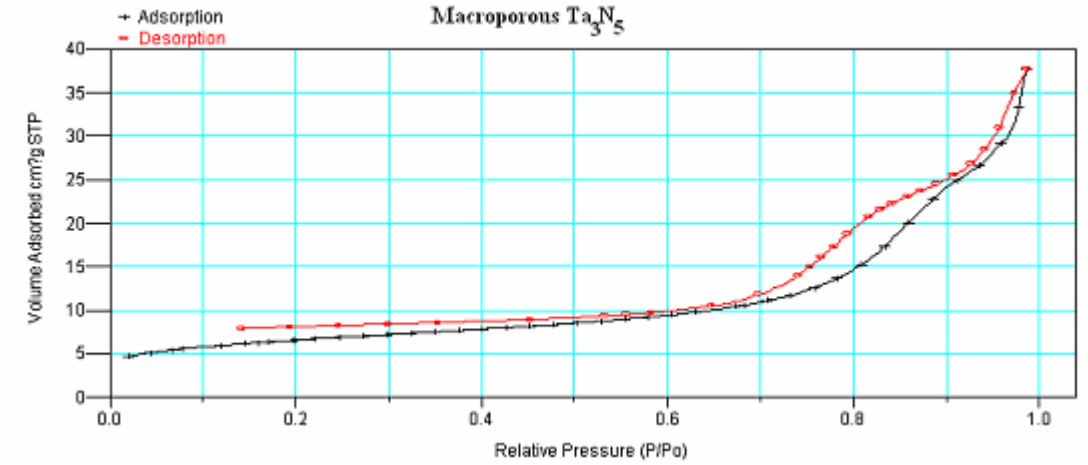

Reference

1. Ciesla, P., P. Kocot, P. Mytych, and Z. Stasicka, Homogeneous Photocatalysis by Transition Metal Complexes in the Environment. *Journal of Molecular Catalysis A: Chemical*, 2004. **224**(1-2): p. 17-33.
2. Kudo, A., Photocatalysis and solar hydrogen production. *Pure Appl. Chem.*, 2007. **79**: p. 1917 - 1927.
3. Herrmann, J.-M., Fundamentals and Misconceptions in Photocatalysis. *Journal of Photochemistry and Photobiology A: Chemistry*, 2010. **216**(2-3): p. 85-93.
4. International Energy Outlook 2010. 2010 [cited 2010 13th November]; Available from: http://www.eia.doe.gov/oiaf/ieo/pdf/0484(2010).pdf.
5. Zahedi, A., Maximizing Solar PV Energy Penetration Using Energy Storage Technology. *Renewable and Sustainable Energy Reviews*, 2011. **15**(1): p. 866-870.
6. Ni, M.L., Michael K. H. Leung, Dennis Y. C. Sumathy, K., A Review and Recent Developments in Photocatalytic Water-splitting Using TiO2 for Hydrogen Production. *Renewable and Sustainable Energy Reviews*, 2007. **11**(3): p. 401-425.
7. Zhu, J. and M. Zäch, Nanostructured Materials for Photocatalytic Hydrogen Production. *Current Opinion in Colloid & Interface Science*, 2009. **14**(4): p. 260-269.
8. Tributsch, H., Photovoltaic Hydrogen Generation. *International Journal of Hydrogen Energy*, 2008. **33**(21): p. 5911-5930.
9. Bak, T., J. Nowotny, M. Rekas, and C.C. Sorrell, Photo-electrochemical Hydrogen Generation from Water Using Solar Energy. Materials-related aspects. *International Journal of Hydrogen Energy*, 2002. **27**(10): p. 991-1022.
10. Fujishima, A., X. Zhang, and D.A. Tryk, Heterogeneous photocatalysis: From Water Photolysis to Applications in Environmental Cleanup. *International Journal of Hydrogen Energy*, 2007. **32**(14): p. 2664-2672.
11. Bahnemann, D., Photocatalytic Water Treatment: Solar Energy Applications. *Solar Energy*, 2004. **77**(5): p. 445-459.
12. Chen, Y.Z., P. Cui, G.X. Xiong, and H.Y. Xu, Novel Nickel-based Catalyst for Low Temperature Hydrogen Production from Methane Steam Reforming in Membrane Reformer. *Asia-Pacific Journal of Chemical Engineering*, 2010. **5**(1): p. 93-100.
13. Rakib, M.A., J.R. Grace, C.J. Lim, S. Elnashaie, and B. Ghiasi, Steam

Reforming of Propane in a Fluidized Bed Membrane Reactor for Hydrogen Production. *International Journal of Hydrogen Energy*, 2010. **35**(12): p. 6276-6290.

14. Chen, Y.Z., H.Y. Xu, Y.Z. Wang, and G.X. Xiong, Hydrogen Production From the Steam Reforming of Liquid Hydrocarbons in Membrane Reactor. *Catalysis Today*, 2006. **118**(1-2): p. 136-143.
15. Kudo, A. and Y. Miseki, Heterogeneous Photocatalyst Materials for Water Splitting. *Chemical Society Reviews*, 2009. **38**(1): p. 253-278.
16. Khaselev, O. and J.A. Turner, A Monolithic Photovoltaic-photoelectrochemical Device for Hydrogen Production Via Water Splitting. *Science,* 1998. **280**(5362): p. 425-427.
17. Choi, S.W., J.H. Yoon, M.J. An, W.S. Chae, H.M. Cho, M.G. Choi, and Y.R. Kim, Organic Nanotube Induced by Photocorrosion of CdS Nanorod. *Bulletin of the Korean Chemical Society*, 2004. **25**(7): p. 983-985.
18. Fujishima, A. and K. Honda, Electrochemical Photolysis of Water at a Semiconductor Electrode. *Nature*, 1972. **238**(5358): p. 37-38.
19. Osterloh, F.E., Inorganic Materials as Catalysts for Photochemical Splitting of Water. *Chemistry of Materials,* 2008. **20**(1): p. 35-54.
20. Zou, Z. and H. Arakawa, Direct Water Splitting into H_2 and O_2 under Visible Light Irradiation with a New Series of Mixed Oxide Semiconductor Photocatalysts. *Journal of Photochemistry and Photobiology A: Chemistry,* 2003. **158**(2-3): p. 145-162.
21. Maeda, K., K. Teramura, D. Lu, T. Takata, N. Saito, Y. Inoue, and K. Domen, Photocatalyst Releasing Hydrogen from Water. *Nature*, 2006. **440**(7082): p. 295-295.
22. Maeda, K. and K. Domen, New Non-oxide Photocatalysts Designed for Overall Water Splitting under Visible Light. *Journal of Physical Chemistry C*, 2007. **111**(22): p. 7851-7861.
23. Maeda, K., N. Nishimura, and K. Domen, A Precursor Route to Prepare Tantalum(V) Nitride Nanoparticles with Enhanced Photocatalytic Activity for Hydrogen Evolution under Visible Light. *Applied Catalysis a-General*, 2009. **370**(1-2): p. 88-92.
24. Sang, L.X., H.X. Dai, J.H. Sun, L.X. Xu, F. Wang, and C.F. Ma, Fabrication of the Hydrogen-evolving Photocatalyst with Mesoporous Structure. *International Journal of Hydrogen Energy*, 2010. **35**(13): p. 7098-7103.
25. Blanford, C.F., H.W. Yan, R.C. Schroden, M. Al-Daous, and A. Stein, Gems of Chemistry and Physics: Macroporous Metal Oxides with 3D

Order. *Advanced Materials*, 2001. **13**(6): p. 401-407.

26. Yang, Z.W., X.G. Huang, G. Yang, Q. Xie, B. Li, J. Zhou, and L.T. Li, Preparation and Photonic Bandgap Properties of Lead Lanthanum Titanate Inverse Opal Photonic Crystals. *Journal of Alloys and Compounds*, 2009. **468**(1-2): p. 295-298.
27. Yang, Z.W., J. Zhou, X.G. Huang, Q. Xie, M. Fu, B. Li, and L.T. Li, Preparation and Photonic Bandgap Properties of $Na_{1/2}Bi_{1/2}TiO_3$ Inverse Opal Photonic Crystals. *Journal of Alloys and Compounds*, 2009. **471**(1-2): p. 241-243.
28. Wijnhoven, J., L. Bechger, and W.L. Vos, Fabrication and Characterization of Large Macroporous Photonic Crystals in Titania. *Chemistry of Materials*, 2001. **13**(12): p. 4486-4499.
29. Waterhouse, G.I.N. and M.R. Waterland, Opal and Inverse Opal Photonic Crystals: Fabrication and Characterization. *Polyhedron*, 2007. **26**: p. 356-368.
30. Blanford, C.F., R.C. Schroden, M. Al-Daous, and A. Stein, Tuning Solvent-dependent Color Changes of Three-dimensionally Ordered Macroporous (3DOM) Materials Through Compositional and Geometric Modifications. *Advanced Materials*, 2001. **13**(1): p. 26-29.
31. Chen, J.I.L., G. von Freymann, V. Kitaev, and G.A. Ozin, Effect of Disorder on the Optically Amplified Photocatalytic Efficiency of Titania Inverse Opals. Journal of the American Chemical Society, 2007. **129**(5): p. 1196-1202.
32. Wang, C., A. Geng, Y. Guo, S. Jiang, and X. Qu, Three-dimensionally Ordered Macroporous $Ti_{1-x}Ta_xO_{2+x/2}$ (x = 0.025, 0.05, and 0.075) Nanoparticles: Preparation and Enhanced Photocatalytic Activity. *Materials Letters*, 2006. **60**(21-22): p. 2711-2714.
33. Schroden, R.C., M. Al-Daous, C.F. Blanford, and A. Stein, Optical Properties of Inverse Opal Photonic Crystals. *Chemistry of Materials*, 2002. **14**(8): p. 3305-3315.
34. Yablonovitch, E., Photonic Band-gap Structures. *Journal of the Optical Society of America B-Optical Physics*, 1993. **10**(2): p. 283-295.
35. Berger, V., Photonic Crystals and Photonic Structures. *Current Opinion in Solid State & Materials Science,* 1999. **4**(2): p. 209-216.
36. Schroden, R.C., M. Al-Daous, and A. Stein, Self-modification of Spontaneous Emission by Inverse Opal Silica Photonic Crystals. *Chemistry of Materials*, 2001. **13**(9): p. 2945-2950.
37. Stein, A. and R.C. Schroden, Colloidal Crystal Templating of

Three-dimensionally Ordered Macroporous Solids: Materials for Photonics and Beyond. *Current Opinion in Solid State & Materials Science*, 2001. **5**(6): p. 553-564.

38. Stein, A., F. Li, and N.R. Denny, Morphological Control in Colloidal Crystal Templating of Inverse Opals, Hierarchical Structures, and Shaped Particles. *Chemistry of Materials*, 2008. **20**(3): p. 649-666.
39. Sadakane, M., T. Horiuchi, N. Kato, K. Sasaki, and W. Ueda, Preparation of Three-dimensionally Ordered Macroporous Perovskite-type Lanthanum-iron-oxide $LaFeO_3$ with Tunable Pore Diameters: High Porosity and Photonic Property. *Journal of Solid State Chemistry*, 2010. **183**(6): p. 1365-1371.
40. Wang, J.J., Q. Li, W. Knoll, and U. Jonas, Preparation of Multilayered Trimodal Colloid Crystals and Binary Inverse Opals. *Journal of the American Chemical Society*, 2006. **128**: p. 15606-15607.
41. Wang, D.Y., R.A. Caruso, and F. Caruso, Synthesis of Macroporous Titania and Inorganic Composite Materials from Coated Colloidal Spheres - A novel Route to Tune Pore Morphology. *Chemistry of Materials*, 2001. **13**(2): p. 364-371.
42. Zhang, J.H., Z. Chen, Z.L. Wang, W.Y. Zhang, and N.B. Ming, Preparation of Mohodisperse Polystyrene Spheres in Aqueous Alcohol System. *Materials Letters*, 2003. **57**(28): p. 4466-4470.
43. Ou, J.L., J.K. Yang, and H. Chen, Styrene/potassium Persulfate/water systems: Effects of Hydrophilic Comonomers and Solvent Additives on the Nucleation Mechanism and the Particle Size. *European Polymer Journal*, 2001. **37**(4): p. 789-799.
44. Maschmeyer, T. and M. Che, Catalytic Aspects of Light-Induced Hydrogen Generation in Water with TiO2 and Other Photocatalysts: A Simple and Practical Way Towards a Normalization? *Angewandte Chemie-International Edition*, 2010. **49**(9): p. 1536-1539.
45. Devi, L.G. and K.M. Reddy, Enhanced Photocatalytic Activity of Silver Metallized TiO2 Particles in the Degradation of an Azo Dye Methyl Orange: Characterization and Activity at Different pH Values. *Applied Surface Science*, 2010. **256**(10): p. 3116-3121.
46. Zheng, X.J., L.F. Wei, Z.H. Zhang, Q.J. Jiang, Y.J. Wei, B. Xie, and M.B. Wei, Research on Photocatalytic H_2 Production from Acetic Acid Solution by Pt/TiO2 Nanoparticles under UV Irradiation. *International Journal of Hydrogen Energy*, 2009. **34**(22): p. 9033-9041.
47. Yu, J.G., Y.R. Su, B. Cheng, and M.H. Zhou, Effects of pH on the

Microstructures and Photocatalytic Activity of Mesoporous Nanocrystalline Titania Powders Prepared via Hydrothermal Method. *Journal of Molecular Catalysis a-Chemical*, 2006. **258**(1-2): p. 104-112.

48. Zhang, A.P., J.Z. Zhang, N.Y. Cui, X.Y. Tie, Y.W. An, and L.J. Li, Effects of pH on Hydrothermal Synthesis and Characterization of Visible-light-driven $BiVO_4$ Photocatalyst. *Journal of Molecular Catalysis a-Chemical*, 2009. **304**(1-2): p. 28-32.
49. Herrmann, J.M., Heterogeneous Photocatalysis: State of the Art and Present Applications. *Topics in Catalysis*, 2005. **34**(1-4): p. 49-65.
50. Badawy, M.I., M.Y. Ghaly, and M.E.M. Ali, Photocatalytic Hydrogen Production Over Nanostructured Mesoporous Titania from Olive Mill Wastewater. *Desalination*, 2010. **In Press, Corrected Proof**.
51. Puangpetch, T., T. Sreethawong, and S. Chavadej, Hydrogen Production over Metal-loaded Mesoporous-assembled $SrTiO_3$ Nanocrystal Photocatalysts: Effects of Metal Type and Loading. *International Journal of Hydrogen Energy*, 2010. **35**(13): p. 6531-6540.
52. Sreethawong, T., T. Puangpetch, S. Chavadej, and S. Yoshikawa, Quantifying Influence of Operational Parameters on Photocatalytic H_2 Evolution Over Pt-loaded Nanocrystalline Mesoporous TiO_2 Prepared by Single-step Sol-gel Process with Surfactant Template. *Journal of Power Sources*, 2007. **165**(2): p. 861-869.
53. Holland, B.T., C.F. Blanford, T. Do, and A. Stein, Synthesis of Highly Ordered, Three-dimensional, Macroporous Structures of Amorphous or Crystalline Inorganic Oxides, Phosphates, and Hybrid Composites. *Chemistry of Materials*, 1999. **11**(3): p. 795-805.
54. Schilling, H., A. Stork, E. Irran, H. Wolff, T. Bredow, R. Dronskowski, and M. Lerch, gamma-TaON: A Metastable Polymorph of Tantalum Oxynitride. *Angewandte Chemie-International Edition,* 2007. **46**(16): p. 2931-2934.
55. Wikipedia. Shape Factor (X-ray diffraction). Available from: http://en.wikipedia.org/wiki/Shape_factor_(X-ray_diffraction).[cited 16th October, 2010]
56. Lu, D.L., G. Hitoki, E. Katou, J.N. Kondo, M. Hara, and K. Domen, Porous Single-crystalline TaON and Ta3N5 Particles. *Chemistry of Materials*, 2004. **16**(9): p. 1603-1605.
57. Takahara, Y., J.N. Kondo, T. Takata, D.L. Lu, and K. Domen, Mesoporous Tantalum Oxide. 1. Characterization and Photocatalytic Activity for the Overall Water Decomposition. *Chemistry of Materials*, 2001. **13**(4): p. 1194-1199.

58. Hisatomi, T., M. Otani, K. Nakajima, K. Teramura, Y. Kako, D.L. Lu, T. Takata, J.N. Kondo, and K. Domen, Preparation of Crystallized Mesoporous Ta3N5 Assisted by Chemical Vapor Deposition of Tetramethyl Orthosilicate. *Chemistry of Materials,* 2010. **22**(13): p. 3854-3861.
59. Hara, M., T. Takata, J.N. Kondo, and K. Domen, Photocatalytic Reduction of Water by TaON Under Visible Light Irradiation. *Catalysis Today,* 2004. **90**(3-4): p. 313-317.
60. Hara, M., G. Hitoki, T. Takata, J.N. Kondo, H. Kobayashi, and K. Domen, TaON and Ta3N5 as New Visible Light Driven Photocatalysts. *Catalysis Today,* 2003. **78**(1-4): p. 555-560.
61. Hitoki, G., T. Takata, J.N. Kondo, M. Hara, H. Kobayashi, and K. Domen, An Oxynitride, TaON, As an Efficient Water Oxidation Photocatalyst Under Visible Light Irradiation (Lambda <= 500 nm). *Chemical Communications,* 2002(16): p. 1698-1699.
62. Hitoki, G., T. Takata, J.N. Kondo, M. Hara, H. Kobayashi, and K. Domen, An Oxynitride, TaON, As an Efficient Water Oxidation Photocatalyst under Visible Light Irradiation ($\lambda \leq 500$ nm). *ChemInform,* 2002. **33**(45): p. 11-11.
63. Ishikawa, A., T. Takata, J.N. Kondo, M. Hara, and K. Domen, Electrochemical Behavior of Thin Ta3N5 Semiconductor Film. *Journal of Physical Chemistry B*, 2004. **108**(30): p. 11049-11053.
64. Ohtani, B., O.O. Prieto-Mahaney, D. Li, and R. Abe, What is Degussa (Evonik) P25? Crystalline Composition Analysis, Reconstruction from Isolated Pure Particles and Photocatalytic Activity Test. *Journal of Photochemistry and Photobiology A: Chemistry*, 2010. **216**(2-3): p. 179-182.
65. Brauer, G. and J.R. Weidlein, Synthesis and Properties of Tantalum Oxide Nitride TaON. *Angewandte Chemie-International Edition*, 1965. **4**(10): p. 875-&.
66. Orhan, E., F. Tessier, and R. Marchand, Synthesis and Energetics of Yellow TaON. *Solid State Sciences*, 2002. **4**(8): p. 1071-1076.
67. Mills, A., Platinisation of Semiconductor Particles. *Chem. Soc, Chem. Commun.,* 1983: p. 367-368.
68. Polyanskiy, M. Refractive Index Database. 2008-2010 [cited 2010 16th June]; Available from: http://refractiveindex.info/.